



"Identifying the microstructural changes for alcoholic patients during short-term abstinence via diffusion Magnetic Resonance Imaging"

Dausort, Manon ; Falyse, Faustine

ABSTRACT

Diffusion magnetic resonance imaging is a powerful tool to characterise the microstructural state of the brain as well as its changes over time. It has therefore been used for years now to evaluate the impact of several pathologies. This paper focuses on the impact of short-term abstinence on alcohol use disorder. A study on a set of 35 patients was conducted in order to have a better insight into the microstructural changes in their brain and the potential reversible damages of alcohol. For each subject, two scans, one on first day of an abstinence program and second 18 days later, were considered to assess the influence of short-term abstinence. Several microstructural models were applied on those diffusion data to retrieve the evolution of different metrics as well as the biological implications they have. The behavioral aspects of the subjects were also taken into consideration to spot any direct correlation between the alcoholism symptoms and changes of microstructural integrity. From those tests, two tendencies were observed among the patients which enabled to divide them into two clusters. The first cluster did not show significant changes in the course of abstinence. By contrast, the second cluster showed a high number of rearrangements in the structures of the limbic system, the cerebellum, its peduncles and the cortico-ponto cerebellar pathway. The evolution of the metrics can however translate two opposite phenomena linked with inflammation: a disinflammation of the extra-axonal space in those structures, suggesting a recovery process, or an inflammation of the f...

CITE THIS VERSION

Dausort, Manon ; Falyse, Faustine. *Identifying the microstructural changes for alcoholic patients during short-term abstinence via diffusion Magnetic Resonance Imaging*. Ecole polytechnique de Louvain, Université catholique de Louvain, 2022. Prom. : Macq, Benoît ; Dricot, Laurence. <http://hdl.handle.net/2078.1/thesis:35541>

Le répertoire DIAL.mem est destiné à l'archivage et à la diffusion des mémoires rédigés par les étudiants de l'UCLouvain. Toute utilisation de ce document à des fins lucratives ou commerciales est strictement interdite. L'utilisateur s'engage à respecter les droits d'auteur liés à ce document, notamment le droit à l'intégrité de l'oeuvre et le droit à la paternité. La politique complète de droit d'auteur est disponible sur la page [Copyright policy](#)

DIAL.mem is the institutional repository for the Master theses of the UCLouvain. Usage of this document for profit or commercial purposes is strictly prohibited. User agrees to respect copyright, in particular text integrity and credit to the author. Full content of copyright policy is available at [Copyright policy](#)

École polytechnique de Louvain

TFE22-540

Identifying the microstructural changes for
alcoholic patients during short-term abstinence
via diffusion Magnetic Resonance Imaging

Authors: **Manon DAUSORT, Faustine FALYSE**

Supervisors: **Benoît MACQ, Laurence DRICOT**

Readers: **Nicolas DELINTE, Frédéric CREVECOEUR**

Academic year 2021–2022

Master [120] in Biomedical Engineering

Acknowledgements

We wish to express our gratefulness to our supervisors, Pr Benoît Macq and Pr Laurence Dricot, for giving us the opportunity to work on such an exciting subject and to meet all the people who helped us.

We are deeply indebted to Nicolas Delinte for all the hours he gave us during this work and for all the advice that enabled us to complete this master thesis.

We would also like to thank Quentin Dessain, Philippe de Timary and Mélissa Salavrakos.

Finally, we would like to express our profound gratitude to all the people who supported and encouraged us during our studies.

Abstract

Diffusion magnetic resonance imaging is powerful tool to characterise the microstructural state of the brain as well as its changes over time. It has therefore been used for years now to evaluate the impact of several pathologies. This paper focuses on the impact of short-term abstinence on alcohol use disorder. A study on a set of 35 patients was conducted in order to have a better insight into the microstructural changes in their brain and the potential reversible damages of alcohol. For each subject, two scans, one on first day of an abstinence program and second 18 days later, were considered to assess the influence of short-term abstinence. Several microstructural models were applied on those diffusion data to retrieve the evolution of different metrics as well as the biological implications they have. The behavioral aspects of the subjects were also taken into consideration to spot any direct correlation between the alcoholism symptoms and changes of microstructural integrity. From those tests, two tendencies were observed among the patients which enabled to divide them into two clusters. The first cluster did not show significant changes in the course of abstinence. By contrast, the second cluster showed a high number of rearrangements in the structures of the limbic system, the cerebellum, its peduncles and the cortico-ponto cerebellar pathway. The evolution of the metrics can however translate two opposite phenomena linked with inflammation: a disinflammation of the extra-axonal space in those structures, suggesting a recovery process, or an inflammation of the fibers, suggesting a continued progression of the damages. The impact of abstinence on some patients is undeniable and further analyses should be performed on biological data to identify which hypothesis (inflammation or further damage) reflects the actual evolution of the brain during short-term abstinence. The recovery hypothesis seems to be the most appropriate one, regarding the evolution of the behavioral data.

Keywords: Alcoholism, Alcohol Use Disorder, Abstinence, MRI, Brain, Diffusion Tensor Imaging

Contents

Acknowledgements	i
Abstract	ii
List of Figures	ix
List of Tables	x
Acronyms	xi
Introduction	1
I State of the art	2
1 Magnetic Resonance Imaging	2
1.1 Nuclear Magnetic Resonance	2
1.1.1 Relaxation	5
1.1.2 Spin Echo sequence	7
1.1.3 Image contrast	8
1.1.4 Acquisition	9
1.2 Diffusion imaging techniques	11
1.2.1 Diffusion-Weighted MRI	11
1.2.2 Diffusion Tensor Imaging (DTI)	14
1.3 Advantages and limitations of DTI	16
1.4 Advanced multi-compartment diffusion models	17
1.4.1 NODDI	17
1.4.2 DIAMOND	19
1.4.3 Microstructure fingerprinting	20
2 ElikoPy pipeline	21
3 Alcohol Use Disorder	24
3.1 Definition of AUD	24
3.2 Impact of DNA on alcoholism	25
3.3 Biological impact of AUD	27
3.3.1 Brain Anatomy	27
3.3.2 Microstructural alterations caused by alcohol	30
3.4 Microstructural effects of abstinence	32
3.4.1 DTI metric changes	32
3.4.2 Volumetric Changes	33
3.5 Psychological influence of alcohol and abstinence	34
3.5.1 Alcohol effect	34
3.5.2 Abstinence effect	35
II Brain microstructure analysis	36

4 Methods	36
4.1 Data collection	36
4.2 Data conversion	38
4.3 Regions of Interest (ROI)	39
4.3.1 Atlas collection	39
4.3.2 Corpus Callosum modifications	40
4.3.3 Corpus callosum division	43
4.3.4 Atlas registration	43
4.4 Microstructure analysis	45
4.4.1 General evolution concept	45
4.4.2 Clustering	46
4.4.3 Statistical analysis	47
4.4.4 DTI analysis	48
4.4.5 NODDI analysis	48
4.4.6 DIAMOND analysis	50
4.4.7 Microstructure Fingerprinting	51
4.5 Treatment of the behavioral data	53
4.6 Motion analysis	53
4.7 Volumetric changes analysis	53
5 Results	55
5.1 Clusters	55
5.2 Motion	57
5.3 DTI analysis	58
5.3.1 Gray matter and lobes	58
5.3.2 White matter, cerebellum and subcortical structures	59
5.4 NODDI analysis	62
5.5 DIAMOND analysis	67
5.6 MF analysis	69
5.7 Volumetric changes in the three main brain compartments	71
5.8 Conspicuous regions	72
5.9 Behavioral analysis	75
6 Discussion	77
6.1 Relevance of the different microstructural models	77
6.2 Interpretation of the different metric variations	78
6.2.1 DTI	78
6.2.2 NODDI	79
6.2.3 DIAMOND	80
6.2.4 MF	81
6.3 Conspicuous regions	82
6.3.1 Noteworthy changes in Cluster 1	82
6.3.2 Noteworthy changes in Cluster 2	83
6.3.3 Respective volumes of the conspicuous regions	84
6.4 Resulting behavioral expectations	84
6.5 Limitations	86
6.6 Further perspectives	88
7 Conclusion	90

Appendix	100
A MRI parameters: typical .json file	100
B Atlases	101
C Coherence of the microstructural models	103
C.1 NODDI: Coherence of fintra, fextra and fiso	103
C.2 DIAMOND: Coherence of frac_csf and frac_ftot	105
C.3 MF: Coherence of frac_csf and frac_ftot	107
C.4 Coherence of FA, ODI and <i>wFA</i>	109
C.5 Coherence of fiso (NODDI) and frac_csf (DIAMOND, MF)	111

List of Figures

1.1	Representation of a spin and the magnetic moment of a particle	2
1.2	behavior of protons with or without the presence of an external magnetic field	3
1.3	Impact of different RF pulses on the macroscopic magnetization vector	4
1.4	Impact of different RF pulses on the 4 excess protons	5
1.5	Illustration of the evolution of both components of magnetization during T_1 relaxation	6
1.6	Illustration of a sequence creating spin echoes	7
1.7	Spin Echo sequence	7
1.8	Evolution of the signal of two tissues with different TR	8
1.9	Evolution of the signal of two tissues with different TE	9
1.10	Evolution of the signal of three tissues with the same TR and TE but with a different proton density	9
1.11	Compensation for the phase shifts by addition of a negative lobe	10
1.12	Complete timeline of gradient placement in the spin echo sequence	11
1.13	Diffusion gradient in a PGSE sequence	12
1.14	Diffusion gradients and their effects on signal	13
1.15	Influence of motion on proton phase	13
1.16	Evolution of the ellipse representing the diffusion tensor	16
1.17	Maps of the different DTI metrics	16
1.18	NODDI model	19
1.19	DIAMOND model	20
2.1	ElikoPy pipeline	23
3.1	Distribution of AUD in the world	24
3.2	Epigenetic mechanisms	26
3.3	Predisposition & development of alcoholism (genetics and environment)	26
3.4	Brain lobes	27
3.5	Hypothalamus, Thalamus, Epithalamus	28
3.6	The limbic system	29
3.7	Division of the corpus callosum	29
3.8	Cerebellum and ventricles	30
3.9	Evolution of WM volume (AUD vs control)	34
4.1	Anatomic scan of a patient	37
4.2	Diffusion scan of a patient for different b-values	37
4.3	Lobules assignment of the cerebellum	39
4.4	Limitation of the initial CC atlas	40
4.5	HCP1065 standard-space FA map.	41
4.6	CC creation	41
4.7	Hand-drawn CC creation	42
4.8	Final CC atlas	42
4.9	Topography of the midsagittal CC, and sagittal and axial slice of the sub-division of CC map used	43
4.10	Transformations used for the registration	44
4.11	Registration process for the Cingulum atlas map	44
4.12	Superposition of brain mask and WM mask	45
4.13	Clustering procedure	47
4.14	Representation of DTI metrics	48
4.15	Representation of NODDI metrics	49

4.16	Difference between FA and <i>wFA</i>	50
4.17	Representation of DIAMOND metrics	51
4.18	Difference between <i>fvf_tot</i> and <i>wfvf</i> : <i>fvf_tot</i> estimates the proportion of fibers in the entire voxel whereas <i>wfvf</i> only considers the fiber compartment and evaluates the concentration of the fibers.	52
4.19	Representation of MF metrics	52
5.1	Clustering result	56
5.2	Summary of all regions showing significant MD changes (GM areas and lobes) considering cluster 2.	58
5.3	Summary of all regions showing significant RD (top), AD (middle) and FA (bottom) changes considering cluster 1.	59
5.4	Summary of all regions showing significant FA changes (WM and cerebellum) considering cluster 2.	60
5.5	Summary of all regions showing significant AD changes (cerebellum) considering cluster 2.	60
5.6	Summary of all regions showing significant RD changes (cerebellum) considering cluster 2.	60
5.7	Summary of all regions showing significant AD changes (WM and subcortical areas) considering cluster 2.	61
5.8	Summary of all regions showing significant RD changes (WM and subcortical areas) considering cluster 2.	61
5.9	Summary of all regions showing significant <i>fextra</i> changes (WM and cerebellum) considering cluster 1.	62
5.10	Summary of all regions showing significant <i>fiso</i> changes (WM and cerebellum) considering cluster 1.	63
5.11	Summary of all regions showing significant <i>fextra</i> (bottom) and <i>fiso</i> (top) changes (subcortical areas) considering cluster 1.	63
5.12	Summary of all regions showing significant <i>fintra</i> changes (WM and cerebellum) considering cluster 2.	63
5.13	Summary of all regions showing significant <i>fextra</i> changes (WM (top) and cerebellum (bottom)) considering cluster 2.	64
5.14	Summary of all regions showing significant <i>fiso</i> changes (WM and cerebellum) considering cluster 2.	65
5.15	Summary of all regions showing significant ODI changes (WM and cerebellum) considering cluster 2.	65
5.16	Summary of all regions showing significant <i>fintra</i> changes (subcortical areas) considering cluster 2.	66
5.17	Summary of all regions showing significant <i>fextra</i> changes (subcortical areas) considering cluster 2.	66
5.18	Summary of all regions showing significant ODI (top) and <i>fiso</i> (bottom) changes (subcortical areas) considering cluster 2.	66
5.19	Summary of all regions significant <i>wFA</i> (bottom) and <i>wAD</i> (top) changes (WM, cerebellum and subcortical areas) considering cluster 2.	67
5.20	Summary of all regions significant <i>wRD</i> changes (WM, cerebellum and subcortical areas) considering cluster 2.	68
5.21	Summary of all regions showing significant <i>frac_csf</i> changes considering cluster 1 (bottom) and cluster 2 (top).	68
5.22	Summary of all regions showing significant <i>frac_csf</i> changes (WM and cerebellum) considering cluster 1 (bottom) and cluster 2 (top).	69

5.23	Summary of all regions showing significant <code>fvf_tot</code> changes (WM and subcortical areas) considering cluster 2.	70
5.24	Summary of all regions showing significant <code>frac_ftot</code> and <code>fvf_tot</code> changes (cerebellum) considering cluster 2.	70
5.25	Overall volumetric changes (WM,GM,CSF) considering cluster 1. .	71
5.26	Overall volumetric changes (WM,GM,CSF) considering cluster 2. .	71
5.27	3D view of the conspicuous regions.	73
5.28	Local volumetric changes (conspicuous regions) - Cluster 1	74
5.29	Local volumetric changes (conspicuous regions) - Cluster 2	74
5.30	Evolution of the behavioral metrics for each cluster.	76
6.1	Possible evolutions between the different DTI metrics. A : FA decrease caused by a diffusion decrease with a stronger AD change; B : FA increase caused by a diffusion decrease with a stronger RD change; C : homogeneous decrease in AD and RD resulting in non noticeable change in FA.	79
6.2	Possible evolutions between the different DTI metrics. A : FA decrease caused by a diffusion decrease with a stronger AD change; B : FA increase caused by a diffusion decrease with a stronger RD change; C : homogeneous decrease in AD and RD resulting in non noticeable change in FA.	80
6.3	Different evolution in T2 observed: scenario 1 characterises no noticeable change; scenario 2 represents reduced proportion of CSF with no significant change in the fiber concentration; scenario 3 illustrates a total fiber volume fraction increase but with no volume change for the general CSF and fiber fractions.	81
6.4	Conspicuous regions	82
6.5	Volume of conspicuous regions	84
6.6	Cortico-ponto cerebellar pathway	85
6.7	Illustration of the difference between a region in T1 & T2.	87
C.1	Coherence of the NODDI model considering cluster 1	103
C.2	Coherence of the NODDI model considering cluster 2 part 1	104
C.3	Coherence of the NODDI model considering cluster 2 part 2	104
C.4	Compensation of the CSF and fiber volume fractions.	105
C.5	Coherence of the DIAMOND model considering cluster 1	105
C.6	Coherence of the DIAMOND model considering cluster 2	106
C.7	Coherence of the MF model considering cluster 1 - summary of all regions showing at least one significant change in <code>frac_ftot</code> or <code>frac_csf</code> . The bars represent the difference between T2 and T1 i.e. $(T2 - T1) * 100$	107
C.8	Coherence of the MF model considering cluster 2 - summary of all regions showing at least one significant change in <code>frac_ftot</code> or <code>frac_csf</code> . The bars represent the difference between T2 and T1 i.e. $(T2 - T1) * 100$	108
C.9	Coherence of cluster 2 considering FA, ODI and <i>wFA</i> - part 1. The bars represent the difference between T2 and T1 i.e. $(T2 - T1) * 100$.109	
C.10	Coherence of cluster 2 considering FA, ODI and <i>wFA</i> - part 2. The bars represent the difference between T2 and T1 i.e. $(T2 - T1) * 100$.110	
C.11	Coherence of cluster 1 considering <code>fiso</code> , <code>frac_csf</code> (DIAMOND) and <code>frac_csf</code> (MF). The bars represent the difference between T2 and T1 i.e. $(T2 - T1) * 100$	111

List of Tables

3.1	Summary of the observations published by different articles	32
5.1	Clusters formed by the K-means algorithm for different values of K and result of the affinity propagation method.	57

Acronyms

ACC Anterior Cingulate Cortex.

AD Axial Diffusivity.

ADC Apparent Diffusion Coefficient.

ADH alcohol dehydrogenase.

ALDH aldehyde dehydrogenase.

AUD Alcohol Use Disorder.

BDI Beck Depression Inventory.

BEARNI Brief Evaluation of Alcohol-Related Neuropsychological Impairments.

BIDS Brain Imaging Data Structure.

CAC current alcohol consumption.

CC Corpus Callosum.

CNR Carrier to Noise ratio.

CNS Central Nervous System.

CPC Cortico-Ponto Cerebellar.

CSF Cerebrospinal fluid.

DAD duration of alcohol use disorder.

DIAMOND DIstribution of 3D Anisotropic MicrOstructural eNvironments in Diffusion-compartment imaging.

DICOM Digital Imaging and Communications in Medicine.

DLPFC DorsoLateral PreFrontal Cortex.

dMRI diffusion Magnetic Resonance Imaging.

DNA DeoxyriboNucleic Acid.

DTI Diffusion Tensor Imaging.

DW-MRI Diffusion-Weighted MRI.

FA Fractional Anisotropy.

FID Free Induction Decay.

fvf fiber volume fraction.

GM Gray Matter.

MD Mean Diffusivity.

MF Microstructure Fingerprinting.

MFI Multidimensional Fatigue Inventory.

MNI Montreal Neurological Institute.

MRI Magnetic Resonance Imaging.

NIfTI Neuroimaging Informatics Technology Initiative.

NMR Nuclear Magnetic Resonance.

NODDI Neurite Orientation Dispersion and Density Imaging.

OCDS Obsessive Compulsive Drinking Scale.

ODI orientation dispersion index.

OFC OrbitoFrontal Cortex.

PGSE Pulsed Gradient Spin-Echo.

PNS Peripheral Nervous System.

RD Radial Diffusivity.

RF Radio Frequency.

ROI Regions of Interest.

SE Spin Echo.

SNR Signal to Noise Ratio.

STAI State-Trait Anxiety Inventory.

T1 Time 1.

T2 Time 2.

TE Echo Time.

TEIQue Trait Emotional Intelligence Questionnaire.

TR Repetition Time.

WM White Matter.

Introduction

Alcohol Use Disorder is a medical condition characterised by an impaired ability to stop or control alcohol use [1]. This disability is a major concern in our society, given the amount of people affected and its consequences on public health. As a matter of fact, up to 3.3 million people die every year worldwide as a result of alcohol abuse, accounting for 6% of the world's deaths [2].

This consumption has inevitable impacts on the consumer's health status, on both a physical and mental plan, including high variations in the brain microstructure that open a large field of research. To this end, Magnetic Resonance Imaging (MRI) and in particular diffusion Magnetic Resonance Imaging (dMRI) has proven to be of great interest to observe and quantify those microstructural changes. dMRI aims to highlight the microscopic movements of water in the tissues, thus providing indirect information about the structure surrounding these water molecules. Some variables can then be extracted of such imaging techniques and be translated in terms of axonal density, white matter integrity, swelling and other parameters [3, 4]. A well known model to retrieve this type of information is the Diffusion Tensor Imaging (DTI).

Based on this principle, some new useful models such as Neurite Orientation Dispersion and Density Imaging (NODDI), DIstribution of 3D Anisotropic MicroStructural eNvironments in Diffusion-compartment imaging (DIAMOND) and Microstructure Fingerprinting (MF) have been implemented upon these dMRI sequences to further characterize the microstructure. They all have something in common: the decomposition of each single voxel into a sum of different compartments, allowing a more accurate representation of the different components present in the voxels.

The goals of this thesis are to analyse and summarise the critical microstructural changes induced by alcohol abstinence in patients suffering from AUD. This early abstinence step is a key phase in the treatment of AUD because patients are more prone to relapse [5].

This paper will therefore be structured in the following way. First, a theoretical background and literature review will be established in order to introduce the main concepts of this research, namely MRI and AUD. Second, a quantitative analysis of the microstructural changes induced by a supervised three weeks withdrawal with alcoholic patients will be performed. Third, a discussion will be made upon the different results and their interpretation before concluding about the interest of this short term abstinence process. Finally, this work will be concluded by identifying the limitations of the work performed and summarizing the important findings of this research.

Part I

State of the art

1 Magnetic Resonance Imaging

Neuroimaging is the set of techniques using mathematical and computer tools to reconstruct structural and functional images of the brain, from signals detected by specialised equipment. Magnetic Resonance Imaging (MRI) is one such technique. It is used for both structural and functional imaging, respectively to study the structure of the brain and to study cognitive processes in healthy subjects or those with neurological and/or psychiatric pathologies [6].

1.1 Nuclear Magnetic Resonance

MRI is based on the behavior of the hydrogen atoms which constitute a large part of the body. The latter is made of two particles: one positively charged, a proton and the other negatively charged, an electron. The proton is a particle having the particularity of spinning on itself, thus inducing a kinetic momentum, also called a spin (see Figure 1.1A). The latter is an intrinsic property of the proton. Furthermore, as it is a charged particle that is rotating, it will produce a magnetic field called magnetic moment $\vec{\mu}$ that is aligned with its axis of rotation (see Figure 1.1B) and will lead to a resonance phenomenon [6].

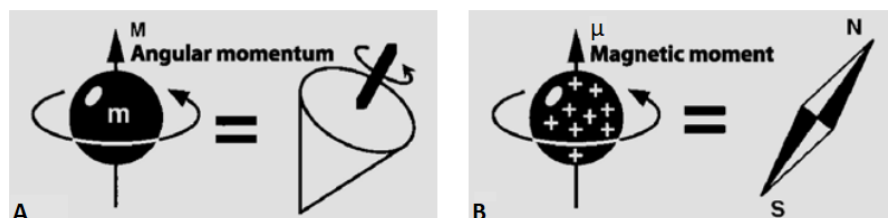


Figure 1.1: **A** Representation of the kinetic momentum or so-called spin and **B** the magnetic moment of a particle. Adapted from [7].

A parallel can be done between a proton and a magnet composed of a North and a South pole: in the absence of external field, the protons will be randomly oriented as depicted on Figure 1.2A. The sum of all the microscopic magnetisations $\vec{\mu}$ is equal to zero, meaning that there is no resulting magnetisation at the macroscopic scale, $\vec{M} = 0$. However, as said before, a proton is a charge which, when placed in an external magnetic field B_0 , will tend to align itself with the field (along its main direction). This will lead to a macroscopic magnetisation vector \vec{M} appearing (see Figure 1.2B). The latter is defined as the sum of a longitudinal component \vec{M}_z and a transverse one \vec{M}_{xy} .

Moreover, they can take two different orientations: either parallel or anti-parallel to B_0 . But in reality, the protons are not perfectly aligned with B_0 . They are rotating with a given angle and a given angular frequency around B_0 . This

phenomenon is called precession and is quantified by the Larmor equation:

$$\omega_0 = \gamma B_0,$$

$$\nu_0 = \frac{\gamma}{2\pi} B_0,$$

where ω_0 is the Larmor angular frequency and ν_0 is the Larmor frequency. The other parameters are γ , the gyromagnetic factor and B_0 , the external magnetic field [4, 7, 6, 8].

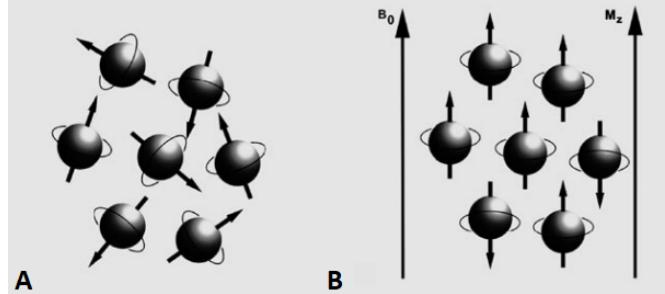


Figure 1.2: **A** Representation of protons when no magnetic field is applied, they are rotating around their axes in random direction; **B** Protons aligned in the direction of the external field B_0 , a few more in the parallel direction and thus inducing a longitudinal magnetization. Adapted from [7].

As protons are particles that follow quantum mechanics, these two possible orientations can be associated to two different levels of energy: low energy level representing the case in which the magnetization vector is parallel to B_0 , and high energy level corresponding to the opposite situation, with a magnetization vector anti-parallel to B_0 . The distribution of the protons between these two populations is quite equivalent but there is a little excess in the population corresponding to the low energy level. This difference, at 0.5 Tesla and at body temperature, is of the order of 2 protons per million. In other words, in a tissue sample, if a set of one million protons are aligned in the anti-parallel direction, then another million and four more protons in excess will have a parallel orientation. In the end, this gives a non-zero macroscopic magnetisation. This is the steady state of a tissue sample [4, 7, 6, 8, 9].

This equilibrium state is a thermal equilibrium state, maintaining a transition between the two energy levels and the number of parallel protons in excess. There is a certain gap ΔE between the two energy levels:

$$\begin{aligned}\Delta E &= h\nu_r, \\ &= h\frac{\gamma B_0}{2\pi} = \hbar\omega_0, \\ &= E_\downarrow - E_\uparrow,\end{aligned}$$

where $E_\uparrow (< 0)$ is the proton's energy when it is in the parallel orientation, $E_\downarrow (> 0)$ is the proton's energy when it is in the anti-parallel orientation and $h = \hbar/2\pi$ Planck constant. One can also compute the energy level E in the following way:

$$E = \pm\gamma\hbar B_0.$$

An electromagnetic wave equal to this difference (ΔE) must therefore be supplied to move the protons from one state to the other.

The ratio of the number of protons either in one or in the other orientation is characterised by the Boltzmann equation as follow:

$$\frac{N_\uparrow}{N_\downarrow} = e^{\frac{\Delta E}{kT}},$$

where N_\uparrow is the number of protons on E_\uparrow and N_\downarrow the one on E_\downarrow , T is the temperature in Kelvin and k is the Boltzmann constant.

At first, B_0 is aligned with the vertical axis \mathcal{O}_z of the reference system. Regarding the magnetisation, the longitudinal component is not null as there is an excess of proton in the parallel population which gives a non zero resultant, but there is no transverse component as the microscopic transverse components all compensate each other. Before the application of the Radio Frequency (RF) pulse, protons are all out of phase. Then, by applying a rotating magnetic field B_1 along \mathcal{O}_x , this steady state can be disturbed. Indeed, it brings some energy to the system and will allow protons to change their energy level. However, a condition must be fulfilled to enable this phenomenon: the rotation frequency (ω_r) of B_1 , a RF wave, must be equal to the specific Larmor frequency ω_0 of the protons in the field B_0 , leading to:

$$\begin{aligned}\omega_r &= \omega_0, \\ \omega_1 &= \gamma B_1.\end{aligned}$$

Both systems are therefore in resonance and the protons oscillate at both the precession angular frequency ω_0 (around B_0) and ω_1 (around B_1). Generally, the RF wave is applied during a short period of time and can thus be seen as an impulse. Its short duration (a few milliseconds) will be such that the magnetization vector will either be tilted from an angle of 90° or 180° , as illustrated in Figure 1.3 [4, 7, 6, 8].

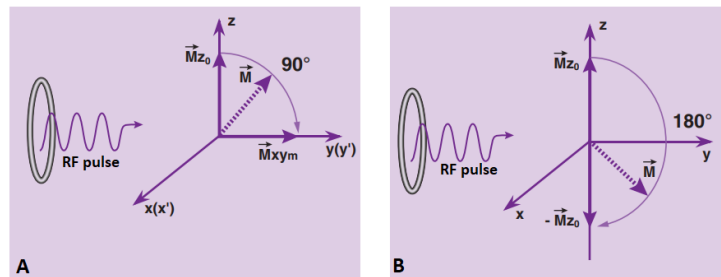


Figure 1.3: Impact of different RF pulses on the macroscopic magnetization vector \vec{M} : **A** 90° RF pulse and **B** 180° RF [4].

Thus, by applying a RF pulse of 90° as shown in Figure 1.4B, protons from the low energy level might receive enough energy to go to the high energy level. When the protons number is equivalent between the two energy levels, the longitudinal magnetisation is null and the transverse one is maximum. However, if a 180° RF pulse is applied, all the excess protons will shift from the E_\uparrow level to the E_\downarrow level, which leads to the inversion of the longitudinal component as shown in Figure 1.4C [4, 6, 8].

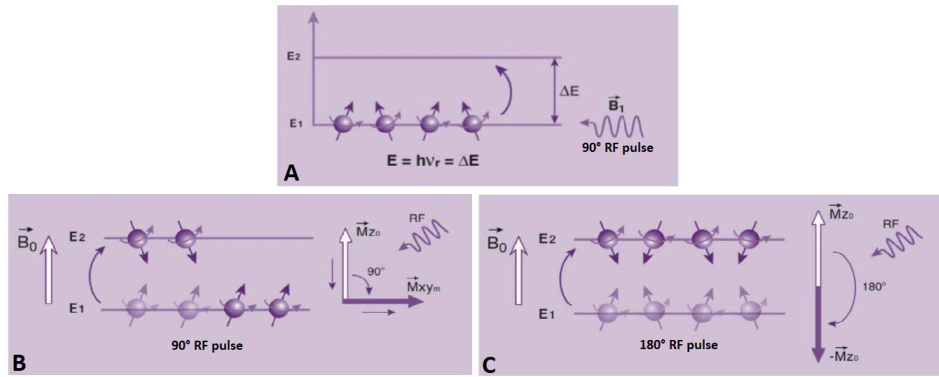


Figure 1.4: Impact of different RF pulses on the 4 excess protons: **A** Before and **B** after the 90° RF pulse and **C** after the 180° RF pulse. Adapted from [4].

The state described in the previous paragraph is unstable and at the end of the excitation, there will be a return to the equilibrium state (i.e. the one represented in Figure 1.4A). This is achieved by inverse phenomena: inverse transitions towards lower energy states and a phase shift of the spins. In the first case, the longitudinal magnetisation will gradually grow back (T_1 relaxation). In the second case, the spin dephasing will cause a rapid decrease in the transverse magnetisation (T_2 relaxation). It is through the relaxation of protons that the phenomenon of Nuclear Magnetic Resonance (NMR) can be observed [4, 7, 6, 8].

1.1.1 Relaxation

The appearance and disappearance of the longitudinal and transverse component are governed by two distinct mechanisms: the energetic transition of the protons from one level to another and the phasing of the protons.

T_1 relaxation

Considering the first mechanism, a 90° RF pulse will bring energy to the system: protons are going to absorb it and move from E_\downarrow , the lower energy level, to E_\uparrow the higher one. This will lead to progressive disappearance of the longitudinal component of \vec{M} . As soon as B_1 is stopped, the system returns to its equilibrium state and uses the inverse mechanism: emission of the previously absorbed energy characterising the return of the protons to the low energy level. However, to ensure that the protons transfer energy to the surrounding biological medium, the spontaneous Larmor frequency must be close to the frequency of molecular collisions of protons. Regarding the longitudinal component, it will progressively increase following this equation:

$$\vec{M}_z(t) = \vec{M}_0(1 - e^{\frac{-t}{T_1}}). \quad (1.1)$$

It is called the longitudinal relaxation or spin-lattice relaxation. This phenomenon can be described by the Figure 1.5.

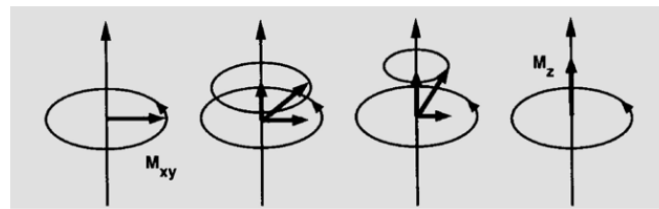


Figure 1.5: Illustration of the evolution of both components of magnetization during T_1 relaxation: decrease of transverse and regrowth of the longitudinal component [7].

As in Equation 1.1, regrowth occurs according to an increasing exponential curve where the time constant T_1 is characteristic of a given tissue. This equation means that after a period of time equal to T_1 , 63% of the longitudinal component has regrown; for $2T_1$, the regrowth is 87% and for $3T_1$ it is almost total (about 95% are recovered). The longitudinal magnetisation grows faster as the time constant T_1 is smaller [4, 7, 6, 9, 10].

T_2 relaxation

The second mechanism involves the phase shift and rephasing of protons regarding the evolution of the transverse magnetisation. During the pulse, the protons come into phase with each other. But when the pulse stops, the protons will gradually become out of phase or lose their phase coherence. This is known as transverse relaxation or spin-spin relaxation because this phenomenon results from the interactions of the protons with each other. Indeed, the protons will evolve in slightly different molecular environments: they will not have exactly the same Larmor frequency. This will create small magnetic fields which will be superimposed locally on the main one, B_0 . This will create inhomogeneities in B_0 which are from molecular origin. This is why, before and after the application of the pulse, the protons are not in phase and do not remain in phase for long. In this case, no energy exchange is involved in this process and it is called T_2 relaxation because the disappearance of the transverse magnetization occurs according to a decreasing exponential,

$$\vec{M}_{xy}(t) = \vec{M}_0 e^{\frac{-t}{T_2}}, \quad (1.2)$$

where the time constant T_2 is also characteristic of the tissue concerned. During the first T_2 seconds, nearly 63% of the transverse component has already disappeared, as characterised by Equation 1.2. An additional T_2 period results in the attenuation of 87% of this component, whereas the latter is almost complete (i.e. 95%) after $3T_2$ seconds. Respectively, the magnitude of order for T_1 and T_2 , are 500 to 1000ms and 50 to 100ms [4, 7, 6, 11].

Considering inhomogeneities with T_2^*

The signal measured in MRI technology is called the Free Induction Decay (FID) signal and corresponds to the decay of the transverse magnetisation M_{xy} . Indeed, if the magnetic field B_0 were perfectly homogeneous, the observed decay would be according to the time constant T_2 . However, this is not the case, as B_0 can only be considered homogeneous on a macroscopic point of view. At the microscopic scale, due to hardware limitation, B_0 is not perfectly homogeneous [12, 13]. These inhomogeneities are constant and lead to an increased phase shift of the spins. The FID signal is therefore linked to two phenomena: on the one hand, there

are the inhomogeneities of B_0 which are following T_2 , or the so-called molecular inhomogeneities and on the other hand, are added the inhomogeneities of the external magnetic field B_0 itself and linked to the setup. The time constant T_2^* will be used to represent the effect of this combination. Accordingly, the FID signal decreases more rapidly, following an exponential in T_2^* as depicted in Figure 1.6, since the inhomogeneities in B_0 accelerate the phase shift of the spins considerably [4, 7, 6].

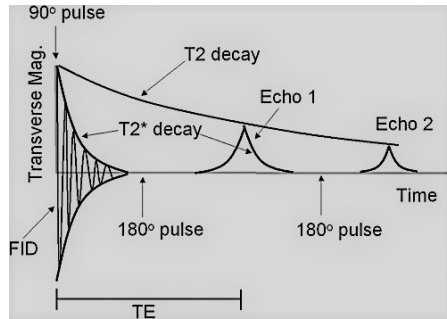


Figure 1.6: Illustration of a sequence creating spin echoes. First, application of a 90° RF pulse leading to a FID signal. The latter is dephased due to T_2^* effects. Then, a refocusing 180° RF pulse is applied, allowing the formation of an echo at time TE [12].

1.1.2 Spin Echo sequence

To get rid of the constant inhomogeneities of the B_0 field, a Spin Echo (SE) sequence can be used. It will allow to access the true T_2 and cancel the protons' dephasing. As shown in Figure 1.7, this sequence is composed of a 90° RF pulse followed by a 180° RF pulse aiming to correct the phase shift induced by the B_0 field. It will allow to obtain a signal following T_2 and not T_2^* . This signal coming from the evolution of transversal magnetization is called echo (purple box on Figure 1.7) [8].

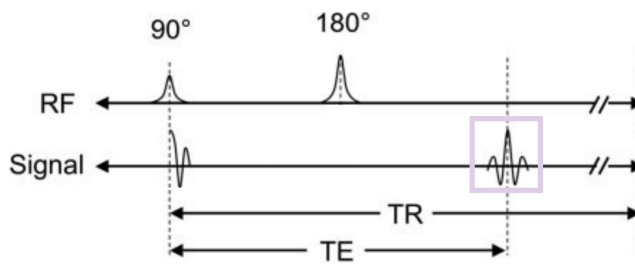


Figure 1.7: Spin Echo (SE) sequence. Adapted from [12].

There are two important time constants in a SE sequence:

- Echo Time (TE): the measurement time or the time between the 90° pulse and the first echo;
- Repetition Time (TR): the time interval between two pulses of 90° or the time of longitudinal magnetisation recovery.

Thus, a 180° RF pulse is applied at time $t = TE/2$. This will cause a rephasing of the spins that were previously out of phase by the action of the 90° RF pulse.

They will be rephased at time $t = TE$: the signal then reappears as an echo and can be measured. However, the spins are not perfectly aligned parallel to the O_z axis of the reference frame. This difference between the initial state and the new state is the consequence of spin-spin relaxation; the vector of the transverse magnetisation (i.e. the measured signal) is slightly smaller than the one obtained with the first 90° RF pulse [4, 7, 12, 8].

SE is the most widely used sequence in imaging techniques. It provides excellent quality images, whose T_1 and T_2 weighting can be determined by a judicious choice of the parameters TR and TE. However, one of the disadvantages of this sequence is that it is relatively long. We will see in the section 1.1.4 how this cycle is used to obtain the image matrix and thus recover the full information.

1.1.3 Image contrast

Contrast is used in MRI to show differences in relaxation times and proton density. By means of these different contrasts, it is possible to visualise the different components of the brain such as White Matter (WM), Gray Matter (GM) and Cerebrospinal fluid (CSF). Indeed, these biologically soft tissues are characterised by different relaxation times: WM has the shortest T_1 and T_2 , GM has intermediate values and CSF has the longest ones. By choosing the parameters (TR and TE) of the SE sequence carefully, it is possible to weight the sequence according to three types of contrasts:

- **T_1 contrast:** characterised by a short TR (to promote T_1 weighting) and a short TE (to minimise T_2 effects). The parameter characterising T1-weighted images is TR. Indeed, short TR will give higher contrast than long ones, as shown in Figure 1.8, because at long TR, tissues are almost completely relaxed and it is therefore very difficult to differentiate them: the longitudinal component is at its steady state. The shorter T_1 , the higher the signal (i.e. appear white on image). This contrast makes the WM white or light gray, the GM gray and the CSF black [4, 7, 6];

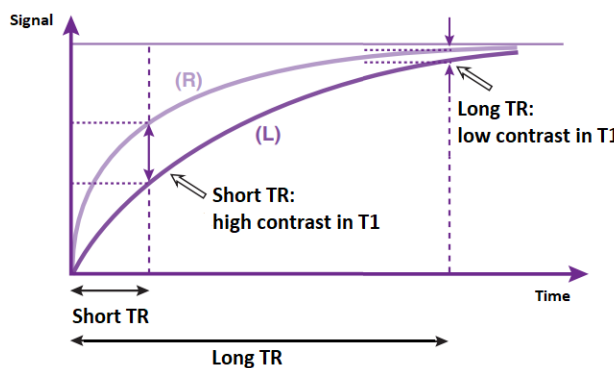


Figure 1.8: Evolution of the signal of two tissues either with a long TR or a short one leading respectively to low and high T_1 contrast. Adapted from [4].

- **T_2 contrast:** characterised by a long TR (to minimise T_1 effects) and a long TE (to promote T_2 weighting). In this case, it is TE that characterises T2-weighted images (see Figure 1.9). At short TE, the T_2 relaxation has

just started and there is a big loss of information in the measured signal. Therefore, the longer T_2 , the higher the signal (i.e. white on image). This contrast makes the WM darker, the CSF white and the GM is in between [4, 7, 6];

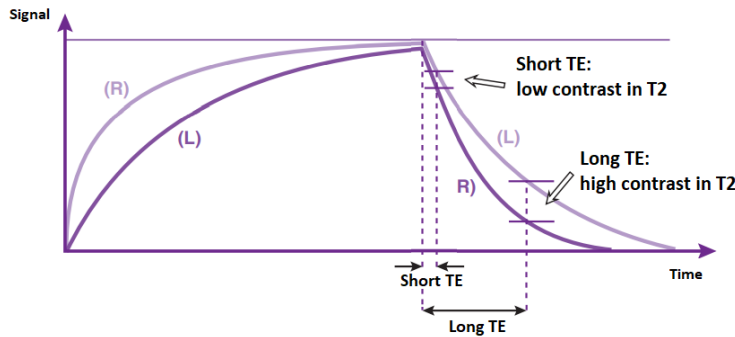


Figure 1.9: Evolution of the signal of two tissues either with a long TE or a short one leading respectively to high and low T_2 contrast. Adapted from [4].

- **Proton density contrast:** characterised by a long TR (to minimise T_1 effects) and a short TE (to minimise T_2 effects). A combination of both parameters is needed for this type of contrast: long TR allows the recovery of longitudinal magnetization while short TE minimizes the signal decrease due to the decay of transverse magnetization (see Figure 1.10) [4, 7, 6].

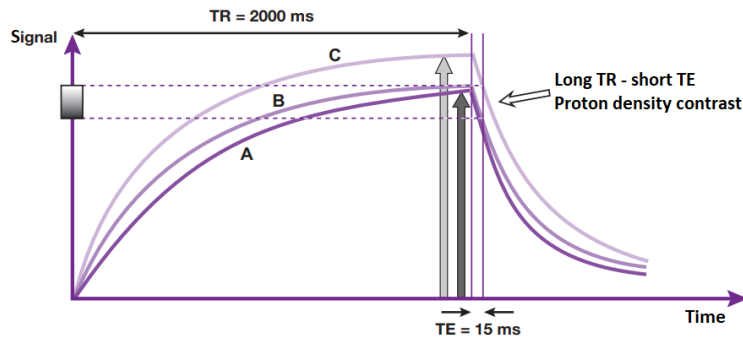


Figure 1.10: Evolution of the signal of three tissues with tissues A and B with the same proton density and tissue C with a different one. Thus, there is contrast between tissue C and tissues A or B but no contrast between A and B as there is no signal difference after a TR time. Adapted from [4].

1.1.4 Acquisition

To obtain an image, it is necessary to add spatial information to the signal in order to assign a position to the different received signals. First, a slice plane has to be selected. After that, the horizontal and vertical directions must be defined on the slice plane. The collected RF signals then have to be spatially processed in order to reconstruct the image.

Spatial encoding is based on the successive application of magnetic field gradients. First, a slice selection gradient ($G_{ss} - G_z$) is used to select the anatomical volume to be explored. Within this volume, the position of each point will be

encoded vertically and horizontally by applying a phase encoding gradient ($G_\phi - G_y$) and a frequency encoding gradient ($G_\omega - G_x$) respectively. These different gradients that enable spatial coding have identical properties, but are applied at different times and in different directions.

The first step in spatial encoding is to select the slice plane: the slice selection gradient (G_{ss}) is applied in a direction perpendicular to the plane of interest. It is added to B_0 which will affect the behavior of only protons contained in this plane. Simultaneously, an RF wave is applied with a frequency equal to the one of the protons of interest (resonance phenomenon) resulting in a tilting of the magnetization of only the protons in this plane. Any hydrogen nuclei outside the slice plane will not be excited and therefore will not deliver any signal [4, 7, 8].

These protons will then be stimulated again by magnetic field gradients to encode their position in the horizontal and vertical directions. The slice selection gradient is applied simultaneously to all the RF waves: 90° and 180° . To compensate for the phase shifts induced by the G_{ss} gradient, which is associated with the first RF pulse, a gradient of inverse polarity of half duration with respect to the first positive lobe (gradient of ratio $+2/-1$ as shown in Figure 1.11) must be added to the two first positive lobes of G_{ss} . Thus, the protons are back in phase before the application of subsequent gradients to code the selected slice, avoiding signal loss. However, the 180° pulse used to rephase the spins will also cause the modification of unwanted spins. To avoid this phenomenon, two lobes of identical gradients can be added on either side of the 180° RF pulse, as shown in Figure 1.12.

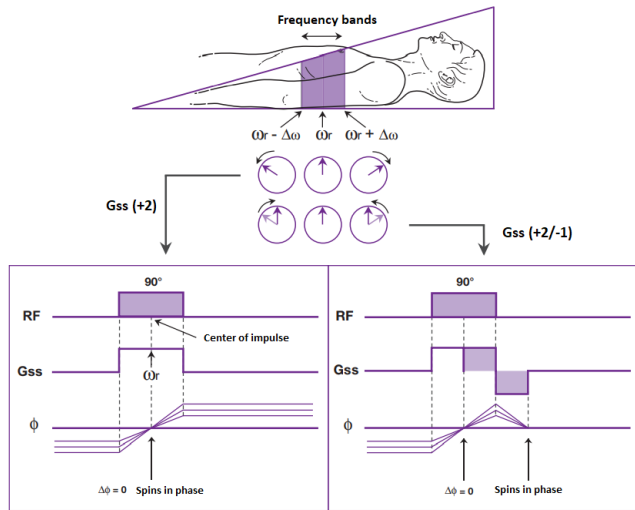


Figure 1.11: Addition of a negative lobe of half duration to the first positive lobe of the G_{ss} gradient to compensate for the phase shifts it induces. Adapted from [4].

The second step is to apply a phase encoding gradient, G_ϕ , in the vertical direction. Protons located on the same line, perpendicular to the gradient direction, will all have the same phase but different from the other ones. This phase shift continues until the signal is collected. When the signal is collected, each line of protons will have a certain phase shift. This will result in a greater or smaller shift in their signals [4, 7, 8].

The final step in spatial coding is to apply a frequency coding gradient, G_ω , in

the horizontal direction during the signal collection. It will change the precession frequencies in this direction for the duration of its application. Nevertheless, the use of a gradient reduces the available signal. Actually, in order to receive a high signal, the SE created by the 180 RF pulse and the gradient echo generated by the bipositive G_ω gradient must coincide. Hence, the first lobe (+1) of this gradient is the source of a phase shift that compensates, in advance, for the phase shifts caused by the reading gradient (+2). As this second gradient (+2) is applied simultaneously with the signal collection, the signal will still carry the frequencies but also the phase shifts created upstream by G_ϕ .

Finally, in order to obtain a complete plane, additional lines must be generated. To do this, this cycle must be repeated, using the same RF pulses and the same frequency encoding gradient, but increasing or decreasing the amplitude of the phase encoding gradient in order to obtain different information at the moment of reading the signal. To achieve these different phase encoding steps, the gradient is applied with different values, incremented in a regular way. It is said to be bipolar, i.e. with positive and negative values, symmetrical with respect to 0 [4, 7, 8].

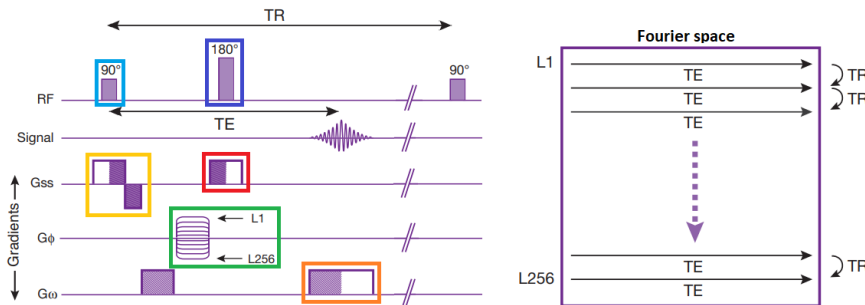


Figure 1.12: Complete timeline of gradient placement in the spin echo sequence: **Light blue box** - 90° RF pulse with ω_0 frequency; **Dark blue box** - 180° RF pulse used to rephase the spins; **Yellow box** - G_{ss} gradient composed by a positive lobe and a reverse polarity gradient of half the duration of the first positive one; **Red box** - G_{ss} gradient composed by two positive lobes on either side of the 180° pulse; **Green box** - G_ϕ phase encoding gradient going from a positive value to the same negative one; **Orange box** - bipositive G_ω gradient. Adapted from [4].

The time between two complete cycles, and therefore the time between the end of one line and the beginning of the next one in the Fourier plane (also known as the K-space) is the TR. At each repetition, a line of the K-space is filled, thanks to a different phase encoding as shown on the right of Figure 1.12. To sum up, the data acquisition is obtained line by line by a double progression: horizontal, reading the same line thanks to the frequency encoding by the readout gradient G_ω , and vertical, from one line to the next thanks to the change of the phase encoding gradient G_ϕ to obtain successively all the lines of the Fourier plane [4, 7, 8].

1.2 Diffusion imaging techniques

1.2.1 Diffusion-Weighted MRI

The main benefit of using Diffusion-Weighted MRI (DW-MRI) is that it relies on the principle of diffusion of water molecules in the body. Indeed, their displacements,

characterised as Brownian¹, allow the extraction of information on the structure of tissues at a microscopic scale, thus offering a much higher quality of resolution [4, 15]. The diffusivity of a molecule is directly influenced by the composition of its surrounding environment (i.e. the type of tissue, the type of molecule,...), by the microscopic architecture of this tissue and by the temperature. This is leading to two types of movement [16, 15]:

- **Free diffusion:** water molecules move in all directions in space, without any constraints. For example, CSF meets this criterion.
- **Restricted diffusion** which can be divided into two subcategories: isotropic, when the degree of diffusion is the same in all directions of space, and anisotropic, when it is different only in some directions of space. Both are, as the name implies, limited by obstacles. For instance, the diffusion in central GM is isotropic whereas it is highly anisotropic in the case of axons in which diffusion is facilitated along the axonal fibers, in the longitudinal direction but less in the perpendicular direction.

The observation of these displacements can therefore provide unique insights on the structure and organisation of tissues. MRI is the only non-invasive technique currently available to observe diffusion *in vivo* [17]. Moreover, this method does not interfere with the diffusion process: it is an intrinsic physical process, independent of the physical magnetic principles used [18].

Diffusion imaging can therefore provide indirect information, such as microstructural properties of the tissue surrounding the water particles. Indeed, it is possible to access the information given by the agitation of the water molecules because it is an integral part of the MRI signal: only molecular displacements in the direction of the gradient are visible and will therefore influence the signal. However, the sequences usually used and described above are not powerful enough to highlight the loss of signal due to this phenomenon. To overcome this problem, a new sequence is used: Pulsed Gradient Spin-Echo (PGSE) sequence containing two diffusion gradients, symmetrically to the 180° RF pulse, as shown in Figure 1.13 [19, 4].

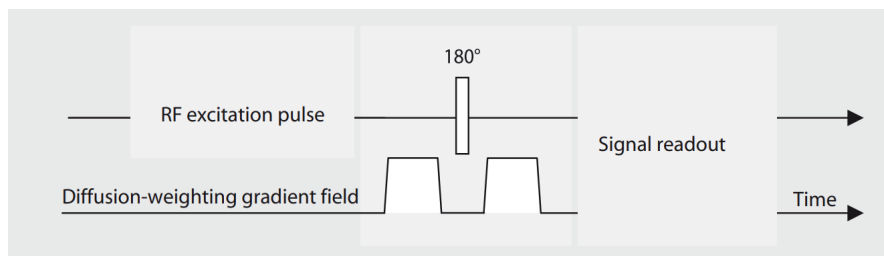


Figure 1.13: Diffusion gradient in a PGSE sequence [7].

These two gradients are added in order to be able to measure the diffusivity of water molecules, within a voxel, through T_2^* signal attenuation. Two cases must be considered: immobile and mobile water molecules. In the first case, the phase shift caused by the first diffusion gradient is perfectly compensated by the second one. The signal of such molecules is therefore not attenuated and is represented by the

¹Brownian motion is the random movement of particles in a liquid or gas [14]

white arrow in Figure 1.14. However, in the second case, the mobile protons are dephased when the first gradient is applied. But as they are moving, they are not exposed to precisely the same diffusion gradient after being under the influence of the 180 degree refocusing pulse. This results in an attenuation of the signal, represented by the gray arrow in Figure 1.14. The speed of molecular movements has an impact on the attenuation of the signal. Indeed, the faster it is, the less the phase shift of the protons will be compensated for and the greater the decrease in signal. This is illustrated by the black arrow in Figure 1.14 [4, 18, 20].

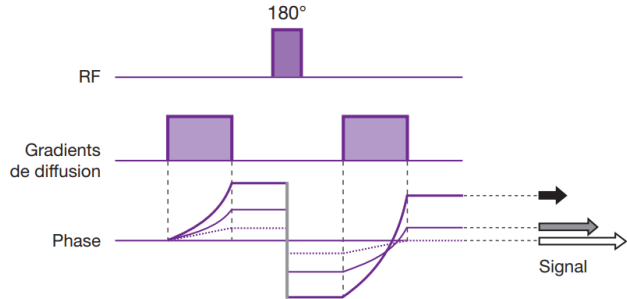


Figure 1.14: Diffusion gradients and their effects on signal [4].

Figure 1.15 is another way to explain the previous paragraph. Indeed, this graph shows how motion of protons will affect the signal. The bottom right rectangle shows that not all protons have been rephased to their initial state because they have moved and therefore have not been subjected to the same field strength as before [21].

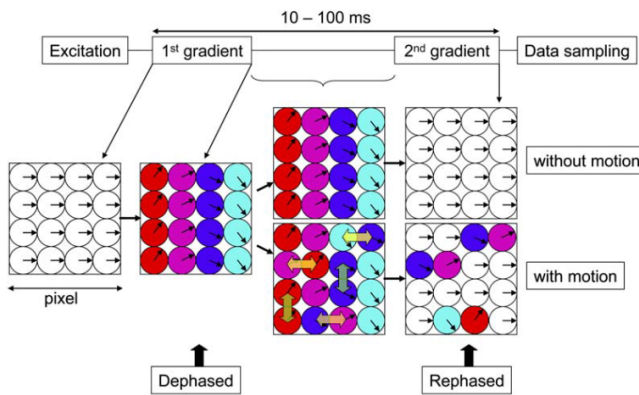


Figure 1.15: Influence of motion on proton phase [21].

The attenuation of the MR signal can be improved by varying the amplitude and time of application of the scattering gradients. These characteristics are combined into a single value called the b-value. It is defined by the following equation [16, 4]:

$$b = (\gamma G \tau)^2 (T - \frac{\tau}{3}) [s/mm^2],$$

with γ the gyromagnetic ratio, G the gradient amplitude, τ the time during which it is applied and T the time between the onset of both diffusion gradient.

This is a metric that quantifies the diffusion weighting in MRI sequences: using a high b-value, the signal will show more attenuation in opposition to the use of a

low b-value. Indeed, a b-value of zero gives no diffusion weighting in the image. Conversely, a high value of b allows to better highlight the differences in diffusion speed.

Another interesting coefficient is the Apparent Diffusion Coefficient (ADC). It represents the rate of diffusion in biological tissues [16]. To be able to compute this coefficient, two DW-MRI acquisitions are needed: one using a b-value equal to zero allowing, as said before, to have no diffusion effects and the other one using a b-value which is different from zero. These two acquisitions are going to give a signal S_0 and a signal S respectively that can be put together into the following formula [4, 18]:

$$ADC = -\log\left(\frac{S}{S_0}\right)/b \text{ [mm}^2/\text{s}],$$

where b is the b-value used to make the acquisition of the signal S .

However, this coefficient is highly influenced by the direction used to encode diffusion. By averaging three measurements made in orthogonal directions, it is possible to resolve this limitation. This new image is called the trace image and gives a better estimate of the scattering phenomenon. Indeed, a hypersignal on this image will correspond to a restricted diffusion in the three directions [4].

1.2.2 Diffusion Tensor Imaging (DTI)

The effect of diffusion on the MRI signal is characterised by an attenuation. It is linked to the b-value and to the ADC [4]:

$$Att = e^{-b \cdot ADC}.$$

However, the ADC coefficient does not take into account the possibility for the diffusion to be anisotropic, making it dependent on the direction of the applied gradient. To take that into account, instead of a scalar, a tensor will be used to define the diffusion. This technique is called Diffusion Tensor Imaging (DTI) is able to extract diffusion anisotropy effect from MRI [4, 22, 18]. This diffusion tensor $\overline{\overline{\mathbf{D}}}$ is defined as follows:

$$\overline{\overline{\mathbf{D}}} = \begin{pmatrix} D_{xx} & D_{xy} & D_{xz} \\ D_{yx} & D_{yy} & D_{yz} \\ D_{zx} & D_{zy} & D_{zz} \end{pmatrix}.$$

This tensor is symmetric meaning that $D_{xy} = D_{yx}$; $D_{xz} = D_{zx}$ and $D_{zy} = D_{yz}$. Thus, to acquire this tensor, DW-MRI sequence is only needed in six different directions. As said before, a seventh measurement is performed with a low b value ($b=0$) to have a baseline image. These 7 measurements are the minimum required for solving the diffusion coefficients characterising the diffusion tensor [18, 23]. The diagonal elements of $\overline{\overline{\mathbf{D}}}$ represent diffusion along the three orthogonal axes of the referential frame.

From this tensor, scalar quantities can be obtained by using its eigenvalues λ_1 , λ_2 and λ_3 . The latter are defined by means of the following equation:

$$\begin{aligned} (\mathbf{D} - \lambda \mathbf{I})\mathbf{u} &= 0, \\ (\mathbf{D} - \Lambda)\mathbf{u} &= 0, \end{aligned}$$

where Λ is the matrix containing the three eigenvalues on its diagonal and \mathbf{u} is the matrix containing the corresponding eigenvectors [4, 17, 18].

Mean Diffusivity (MD)

The MD is a measure of the overall diffusivity in a particular voxel and the overall presence of diffusion barriers. To obtain this global characterisation of diffusion in one voxel, anisotropic effects must be avoided and the Trace (Tr) of the diffusion tensor ($\bar{\bar{\mathbf{D}}}$), as it is a quantity independent of the directions, is a good indicator of the global diffusivity in a given voxel, also translating the amount of water in the extracellular space [24, 18]. The latter is calculated as the sum of the three eigenvalues λ_1 , λ_2 and λ_3 :

$$Tr(D) = \lambda_1 + \lambda_2 + \lambda_3, \quad (1.3)$$

$$MD = \frac{Tr(D)}{3} = \frac{\lambda_1 + \lambda_2 + \lambda_3}{3}. \quad (1.4)$$

MD will be low within the WM and the GM as the diffusion is mainly anisotropic in these regions but will be quite high in other structures such as CSF, as movements of water molecules are less restricted. On Figure 1.17A, a MD map is displayed: pixels with low MD values appear dark and those with high values appear bright. Moreover, as this metric is completely independent of the direction of the frame of reference (by contrast to the ADC), its changes will only be due to changes in the structure of the tissue [22, 18].

Axial Diffusivity (AD)

AD is another way to characterise the diffusion. It represents the diffusivity along the principal axis of the diffusion ellipsoid and is given by λ_1 [23].

$$AD = \lambda_1. \quad (1.5)$$

Radial Diffusivity (RD)

RD is the expression of the diffusivity along perpendicular direction to the principal one [23]:

$$RD = \frac{\lambda_2 + \lambda_3}{2}. \quad (1.6)$$

With the definition of those three diffusion metrics, the following equation enables to link them with each other:

$$3MD = AD + 2RD. \quad (1.7)$$

Fractional Anisotropy (FA)

It is also possible to obtain information about the degree of anisotropy of a voxel. The behavior of water molecules with respect to orientation can be described thanks to this last metric which is called FA. It is defined as the ratio of the degree of anisotropy of $\bar{\bar{\mathbf{D}}}$ to the total diffusion tensor and quantifies its shape.

$$FA = \sqrt{\frac{3}{2}} \sqrt{\frac{(\lambda_1 - MD)^2 + (\lambda_2 - MD)^2 + (\lambda_3 - MD)^2}{\lambda_1^2 + \lambda_2^2 + \lambda_3^2}}. \quad (1.8)$$

FA can vary between [0, 1]:

- Zero represents the situation for which the isotropic diffusion is maximum and shapes the diffusion tensor as a perfect sphere;
- One represents the opposite situation, when the anisotropic diffusion is maximum. The tensor is then shaped as an ellipse, as displayed in Figure 1.16.

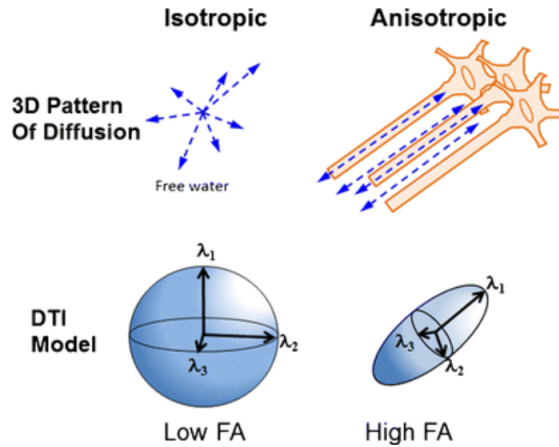


Figure 1.16: Evolution of the ellipse representing the diffusion tensor [22].

Once the four metrics are obtained for each voxel, a map can be created: voxels with high value of FA will appear bright whereas voxels with low FA value will appear dark on the image. Moreover, another map can be computed: Red-Green-Blue map of the FA (see Figure 1.17C). The latter gives indication on the direction of diffusion. In such maps, the red color indicates left-right, green anterior-posterior and blue superior-inferior direction of the diffusion [23, 16].

The four metrics introduced here above also have physiological/anatomical interpretations. First, FA reflects the integrity of microstructural connectivity underlying brain circuitry. High values of FA thus represent high WM integrity. Regarding diffusion metrics, AD is used to translate axonal integrity, meaning that low AD values can be a sign of axonal damage. Finally, RD is commonly used to speak about myelin integrity [25, 22, 24, 23, 18].

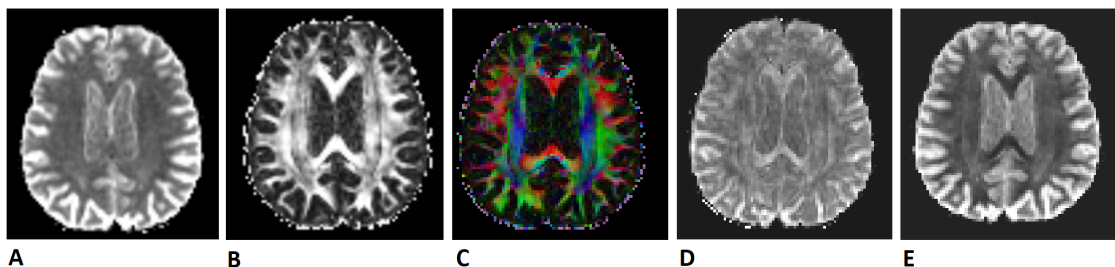


Figure 1.17: Axial slice of **A** MD map; **B** FA map; **C** RGB-FA map; **D** AD map and **E** RD map.

1.3 Advantages and limitations of DTI

DTI is a model with many advantages, but also some limitations. One of the main advantages of this model is that it allows the assessment of WM *in vivo* and

provides quantitative measurements in a non-invasive manner. However, although it can identify the location of major WM bundles, only one fiber population can be modelled in a voxel at the time and this does not represent reality. Moreover, DTI expects the water molecules to follow a Gaussian distribution and therefore does not take into account the impact of the specific microstructure of a voxel. Indeed, voxels are sometimes composed of multiple fiber populations which are crossing each other. This leads to misinterpretations: a voxel expressing low anisotropy may simply be due to populations of fibers, organised but oriented in different directions, whereas the DTI model will interpret it as a single unorganised population. The anisotropic character of the scattering will only appear on the DTI if, in a single voxel, all the structures passing through it are aligned in the same direction [26, 27].

Another limitation of DTI is that it is very sensitive and will therefore depend on many external factors such as acquisition parameters, the user, the scanner used, some non-biological factors (e.g. patient movement), etc. This has an impact on the quality of data that can be extracted from DTI. Indeed, they have a low Signal to Noise Ratio (SNR). The latter quantifies the ratio between the level of background noise and the level of the signal obtained. A low SNR represents poor image quality because the noise is too high compared to the signal [26, 27].

Finally, the DTI remains very interesting to study the evolution of neurological conditions because it has been shown to be very sensitive to brain damage and to the effects of neurological pathologies [27].

1.4 Advanced multi-compartment diffusion models

1.4.1 NODDI

Even though DTI has been the default method to investigate the brain microstructure for a few decades now, modern imaging tools and computing technologies give rise to new possibilities for even more detailed tissue characterisation, pushing research even further than before. This is the reason why new models such as Neurite Orientation Dispersion and Density Imaging (NODDI) are investigated in order to link the dMRI signals to tissue features. This goes beyond the simple signal representation enabled by DTI techniques and introduces a new biophysical model relying on assumptions about the underlying tissue [28].

NODDI is a microstructural model created in 2012 by Zhang et al. [29] in order to quantify neurites in terms of density and orientation inside an imaging voxel. Those parameters are significantly important for the interpretation of the brain development for example, as it has been shown that a higher dispersion of neurite orientation distribution in WM tracts translates a greater brain development [29]. This specific model allows to compensate for the non-specificity of DTI metrics. Indeed, a located decrease in FA might have several causes such as reduction in neurite density, increase in the dispersion of neurite orientation distribution, or many other structural changes [30].

The model is based on the discrimination of three different compartments: intracellular (ic), extracellular (ec) and CSF (iso). As the diffusion of water molecules is different in those areas, the resulting MR signal can also be differentiated. The

latter can be described with the following equation:

$$A = (1 - \nu_{iso})(\nu_{ic}A_{ic} + (1 - \nu_{ic})A_{ec}) + \nu_{iso}A_{iso},$$

where A and ν respectively represent the normalized signal and volume fraction for each of the three compartments. This voxel discrimination is made according to the anatomical constitution of the concerned element.[29]

First, the *intracellular model* applies to the elements located inside a neurite. A neurite is defined as a general term for axons and dendrites that are the projections of the cell body of a neuron. They are therefore responsible for the propagation of action potentials, carrying neural information. In this first compartment, the diffusion of water molecules is highly constrained by the shape of those neurites and is thus mainly parallel to their orientation. The model is therefore illustrated by a set of sticks, being cylinders of zero radius. The fraction of a voxel occupied by this intracellular compartment is characterised by fraction named **f_{intra}**, characterising how the fiber volume is evolving. Indeed, if **f_{intra}** increases in the WM, either the proportion of fibers in the considered area increases, thus showing axonal regrowth or the volume of fiber increased as a consequence of axonal swelling, thus translating a WM inflammation. On the other hand, if it decreases, the proportion or volume of fibers drops, which can, for example, be explained by inflammation of the extra-axonal space or axonal degeneration/deletion. However, its interpretation in the GM is quite different because it is not composed of any axonal fiber and thus will be more representative of what is happening to the proportion of microglial cells.

Second, the *extracellular model* designates the space surrounding the neurites, mainly composed of glial cells holding those neurites in place while providing them nutrients and oxygen, additionally to their protection role. The presence of neurites all around this compartment hinders the diffusion of water molecules but does not restrict it in a specific direction and this is modeled by a simple anisotropic diffusion. This is imaged by cylinders, having a principal parallel and a secondary perpendicular diffusivity component [29, 31]. The fraction of a voxel occupied by this extracellular compartment is characterised by fraction named **f_{extra}**. A higher value of **f_{extra}** can therefore be the sign of a higher quality of the myelin sheath, or a swelling of the extra-axonal cells due to inflammation.

Moreover, the fibers represented by sticks in this model can range from highly dispersed distributions in some brain areas, like the GM in which one can find dendritic processes in all directions, to a uniformly oriented distributions, in specific oriented WM structures such as the CC. This gives rise to a new metric, the orientation dispersion index (ODI), characterising each voxel corresponding to this model. The ODI ranges from 0 to 1 and locally translates the orientation dispersion in both, intra- and extracellular compartments. Hence, 0 stands for perfectly aligned fibers whereas 1 represents a fully isotropic structure [28, 29]. When ODI changes, it can have two meanings depending on the area of the brain in which it is located. In the WM, a decrease reflects axonal packing and an increase is a symbol of fiber dispersion. If it increases, it could thus reflect tissue rearrangement. On the other hand, the behavior of ODI in GM is quite different and a decrease illustrates a decline of the dendrites proportion whereas an increase expresses a rearrangement of the tissue or a neuroinflammation [28].

Third, the *isotropic model* refers to the compartment characterised by a fully isotropic diffusion [29]. It is sometimes referred to as the CSF compartment because of its high similarity with the diffusion observed in the ventricles full of CSF : isotropic diffusion of water molecules. It is however a misuse of language as this compartment is in reality not filled with CSF but with unconstrained molecules (or constrained in a sphere).

It is thus the combination of the CSF diffusion and the intra- and extracellular components, that builds the collected signal, as represented in Figure 1.18.

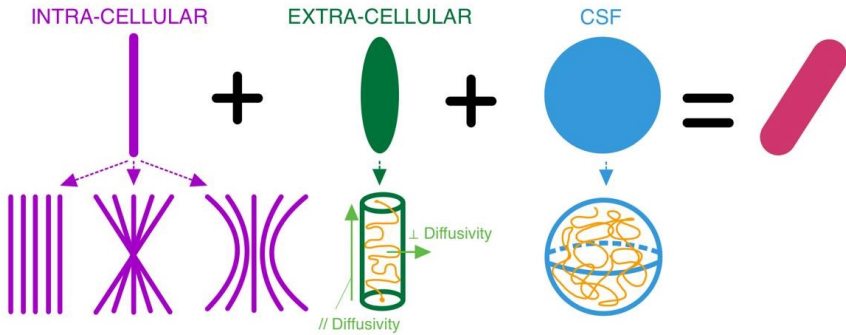


Figure 1.18: NODDI model: representation of the three compartments (intra-, extracellular and CSF) considered by this model. The intracellular compartment is represented by sticks (cylinders of zero radius). The extracellular space reflects the constrained diffusion with a cylinder, having both a longitudinal and a radial diffusivity components. The isotropic compartment (renamed CSF compartment) is represented by a sphere.

1.4.2 DIAMOND

DIstribution of 3D Anisotropic MicrOstructural eNvironments in Diffusion-compartment imaging (DIAMOND) is a microstructural model that takes into account all the information from the microstructures in the DW-MRI signal. This model, like NODDI, considers that in each voxel there are several compartments and does not consider the whole voxel as a single homogeneous population (see Figure 1.19A). Indeed, it considers a large number of spin packets in each voxel to provide insight into its composition. They are composed of homogeneous and heterogeneous 3D spin packets. The signal obtained for each voxel comes from homogeneous spin packets undergoing local anisotropic and Gaussian 3D diffusion. It represents the interactions of the spins with homogeneous parts of the microstructure. The diffusivity of homogeneous populations can therefore be represented by a diffusion tensor \mathbf{D} . Their contribution to the signal is weighted by $P(\mathbf{D})$, the matrix-variate distribution giving the fraction of spin packets characterised by a diffusion tensor \mathbf{D} leading to a diffusion signal S_k :

$$S_k = S_0 \int_D P(\mathbf{D}) e^{-b_k \mathbf{g}_k^T \mathbf{D} \mathbf{g}_k} d\mathbf{D},$$

where S_0 is the signal obtained for b_0 , the baseline signal, \mathbf{g}_k is the direction of the diffusion gradient direction and b_k is the b-value of volume k [32].

With the DTI model, voxels are considered to contain only one homogeneous microstructural environment. If the latter is characterised by a \mathbf{D}^0 diffusion tensor,

then it is possible to fall back on the DIAMOND model by defining $P(\mathbf{D})$ as a delta function: $P(\mathbf{D}) = \delta(\mathbf{D} - \mathbf{D}^0)$. However, this is not a realistic way to define a voxel. Indeed, they are often composed of several distinct compartments containing some amount of heterogeneity and this can be taken into account in the model by considering $P(\mathbf{D})$ as a matrix-variate Gamma ($mv-\Gamma$) distribution. The latter is defined as follows:

$$P_{\kappa, \sum}(\mathbf{D}) = \frac{|\mathbf{D}|^{\kappa-(p+1)/2}}{|\sum|^{\kappa} \Gamma_p(\kappa)} e^{-\text{trace}(\sum^{-1} \mathbf{D})},$$

$$\Gamma_p(\kappa) = \pi^{p(p-1)/4} \prod_{j=1}^p \Gamma(\kappa - (j-1)/2),$$

with κ the shape parameter capturing heterogeneity of the spin packet population, \sum the scale parameter and $\Gamma_p(\kappa)$ the multivariate Gamma function. If the latter has a narrow peak, it indicates a quite homogeneous population whereas broad peak indicates a heterogeneous population as seen on Figure 1.19C. This can be generalized to N_p populations of spin packets in a voxel each being characterised by a $mv - \Gamma$ distribution $P_{\kappa_j, \sum_j}(\mathbf{D})$:

$$P(\mathbf{D}) = \sum_{j=1}^{N_p} f_j P_{\kappa_j, \sum_j}(\mathbf{D}),$$

with $f_j \in [0, 1]$ the occupancy fraction of each population and their sum is equal to one.

As said before, DIAMOND is a generalized way to express 3D diffusion and, with a few manipulations of the direct output, new metrics such as the FA, MD and RD can also be extracted. To differentiate them from the direct DTI metrics, they will be called cFA, cMD, cAD, cRD in the rest of this report. But it also provides an overall measure of heterogeneity and takes into account the orientations of fascicles. However, to do so, the number of tissue compartments in each voxel must be defined [32].

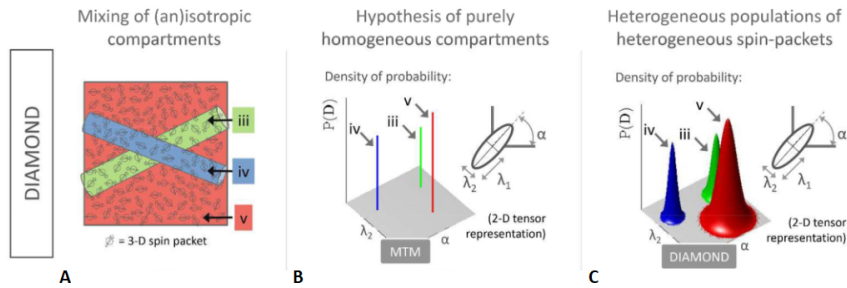


Figure 1.19: DIAMOND model: **A** Several compartments are shown (an isotropic in red and two anisotropic in blue and green); **B** delta functions considering purely homogeneous compartments with no exchange and **C** probability density function when taking into account heterogeneity of diffusion [32].

1.4.3 Microstructure fingerprinting

Microstructure Fingerprinting (MF) is, like NODDI and DIAMOND, a multi-compartmental microstructural model. It is based on a dictionary created through

several Monte Carlo simulations of DW-MRI signals (or also called fingerprints). The purpose is to find the right parameters to describe the microstructure of each voxel. The latter are considered to be composed of several compartments, each characterising the different biological structures found within. To take into account these different compartments, the principle of superposition is used: the signal of several fascicles, of different orientations, intersecting in a voxel is equal to the sum of the signals of each fascicle considered individually [33, 34].

The dictionary mentioned above contains the information of the different parameters of the model (such as the radius of the cylinders representing the axons, the orientations, their density,...) used to represent all the different combinations of microstructural tissues that can be found in a voxel. Then, an algorithm is used to find the best combination that best describes each voxel and thus best represents the information contained in the DW-MRI signal [33, 34].

2 ElikoPy pipeline

The ElikoPy pipeline [35] has been designed in order to face the various disadvantages that come with DW-MRI such as recurring low SNR and artifacts. The signal acquisition is known to induce distortions and slice-wise signal dropouts that have to be corrected to ensure the reproducibility of neuroimaging studies and the coherence of the resulting metrics in order to guarantee a correct interpretation of the results. ElikoPy is thus a processing pipeline developed to correct the majority of image quality problems and inform the user about the quality of the processed data. Its particularity is its ability to deal with large-scale population studies [36].

The implementation of this processing tool is mainly based on several existing Python packages such as DiPy [37], Dmipy [38] and MF [33]. It can also support different types of input formats: Brain Imaging Data Structure (BIDS), classical Digital Imaging and Communications in Medicine (DICOM)² and Neuroimaging Informatics Technology Initiative (NIfTI)³. The process illustrated in Figure 2.1 starts with a data check in order to verify that the image dimensions match the dimensions of the b-value and b-vector files along the acquisitions parameters and index files. In the case of a successful check, a specific folder is generated for each subject and the preprocessing is launched in order to enhance raw images and get rid of the possible artefacts. The creators of this pipeline have shown that there is a real interest in preprocessing, especially for more advanced diffusion models that can be used later. Indeed, their sensitivity to small variations is considerably increased and thus allows for better discrimination of fiber populations within each voxel. Preprocessing tends to make the data more uniform across subjects and to attenuate non-biological differences [36].

Regarding this preprocessing, several steps are successively applied. First, a reslicing is performed in order to deal with the detrimental effect of the automatic interpolation (done by the MRI scanner to enhance image quality) and ensure isotropic voxels. However, this reslicing step brings some drawbacks: there is longer

²DICOM is the international standard to transmit, store, retrieve, print, process, and display medical imaging information [39]

³NIfTI is a type of file format for neuroimaging [40]

computation time or reduced resolution even if the SNR increases for higher voxel volumes. After that, voxels that are not located in the brain area are discarded thanks to the application of a brain mask: the brain is extracted from the skull and other surrounding tissues to allow the following steps of the pipeline to use brain tissue only and thus reduce computation time. A further correction is made by applying a denoising technique, the principal component analysis of Marchenko-Pastur, in order to limit the effect of noise found in the images. This method is quite robust as it does not blur the image or create any artifact. This step should be performed first on the data. Indeed, performing a step of interpolation before would render noise more correlated and therefore lead to the failure of this method since its aim is to reduce the uncorrelated noise [36].

Then, this pipeline is also able to correct Gibbs ringing artifacts. Those artefacts are characterised by series of lines in the diffusion-weighted image [41]. However, this correction has not been applied in this work because if the data is not affected by such an artefact, which is the case for the data considered in the present work, removing it anyway would deteriorate the images instead of improving them. Two other corrections are made by ElikoPy: motion and Eddy Current distortions. They are causing displacements and deformations of the brain but can be jointly corrected. The methods used are coming from FSL [42], FSL Topup [43] and FSL Eddy [44]. First, an estimation of the distortion field is done by Topup and then used by Eddy to correct the distortions in the image. The motion artefacts are corrected between adjacent volumes and also adjacent slices [36].

As explained in section 1.1.1, magnetic fields present some inhomogeneities coming from the scanner itself. The artefacts caused by those imperfections are called bias field and are corrected by applying N4 Bias Field Correction algorithm in ElikoPy. However, as for Gibbs ringing artefact, making the correction when it is unnecessary has detrimental effects and decreases the quality of the data [36].

Next, a WM mask is applied to extract the regions of interest for some specific analysis of the images. It is also helpful to speed up the computation of the different microstructural features. Those features can be analysed via four available algorithms: DTI, MF, NODDI and DIAMOND. All the elements calculated by these methods and used in the rest of this work, will be described in the methods section (section 4). Finally, it is possible to obtain a PDF report for each patient, containing all the information resulting from the performed steps of preprocessing [36]. It is also useful to mention that ElikoPY has other parameters and preprocessing steps available but that they will not be described further here, as they were not performed in this case.

Finally, in the prospect of studying volume changes, ElikoPy is able to segment the brain in three parts: the WM, the GM and the CSF. This information is contained in a file with only three values, either 1, 2 or 3, each corresponding to a specific tissue class. Thus, if a pixel is assigned to 1, it means that it belongs to the CSF (and respectively 2 and 3 the GM and the WM).

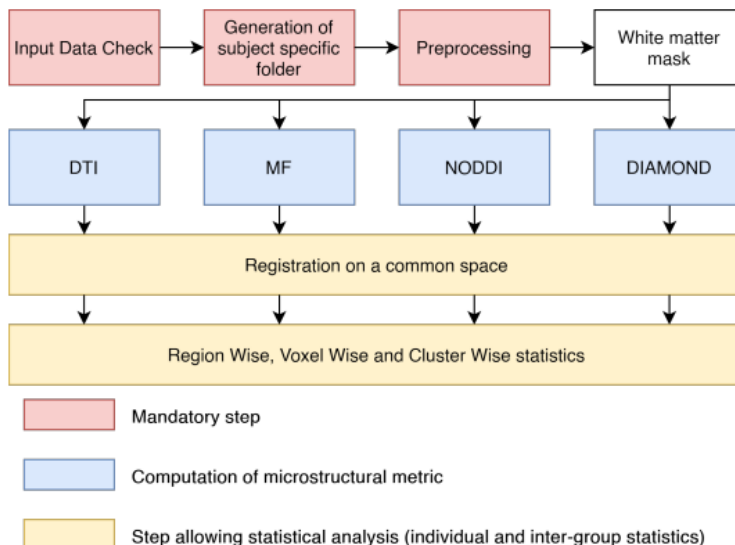


Figure 2.1: Overview of the main processing steps in the ElikoPy pipeline [36].

3 Alcohol Use Disorder

3.1 Definition of AUD

Alcohol Use Disorder (AUD) is a medical condition characterized by an impaired ability to stop or control alcohol consumption [1]. This pathology is a major concern in many health systems because of its prevalence among the population and the variety of consequences that it might cause in the human body. Indeed, it has been reported that worldwide, 7% of drinking adults suffer from AUD which is equivalent to 1.4% of the population, with a prevalence for people aged between 25 and 34 years old. The disorder is responsible for a large amount of premature deceases and can therefore be accountable for 6% of the global death rate [2, 45].

However, those deaths are not uniformly spread around the globe and Figure 3.1 perfectly illustrates this phenomenon. For that reason, the priority of research on AUD, its causes, consequences and potential treatments varies from country to country. We can first note that the alcohol consumption is globally high for Europe while it is particularly low across North Africa and the Middle East (see Figure 3.1A). Also, the prevalence of AUD in Russia is worrying in comparison to other countries in the world (see Figure 3.1B).

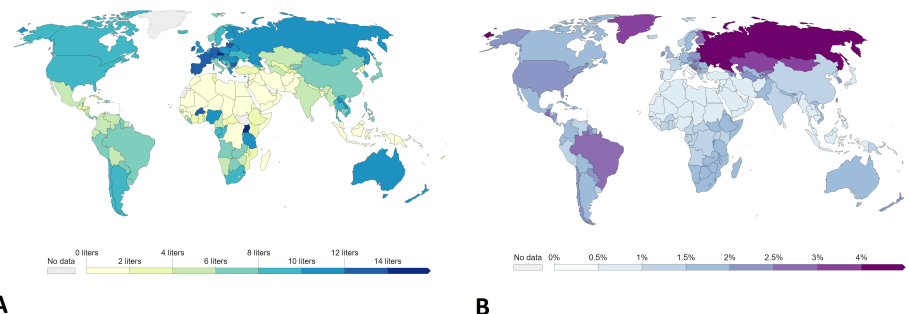


Figure 3.1: Distribution of AUD in the world: **A** alcohol consumption per person in liters of pure alcohol, World, 2018 and **B** share of population with AUD, World, 2017. Adapted from [45].

One way to diagnose a patient with AUD pathology, is to verify if its alcohol consumption is associated with two or more of the typical symptoms of AUD during the past 12 months⁴ [45, 46]:

- Tolerance such that increased doses are required in order to achieve effects originally produced by lower doses;
- Physiological withdrawal state when alcohol use has ceased or been reduced;
- Difficulties controlling drinking in terms of its onset, termination or levels of use;
- Neglect of social, occupational or recreational activities;
- Time spent drinking or recovering from effects of alcohol;
- Drinking despite physical/psychological problems;
- Craving or urge to use alcohol;
- Alcohol consumed in larger amounts or over longer periods than was intended;
- Failure to fulfill major role obligations at work, school or home;

⁴According to the Diagnostic and Statistical Manual for Mental Disorders, 5th edition (DSM-5)

- Recurrent alcohol use in hazardous situations;
- Drinking despite social/interpersonal problems.

The different causes for AUD can be classified in different categories. First, **behavioral risk factors**, linked to the drinking history, include the age of first alcohol use, amount of alcohol consumed, and number of years of heavy drinking. Second, **environmental factors**, such as early life stressors (including physical or sexual abuse) increase the risk for AUD later in life. Third, a **psychological aspect** is also influencing the development of the disease, triggered by high anxiety traits [47].

Moreover, some studies have identified a big role of the alcohol metabolism genes, particularly those for alcohol dehydrogenase (ADH) and aldehyde dehydrogenase (ALDH), in terms of **genetic risks** for AUD. This is the case of Frank et al. [48] who studied the specific gene cluster ADH1 composed of the three following genes: ADH1A, ADH1B and ADH1C. They identified inside this gene cluster a specific nucleotide prone to single-nucleotide polymorphism and correlated to alcohol dependence. In other words, at this specific position in the genome, the nucleotide is prone to a variation in a minority of individuals and this variation appears to be significantly related to the development of the AUD condition.

3.2 Impact of DNA on alcoholism

Despite the incomplete understanding of AUD and its underlying mechanisms, there is substantial evidence of the influence of genetics in the pathology. A majority of the previously cited factors in section 3.1 are influenced by genetics. Indeed, 50 to 60% of the risk for developing AUD are due to genetics, while the remaining percents may be due to either environmental factors, or gene-environment interactions (see *Epigenetics* explanation in the next paragraph and Figure 3.2). Those numbers have been proven by comparing prevalence of alcohol dependence in different situations. The impact of the environment solely could be isolated by comparing children educated in the exact same environment but among which one of them has been adopted (no genetic relationship). Moreover, by comparing siblings who grew up in the same environment to homozygotic twins (100% matching DeoxyriboNucleic Acid (DNA)) in similar conditions, a measure could also be retrieved. We thus know that predispositions to alcoholism play a major role that can not be ignored [47, 1].

Additionally, some researchers have identified mechanisms resulting in heritable changes in gene expression due to alcohol-induced epigenetic mechanisms via modification of histones or DNA methylation. Epigenetics is the way the genes functioning (activity and/or expression) can be affected by someone's behavior and environment, in a reversible way without DNA alteration as detailed in Figure 3.2 [49, 50].

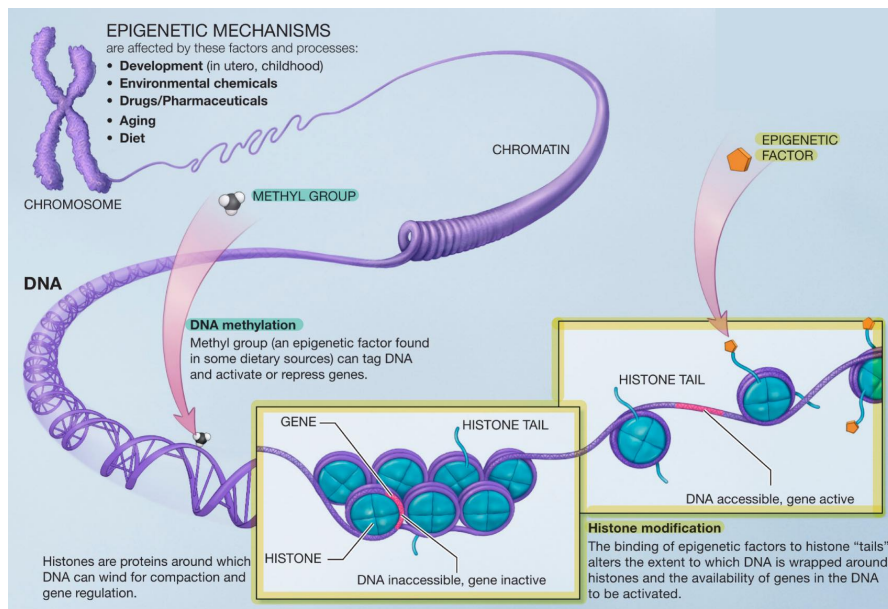


Figure 3.2: Epigenetic mechanisms. Adapted from [51].

This is either expressed by the direct methylation of DNA or by the chemical modification of histones. Firstly, the methylation of DNA works by adding a chemical group to DNA, preventing the decoding of DNA sequence by proteins on this specific site. Secondly, the histone proteins, around which the DNA is wrapped, are controlling this spatial configuration around themselves with their chemical composition. By changing this composition, the DNA can be wrapped (i.e. unread) or unwrapped (i.e. read) because wrapped DNA segments cannot be accessed by the decoding proteins [49, 50].

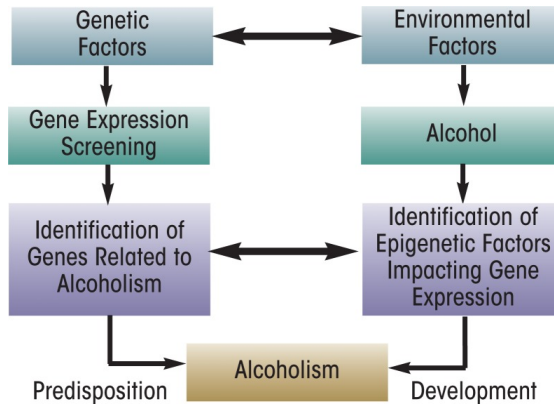


Figure 3.3: Hypothetical model for the interactions of genetic and environmental factors in the predisposition to and development of alcoholism [49].

Accordingly, those epigenetic factors, appearing as a consequence of alcohol consumption, hypothetically contribute to the development of AUD. Those factors are added to the conventional genetic factors, directly related to everyone's DNA sequence that highly influences the predisposition to AUD, as clearly stated in Figure 3.3 [49, 50].

3.3 Biological impact of AUD

There is an undeniable effect of alcohol consumption on the microstructure of the brain, and this for any consumer. Up to date, several studies have been conducted on animals (mainly rats) and humans in order to discover the microstructural abnormalities of excessive alcohol consumption.

In general, microstructural changes on diffusion images are identified according to the metrics introduced in section 1.2.2. The scientific literature shows a wide variety of effects of chronic alcohol consumption with sometimes some contradictory results. Some regions also seem to be more impacted by alcohol consumption than others [52]. A short neuroanatomical description is therefore useful in order to understand this section.

3.3.1 Brain Anatomy

First, the nervous system consists of a central part, Central Nervous System (CNS), and a peripheral one, the Peripheral Nervous System (PNS). Both systems allow the flow of information in the form of action potential in our body. This information can either originate from the peripheral tissue and flow to the brain in order to give feedback to the brain about some sensations; it is then called afferent. Alternatively, a similar flow but in the reverse way for an efferent flow, then qualified as motor information, in order for the body to potentially respond to afferent information. The CNS is composed of two elements: the brain that generates information flow and the spinal cord that conducts it further to the PNS. The brain is composed of three different components: WM (consisting of axons and oligodendrocytes), GM (made of neurons and unmyelinated fibers) and CSF to protect the brain. The CNS can as well be split in 4 different areas: the cerebrum as the main component, diencephalon, cerebellum, and brainstem [53].

The cerebrum

The cerebrum is made of two hemispheres (left and right) and its outer layer, the cerebral cortex, is commonly separated into five lobes shown in Figure 3.4: frontal, parietal, temporal, occipital and insular lobes [53].

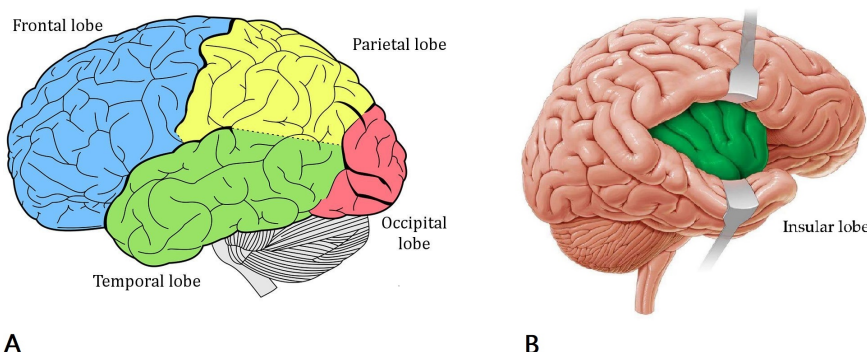


Figure 3.4: Brain lobes: **A** frontal, parietal, occipital, temporal ([54]) and **B** insular ([55]).

Those lobes usually carry specific functions. First, the frontal lobe plays a role in terms of impulse control, attention, imagination, speech and executive function. This executive function is carried by a sub-part of the frontal lobe: the prefrontal

cortex. The latter is also involved in language performances and emotional information treatment. For those reasons, frontal lobe damages can for instance be responsible for impaired judgement, difficulty controlling emotions, impulsive or risky behavior or troubles with communication [56, 52, 57].

Second, the parietal lobe ensures the integration of various sensory stimuli such as proprioceptive and mechanoceptive information and also takes part in the language processing [58].

Third, the temporal lobe is involved in visual memory processes and is therefore subject to memory loss in case of local damage [56, 52]. It is also made of Wernicke's and Broca's area, respectively responsible for understanding/processing and producing speech. Consequently, a dysfunctioning temporal area can also be responsible for disorder of speech, impaired memory skills and changes in self-image and self-perception [59].

Fourth, the occipital area mainly concerns vision. It is responsible for visual perception and interpretation. Finally, the insula gathers a lot of information and sensation such as pain and taste [58].

Subcortical structures

Deeper in the brain, are some subcortical structures. First, the diencephalon comprises the thalamus, epithalamus, subthalamus and hypothalamus (see Figure 3.5). The hypothalamus has hormonal implications both in terms of production and regulation [53]. It is therefore responsible for the relationship between the nervous and the endocrine system, itself regulating a myriad of sub-systems such as body homeostasis, stress or sleep [61]. The thalamus contributes to many brain processes: it is mainly associated with changes in mood, but also plays a role in memory, cognition and perception. Moreover, it relays some motor and sensory signals to the cerebral mantle [52, 62].

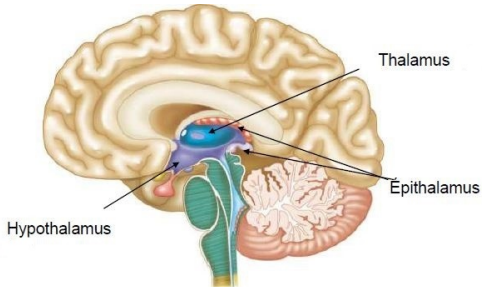


Figure 3.5: Hypothalamus, Thalamus, Epithalamus [60].

Then, the limbic system also has different substructures: the hippocampal formation, fornix, nucleus accumbens, amygdala, and others represented in Figure 3.6. It is mainly involved in memory, olfaction, body homeostasis, regulation of sensorial/visceral activity and emotions. Furthermore, it has a role to play in the production of appropriate responses to stimuli with social and emotional salience [52, 53].

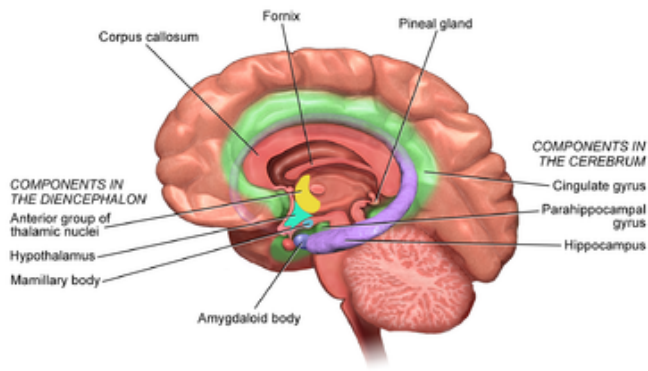


Figure 3.6: Anatomical components of the limbic system [63].

Corpus Callosum

Another key element of the brain's WM is the Corpus Callosum (CC). This is a thick nerve tract interconnecting different cortical regions of bilateral brain hemispheres and enabling communication between them. It is anatomically divided in four parts: the rostrum, the genu, the trunk/body and the splenium shown in Figure 3.7A. Those zones can be even more precisely separated. The example of one possible division is shown in Figure 3.7C [53, 64]. This additional division allows us to mention the isthmus, as a segment between the body and the splenium of the CC, connecting the bilateral superior temporal and the posterior areas of the brain. The first is engaged in auditory processing while the second plays a role in cognitive functions such as attention, working memory and learning [65].

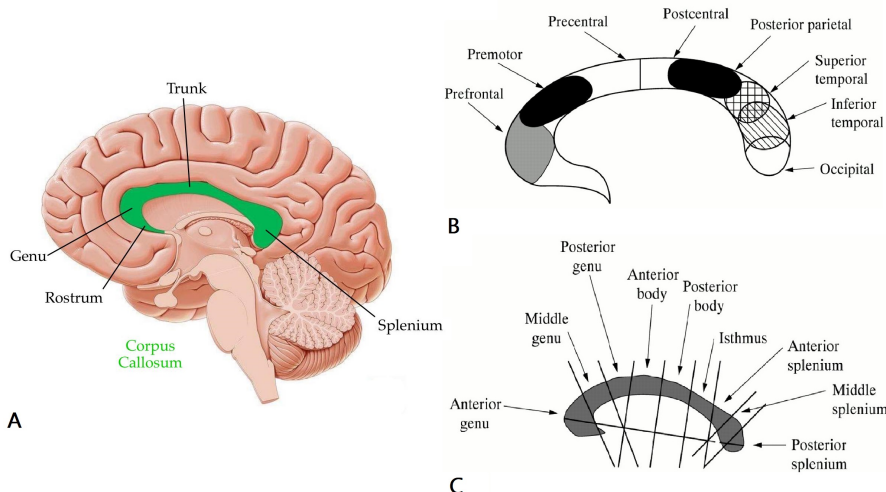


Figure 3.7: **A** Anatomical division of the CC. Adapted from [66] ; **B** Division of the Corpus callosum and **C** corresponding lobes involved [57].

Cerebellum

Finally, the cerebellum lies between the cerebrum and the medulla of the brain stem as shown in Figure 3.8A. It plays an important role in the regulation of motor functions i.e. voluntary muscle contraction and equilibrium [53, 67]. This motor regulation is partly made via the cerebellothalamic network. Indeed, as stated earlier, the thalamus relays motor information [52]. The cerebellum is composed of WM structures such as the cortico-ponto cerebellar pathway and the cerebellar peduncles. Then, the corpus of the cerebellum is divided into several

lobes composed of both white and gray matter. The lobes are made of an outer layer composed of GM and an inner layer made of WM called *arbor vitae* [68].

Furthermore, as introduced earlier, the CSF can be found deep in the brain, inside interconnected cavities that are called ventricles and acts as a protector. One can find 4 ventricles, all represented in Figure 3.8B [53].

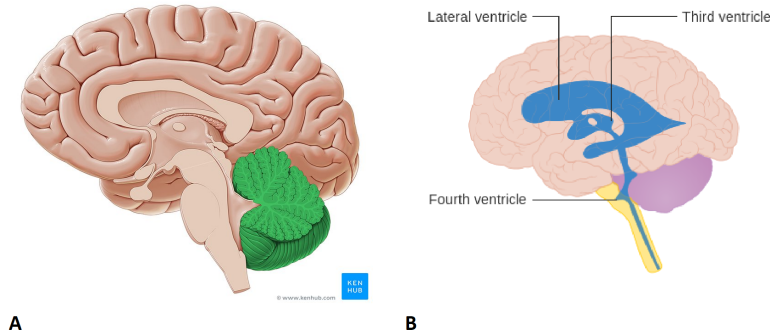


Figure 3.8: **A** cerebellum and **B** ventricles.

3.3.2 Microstructural alterations caused by alcohol

After this anatomical introduction, the focus can now be put on the anatomical changes involving those brain structures as a consequence of alcohol intake. In this respect, the outcomes of some determining studies will be exposed, concerning different results obtained via MRI.

Fractional anisotropy (FA) alterations

First of all, De Santis et al. [5] performed an experiment exploring microstructural changes in AUD patients' WM in comparison to healthy controls. They underlined the fact that the FA seems to be a good indicator of alcohol consumption as heavy drinkers show overall lower FA values in the WM and that this effect is positively correlated with the alcohol problem severity. Monnig et al.[69] and Pfefferbaum et al. [25] also supported this statement. On the contrary, Chumain et al. [70] concluded that alcohol mainly induces an increased FA in most WM tracts of the brain except for the ones located in the cerebellum and the right insula. This shows how important it is to explore as many sources as possible and to conduct new experiments because the literature shows a wide variety of results [5, 69, 25, 70].

In fact, De Santis [5] underlined particularly noticeable FA values in the CC and the fornix (see Figure 3.6), in comparison to control subjects [5]. Other studies like the one of Pfefferbaum et al. [71, 25], Monnig et al. [69], Zou et al. [72] and Liu et al. [64] also supported these observations about the CC. Another study of Monnig et al.[56] also confirmed the observations of De Santis about a FA decrease located in the fornix [5, 71, 25, 72, 69, 64, 56].

On top of that, Liu et al. [64] performed a more local analysis of this effect on the CC and identified a specific FA diminution in the segment interconnecting the bilateral orbitofrontal cortices, located in the genu of the CC (see Figure 3.7A). They also mentioned that no difference was noticed between controls and AUD groups in the segment of the CC corresponding to the bilateral motor cortices,

located in the body part of the CC (see Figure 3.7A).

Similarly, Pfefferbaum et al. [71], Rosenbloom et al.[73] and Alhassoon et al. [74] brought the callosal genu region to the fore by showing bigger FA abnormalities in comparison to the splenium. By contrast, Wang et al. [65] also identified a decreasing FA behavior in the CC but this time in the isthmus region, localized more posteriorly and Alhassoon et al. [74] concluded the same for the CC's body [64, 71, 73, 74, 65].

Other brain regions also have been highlighted for their lower FA values in comparison to control subjects. To cite some of them: the thalamus [56], the cerebellum [70], the insula [70], the hippocampus [72], the external capsule [72] and the cingulum [72].

Diffusivity alterations

According to those same studies, AUD patients show other variations for diffusivity measures. Some of them state that the MD tends to increase to values higher than controls as a consequence of alcohol consumption in the CC [71, 5, 65]. In particular, some studies highlighted the local changes on different callosal regions. Wang et al. [65] identified the isthmus region as sensitive to MD changes whereas Pfefferbaum et al. [71] stated that the genu is more prone to high MD values than the splenium of the CC (see Figure 3.7B). Alhassoon et al. [74] had similar observations for the RD in the genu and the body of the CC. On top of that, the previously mentioned studies stated that AUD brings similar consequences regarding AD and RD: both are higher in the CC in comparison to controls [5, 65, 71, 74].

In a more global approach, Chumain et al. [70] contradict the results of others and claimed that diffusion tends to be lower in most WM tracts for AUD patients whereas De Santis et al. [5] observed an overall increased MD and RD and a decreased AD in WM tracts [5, 70].

To sum up, there is a myriad of studies focusing on the effect of alcohol on the human brain and DTI is the most widely used model to extract several properties. The interest of covering the literature available is to first, keep in mind that results can sometimes be biased and that similar studies can have contradictory results. Second, by gathering the results of many studies, one can clearly see that some metric tendencies tend to appear in a bigger amount of studies, suggesting that the results are more reliable. For this reason, Table 3.1 summarizes the different conclusions of the articles explored here above in order to illustrate the observations on which the literature seems to agree in general and the discrepancies that sometimes also appear.

Another detail to keep in mind is the fact that alcohol has immediate, short term and long term effects on the brain microstructure. Rolland et al. [75] conducted a study to differentiate the direct effects of alcohol (a few hours post intake) from the longer-term impacts. They were able to underline significant changes in the induced modifications. It is therefore important to keep this study in mind as an indicator of relevance: if long term effect of alcohol is studied, AUD patient should at least experience a small abstinence period in order to avoid immediate effects to be considered as relevant for long term alterations.

Table 3.1: Summary of the observations published by different articles

IMPACTS OF ALCOHOL								
	FA		MD		AD		RD	
Area	+	-	+	-	+	-	+	-
Overall WM	[70]	[5],[69], [25]		[5]	[70]		[5]	[5]
CC		[5], [69], [64], [71], [72]		[5],[65], [71]		[5],[65]		[5],[65]
Genu (CC)		[71],[74], [73],[64]		[71]				[74]
Body (CC)		[74]						[74]
Isthmus (CC)		[65]		[65]				
Fornix		[5],[56]						
Thalamus		[56]						
Cerebellum		[70]						
Insula		[70]						
Hippocampus		[72]						
Ext.capsule		[72]						
Cingulum		[72]						

3.4 Microstructural effects of abstinence

There are many stages of withdrawal that have to be distinguished when analysing results of different studies. Indeed, early withdrawal changes can differ from long-term abstinence effects. It is therefore crucial to take the period of sobriety into account when exposing results. Those results are relatively different across the literature but still contribute to the hope of promising recovery for abstinent patients. Usually, the studies either focus on DTI metrics such as the ones developed in the previous sections, or on volumetric changes by comparing the relative WM,GM and CSF volumes through the brain or the volume of well-known brain regions.

3.4.1 DTI metric changes

Regarding short term effects, a study of De Santis et al. [5] showed that in the **first weeks** of abstinence, a group of AUD patients was characterized by changes such as global FA decrease and elevated RD. Those results suggest that the microstructural alterations caused by alcohol do not start to revert to control values immediately after discontinuing alcohol consumption [5].

Similarly, Zou et al. [72] focused on the changes **between 1 week and 1 month** without alcohol consumption. At the beginning of the abstinence, they have put forward three zones, characterized by lower FA values (in comparison to control subjects), that recovered to normal values after one month: the hippocampus, the external capsule and the cingulum. Those regions however still showed significantly low FA values after one week of abstinence, meaning that the changes mainly appeared progressively in this 4 week period [72].

On a longer timescale, Zorlu et al. [76] conducted a study focusing on abnormal WM integrity in long-term (**> 6 months**) abstinent alcohol dependent patients by comparing them to healthy control subjects. In terms of DTI measures, they found significantly higher RD and AD values for the long-term abstinent alcohol dependent group in frontal, temporal and parietal WM areas compared with the control group and those results persisted for an even longer period. They mentioned that those AD/RD abnormalities were still observed after **27.8 months** in average. Conversely, FA values did not differ between groups meaning that detoxified alcoholics came back to FA values comparable to those of controls in the WM tracts. They were thus able to state that some myelin abnormalities seem to be partially persistent even for long term abstinent patients while others are fully reversible [76].

Pfefferbaum et al. [25] also studied the evolution of DTI metrics during a long term abstinence period (median period: **90 weeks** i.e. a bit less than 2 years). Over time, the overall WM FA increased progressively, whereas the FA of control subjects tends to decrease over time as a consequence of aging (within a 1- to 8-years interval). This positive FA evolution is therefore even stronger as abstainers still suffer from aging, but proved increasing values heading toward normality. Regarding AD, the latter also tends to increase with age for control subjects in general. But the changes in the case of abstainers suggest, in the same way as the FA changes, a progressive repair [25].

Monnig et al. [56] reported lower FA values in the parietal and temporal regions for AUD remitted patients, sober for **more than one year** when compared to control subjects. Those observations were extended to other brain areas such as the superior and inferior corona radiata, the splenium of the CC and the posterior thalamic radiation. By contrast to the study of Zorly et al. [76], this suggests that FA values do not come back to a «normal »level even after one abstinence year [56].

3.4.2 Volumetric Changes

By contrast, Zou et al. [77] conducted a progressive volumetric study involving a short term and a long term abstinence analysis. The early abstinence was evaluated for a period **from 1 week to 1 month** and the longer term was focused on the evolution of volumetric changes **between 1 month and 7 months** of abstinence. They also restricted their analysis to six regions of interest: Anterior Cingulate Cortex (ACC), DorsoLateral PreFrontal Cortex (DLPFC), OrbitoFrontal Cortex (OFC), insula, and hippocampus. This study first concluded that the baseline volumes, after 1 week, differed between groups: the ACC, hippocampus and the DLPFC were smaller for the alcoholic group in comparison to a stable control group. However, they found out that between 1 week and 1 month of abstinence, subjects had increased median volumes for all the regions of interest, except for the amygdala. Later on, between 1 and 7 months, they observed a structural recovery translated by a significant volume increase of 3 brain regions (ACC,DLPFC,OFC) but unlike in early abstinence, no further evolution was observed for the other zones. Furthermore, those increased volumes after 7 months of withdrawal in ACC, DLPFC and OFC were equivalent to control group volumes, resulting in a total volumetric recovery. This recovery was thus progressive; after 1 month of abstinence, the respective volumes were already partially recovered and it required

6 more months to achieve a full recovery. The evolution rate was however 4 to 6 times higher in the early abstinence phase.

Another volumetric study conducted by Agartz et al. [78] evaluated changes after **48h, one month and 2.5 months** of abstinence. They reported that the total GM did not significantly change over time along the abstinence period. However, the WM showed extremely promising results. Indeed, the total WM volume increase ranged between 1.9 and 22.4% for absolute volumes and 2.1 and 21.2% for relative volumes. Those results are displayed in Figure 3.9 for which both groups are represented in different colors. One can clearly observe the increasing tendency of WM volume in alcoholic patients during their withdrawal, but the values for AUD patients are still lower than the ones of the healthy group.

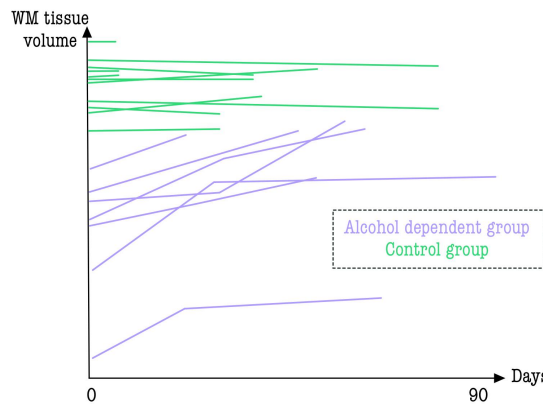


Figure 3.9: Relative intracranial WM tissue volumes in seven alcohol-dependent patients and a reference group of 11 healthy control subjects measured over time (days). Adapted from [78].

Similarly, Shear et al. [79] highlighted this single WM evolution without any significant changes in the GM. Once again, this shows the variety of results available in the literature, as Zou et al. [77] mainly reported GM changes up to **7 months** withdrawal while this study [79] demonstrates changes in brain volume are confined to WM, for a 2.5 months abstinence, and appear to be the greatest in the first weeks of the withdrawal [78].

3.5 Psychological influence of alcohol and abstinence

3.5.1 Alcohol effect

Alcohol consumption and mental health are extremely closely related. On the one hand, an excessive alcohol consumption has an unavoidable influence on the consumers' mental health and has proven to be a risk factor of severe depression or anxiety. Thus, death can either be a direct or indirect consequence of alcohol dependence, for example through suicide. As a matter of fact, it has been estimated that the relative risk of suicide in an individual with alcohol dependence is around 10 times higher than an individual without [45]. On the other hand, mental health issues can also lead to alcoholism. This is the reason why AUD can be either a cause or a consequence of mental issues [45].

Moreover, as explained in section 3.3, AUD patients exhibit several microstructural changes that can be characterized by the variation of different metrics (FA,

MD, AD,...) measured in the white and GM of the brain. In general, alcohol use has shown damaging alterations of WM integrity, whereas higher WM integrity tends to translate better cognitive functioning. All those changes are also reflected on the behavior of AUD subjects, as brain regions are usually responsible for specific tasks.

As the biological impact of AUD has already been introduced in section 3.3, with a description of local brain areas in which changes are usually observed as a consequence of chronic alcohol consumption, specific behavioral changes can be underlined. First, the memory, cognition and motor capabilities are threatened by damages in multiple zones concerned by AUD. Then, hormonal dysfunction can also be a consequence leading to deregulated body homeostasis and increased stress level. Finally, mood changes can be noted as a downside of alcohol consumption, being a consequence of damages at the level of the thalamus.

3.5.2 Abstinence effect

In the framework of a long abstinence period of **4 years**, Rosenbloom et al. [80] successfully showed improvement in overall memory, non-verbal short-term memory and psychomotor speed for remitted patients. What is also interesting in this study is that the same tests were performed already after **one month and one year** of withdrawal, and it turns out that no significant cognitive recovery was observed after two years and that no real improvement in terms of short-time memory were observed between early abstinence (1-2 months) and two years abstinence. This is the proof that AUD recovery is a long process with progressive steps. Some of the cognitive and physical capacities can be retrieved in the first weeks of abstinence while others are the result of years of efforts to fight the pathology [80].

This is in line with the study of Agartz et al. [78] which thanks to behavioral and microstructural observations during abstinence, observed some improvements in short-term memory, abstract reasoning, spatial ability and visuo-motor capacities during the first **2 weeks** of abstinence.

On the contrary, Monnig et al. [56] established the neuropsychological profile of early abstinent subjects and they mainly reported symptoms like confusion, poorer memory, and impaired attention, and mentioned that those effects tend to resolve with **several months** of abstinence. They also related those changes to the abnormal frontal and temporal diffusivity found in DTI analysis [56].

Part II

Brain microstructure analysis

4 Methods

4.1 Data collection

The data were collected in the framework of the PhD of Mélissa Salavrakos. AUD patients were first recruited according to a criteria of highly frequent alcohol consumption and were included in a 18 days withdrawal program in *Cliniques universitaires Saint-Luc* located in Brussels (Belgium). The first exclusion criteria is the presence of a severe comorbidity such as a severe psychiatric comorbidity (bipolar disorder, schizophrenia), severe hepatic comorbidity (viral hepatitis, autoimmune disease), chronic inflammatory disease (lupus, vasculitis) and regular or significant intake of anti-inflammatory drugs. The second exclusion criteria is a known contraindication to magnetic resonance imaging due to the presence of a pacemaker, clip or ventriculo-peritoneal drain in the patient's body. As stated earlier, this study concerns an 18 days abstinence program. However, some subjects did not come back at the end of this period, those subjects were thus excluded from the sample.

The set of patients included in this study underwent an MRI scan on the first day of admission (Day 1), referenced as Time 1 (T1) for the rest of this paper. A second scan is performed 18 days later (Day 18) and is therefore called Time 2 (T2). The goal of this program is to study the short-term effects of abstinence on the brain microstructure and to relate them with other behavioral information and other variations taking place in the rest of body such as inflammatory data or blood samples. The set of patients treated for this master's thesis is composed of 46 patients who all followed the same precise protocol. The MRI device used is the *3T SignaTM Premier, GE Healthcare* with an EP-SE sequence. The acquisition was made with an imaging frequency of 127.77 Hz, a slice thickness of 2 mm, a TR of 4.837 s and TE not identical for each patient but always around 79/80 ms. A typical .json file containing all the scan parameters is available in appendix A.

For each patient, a set of 3x2 data files acquired respectively at T1 and T2 were provided:

- 2 anatomic scans: they are T1-weighted contrasted scans (156 x 256 x 256) as shown in Figure 4.1;

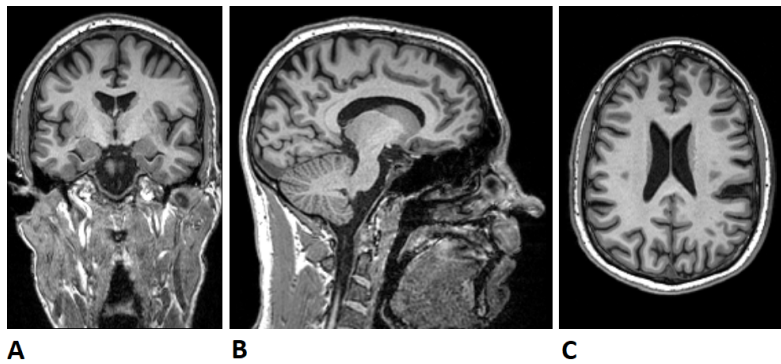


Figure 4.1: Slice (**A** frontal, **B** sagittal and **C** axial) of the anatomic scan of a patient.

- 2 diffusion scans: files composed of 167 volumes. 7 were acquired with a null b-value and 160 were acquired with different b-values (1000, 2000, 3000 and 5000 s/mm^2), as displayed in Figure 4.2. Each volume has a shape (110 x 110 x 68);
- 2 diffusion correction scans: these files were acquired in the same way as the diffusion scans but were manually stopped before their completion to only obtain the first volume. Those scans allow a better preprocessing by ElikoPy.

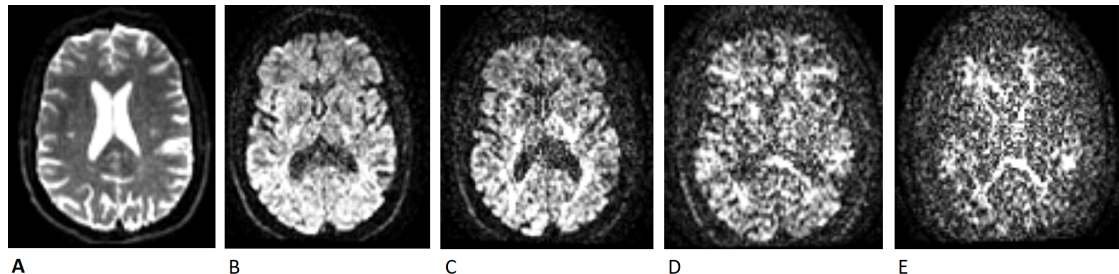


Figure 4.2: Slice of a volume with a b-value equal to **A** 0, **B** 1000, **C** 2000, **D** 3000 and **E** 5000 [s/mm^2] of diffusion scan of a patient.

Altogether, data from 46 patients were received. However, some had to be discarded because one of the two acquisition times (T1 or T2) was missing. The decision was made to exclude such patients because this work focuses on microstructural changes between the two MRI scans. Some other patients also had to be discarded because their anatomical scans were missing. Indeed, this data is necessary to perform the preprocessing with ElikoPy correctly. Finally, some of them also had to be excluded because their files were damaged. This will be developed in more details in section 4.2. As a result, out of the 46 patients, only 35 had a complete usable set of data's on which the study could be performed.

In addition to the medical data issued from the MRI, behavioral information was gathered by Mrs Salavrakos for each patient through the following series of questionnaires:

- Beck Depression Inventory (BDI): psychometric tests to determine the degree of depression and the dynamics of its evolution [81]. The questionnaire is made of 21 items (questions) to which a score between 0 and 3 is assigned.

The total score thus ranges between 0 and 63 (3*21): the higher the score, the more severe the depression state;

- State-Trait Anxiety Inventory (STAI): instrument quantifying adult anxiety. This particular instrument is used to simplify the separation between state anxiety and trait anxiety, feelings of anxiety and depression through a 20 questions test [82]. A score between 1 and 4 is assigned for each question. The total outcome thus ranges between 20 and 80 (4*20): the higher the score, the higher the anxiety level;
- Obsessive Compulsive Drinking Scale (OCDS): rating instrument that provides a measure of some cognitive aspects of alcohol craving. This score results from two intermediate scores aiming to differentiate the obsessions and the compulsions about drinking;
- Multidimensional Fatigue Inventory (MFI): set of 20 questions, scored between 1 and 7 to assess the fatigue level on different perspectives. The final score varies between 20 and 140 (20*7);

Other tests and questionnaires were also performed but they will not be developed as they are not relevant for this work.

4.2 Data conversion

As mentioned previously, 6 files were created for each patient with the following names: NAME_T1_Anat3D, NAME_T1_DTI, NAME_T1_DTicorr and identically for T2. These files contain DICOM data. The first step was to make the files anonymous. This can be done with the MRIcron software [83]. The latter also allowed DICOMs to be converted to NIFTI. This conversion created 2 files for the anatomic scan, a .json and a .nii.gz, and 4 files for the diffusion files, .bval, .bvec, .json and .nii.gz. On the one hand, the .json gathers the technical information of the scan such as the scan options, the imaging frequency, and all the specific MRI parameters of the sequence. On the other hand, .bval, .bvec files summarise the different bvalues and the corresponding bvectors, whereas the .nii.gz file is the file of interest, composed of all the recorded MRI slices. Finally, a naming convention was also adopted during the conversion: the different patients were renamed « sub# » with a different number each. This choice was made to be consistent with the organisation of the ElikoPy pipeline.

The conversion described in the previous paragraph was successful for all patient files used in this master's thesis. However, to achieve this, a manual conversion of the so called DTIcorr files had to be carried out. Indeed, these files were supposed to contain only one volume but contained several, each composed of 68 DICOM slices. Thus, to make the conversion work, the excess slices had to be manually removed: only the first 68 DICOM files, thus belonging to the first volume, were conserved. This manipulation prevented the creation of the corresponding .bval and .bvec files during conversion that also had to be manually created with the appropriate values: the .bval file contain only one value (0) as the volume was acquired with a b-value of 0 [s/mm^2], and the .bvec file contain a set of 3 values (0, -1 and -0.115951), the coordinates of the corresponding vector.

Regarding the preprocessing of the data, it was entirely performed through the ElikoPy pipeline, as explained in section 2, in order to remove the different artefacts contained in the images.

4.3 Regions of Interest (ROI)

4.3.1 Atlas collection

The goal of this study is to analyse the microstructural changes in the different brain zones due to short-term abstinence. For this, 7 atlases gathering 141 different zones (atlas maps) have been used in this study to cover as many regions as possible. An atlas is composed of several labeled maps representing a specific region of the brain, allowing the data to be analysed and characterised on the basis of the anatomical location [84]. Each voxel is then assigned to a specific area of the brain responsible for specific functions. The detailed list of all atlases used is available in appendix B.

The first atlas used in this study was created by Jörn et al. [85] as a representation of the entire cerebellum. The latter is a probabilistic map, divided into 21 lobules. Hence, each map contained in the atlas is a brain representation giving to each voxel, the probability of being in the concerned zone of interest. Regarding the cerebellum sub-division, the authors decided to group the lobules I to IV into a single area, and then to create separate zones for lobules V, VI, Crus I, Crus II, VIIb, VIIIa, VIIIb, IX, and X. They then divided the cerebellum into a left and a right part. The I-IV lobule was additionally divided into a vermis (central) part. Those delimitations can be observed in Figure 4.3. 6 additional maps are then added to this set to account for the white matter connections of the cerebellum. They are listed under the name Cerebellar in appendix B. Those last 6 maps are publicly available on the NatbrainLab website [86].

Then, another atlas is chosen to cover the GM of the brain. For this, 48 cortical and 21 subcortical structural areas were segmented by the Harvard Center for Morphometric Analysis [87]. Thereafter, 5 maps were selected to represent different lobes of the brain: insula, occipital, parietal, temporal and frontal. They originate from Research Imaging Center and as the previous ones can be downloaded on FSL [87].

Finally, 42 probabilistic tract maps were published by Warrington et al. [88] in the framework of a study providing standardised tractography protocols resulting in the automated extraction of WM tracts in human and non-human primate brains. The resulting files were then made publicly available through FSL [87]. These maps are of great interest in the context of this thesis as the WM evolution will be carefully analysed through this whole abstinence process. However, the thickest WM tract of the human brain is not part of the previously mentioned atlas: the

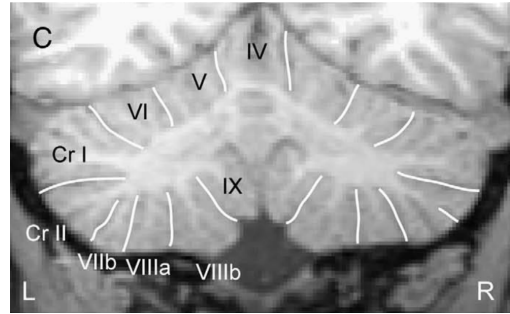


Figure 4.3: Lobules assignment of the cerebellum [85].

corpus callosum.

An additional WM atlas was therefore downloaded from NatbrainLab [86] in order to include the CC in this research. However, this raw probabilistic atlas was created on a diffusion image belonging to a specific space but the location of the CC map in the MNI brain, HCP1065 standard-space, was not completely correct. For this reason, the decision has been made to correct this CC delimitation in two steps. This will be explained in detail in section 4.3.2.

4.3.2 Corpus Callosum modifications

First, as the atlas is probabilistic, the probability of a voxel to be located in the CC progressively fades as one moves away from it. But as the downloaded CC was slightly offset in the original space, very small probabilities were assigned to pixels actually located in the middle of the CC where a probability of 1 would have been expected. This phenomenon is clearly depicted in Figure 4.4 in which the original diffusion image (Figure 4.4A) and the overlay of the CC atlas (Figure 4.4B) are displayed. The three colored arrows show key locations illustrating this atlas limitation. As Figure 4.4A shows, the blue, orange and pink arrows respectively delimit a left, upper and lower border of the anatomical CC but are still located in the zone. However, the atlas was not correctly built: it ranged from high values (red) in the middle of the CC to lower values (green) in the surroundings, but those weak probabilities displayed in green are actually still inside the CC on the upper part and are fully out of the zone on the lower one. And here, the numbers speak for themselves: the blue and orange arrows located at the border of CC correspond to probabilities of 0% to be in the CC according to the probabilistic map. By contrast, the pink arrow located similarly at the border of the actual CC points toward a yellow area translating a probability of 75%.

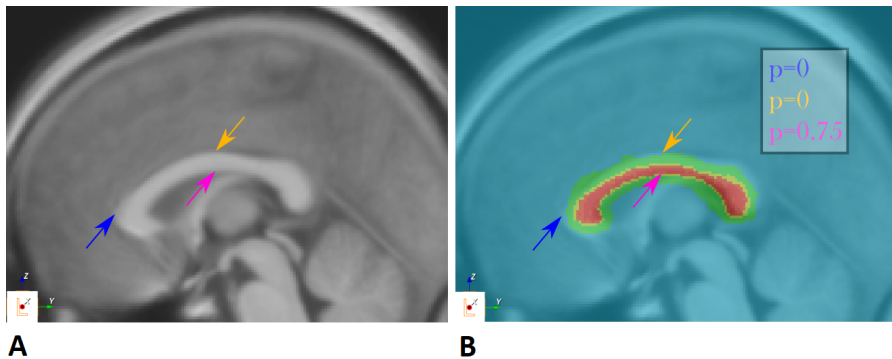


Figure 4.4: Limitation of the initial CC atlas: **A** diffusion image in the original space and **B** overlay with CC atlas.

For this reason, the CC delimitation had to be built according to a very low probability to ensure that the entire CC was taken into account. Thus, the threshold chosen to delimit it was set to 0.14. However, this choice came with undesired consequence: the selected zone was very large thus containing pixels in various other structures such as the CSF located right under the CC.

Hence, a solution had to be found to shrink this excessive atlas in the appropriate way in order to only consider voxels truly located in this ROI. A solution for that is to use FA indications. Indeed, the CC is the most anisotropic region of the brain,

due to its big amount of fibers connecting both hemispheres. Consequently, the voxels inside the CC are represented by very high FA values in comparison to its surrounding regions, and a combination of the available (pre-treated) atlas and an FA map could be wisely built to shrink the area. However, the current CC atlas was registered in an unknown space and no FA map was provided by the website. Thus, a first processing step was necessary to register the atlas in the HCP1065 standard-space for which a high quality FA template was at our disposal [87] (see Figure 4.5).

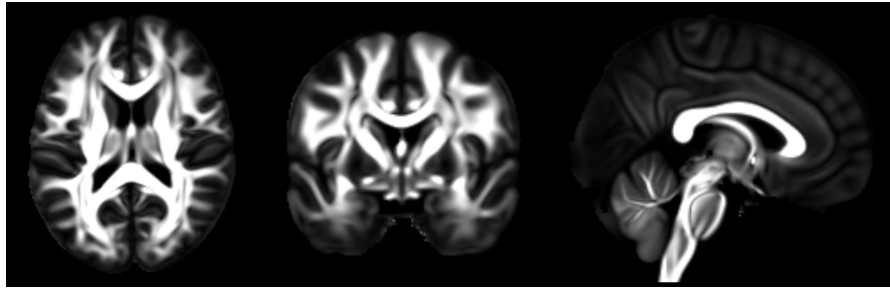


Figure 4.5: HCP1065 standard-space FA map.

As both, the atlas and this FA files were now in the same space, a « FA mask » could be extracted to shrink the atlas as intended. In this respect, a threshold of 0.34 was chosen for FA values. This value was set as a result of observations with MisterI program [89]. In other words, each voxel previously considered as part of the CC (assigned with a probability higher than 0.14), characterized by a FA value lower than 0.34 was excluded from the atlas. The Figure 4.6 illustrates the different steps in the creation of the new CC: the registration step in the HCP1065 standard-space and the use of the mentioned thresholds.

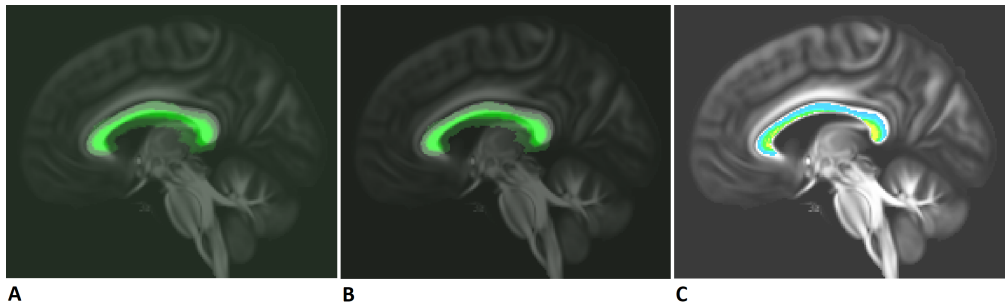


Figure 4.6: **A** CC after registration in the HCP1065 standard-space, superposed on the FA map (high quality template); **B** Result after applying a 0.14 threshold on the probability of the CC; **C** Result after the multiplication by a FA mask keeping the FA values higher than 0.34.

As a result of these steps, the created CC was smaller than the anatomical one and many pixels were missing. This default was not visible on every slice (see Figure 4.6) but some slices showed a high number of missing pixels as shows Figure 4.7A. A decision was therefore made to draw the CC by hand. Using the MRIcron software [83], the previously obtained CC could be improved by manually selecting the missing pixels. The difference between both CC is depicted in Figure 4.7.

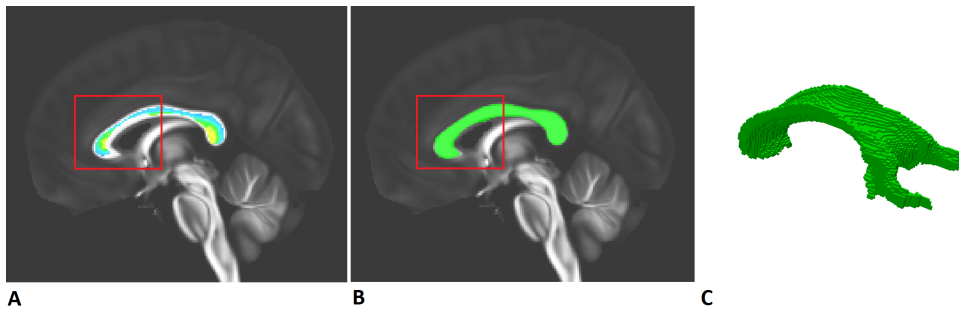


Figure 4.7: **A** CC atlas after applying a threshold and multiplication by a FA mask; **B** hand-drawn CC and **C** its 3D visualisation.

As this manually built atlas was based on a correction of the downloaded one, it was selected to go on for the rest of the analysis of the CC. At this stage, a finely delimited CC was built in the MNI space. Next, a registration of this atlas was made on every single patient in the same way as for the other atlas maps. This registration will be detailed in next section 4.3.4.

Finally, by observing the resulting atlas, it was noticed that a few imperfections resulted from the registration: some isolated voxels appeared out of the CC due to their location in WM tracts close to the CC, while a few pixels located inside the CC were removed. To solve this, two morphological operations from Scikit-image library [34] were successively applied: an opening and a closing (respectively `skimage.morphology.area_opening` and `skimage.morphology.area_closing`). The resulting CC atlas in a patient space can be observed in Figure 4.8C-D. The latter is enhanced and delimits the appropriate zone, in comparison to the original one composed of imperfections (see Figure 4.8A-B).

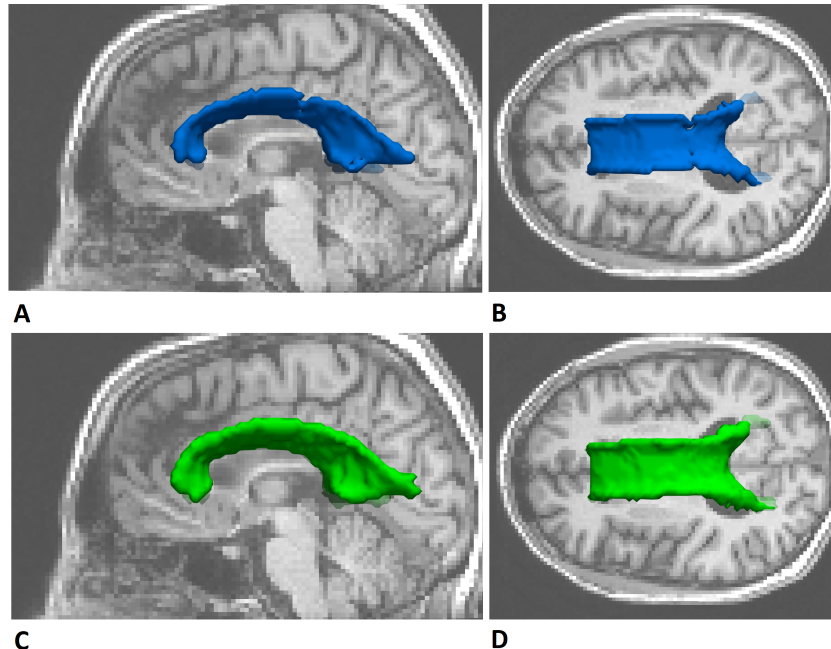


Figure 4.8: Final atlas map of the CC **A-B** after registration in the patient space and **C-D** after the application of morphological operations (opening and closing) superimposed on the anatomical map of a patient.

4.3.3 Corpus callosum division

The CC is a region carrying a lot of interest in the study of AUD and it has already been mentioned in many studies that several tendencies can rise from different parts of the CC. For this reason, the recently created CC atlas was further divided, to proceed to a more local analysis of its different sub-regions. This sub-division was inspired from a paper of Hofer et al. [90] who decided to split the tract into five regions: the genu, the anterior and posterior midbody, the isthmus and the splenium as detailed in Figure 4.9A. According to that, five more maps were added to the set considered in this master's thesis. The CC map, registered on each patient, was therefore divided for each patient using the same method. An overview of this division is depicted in Figure 4.9B and C.

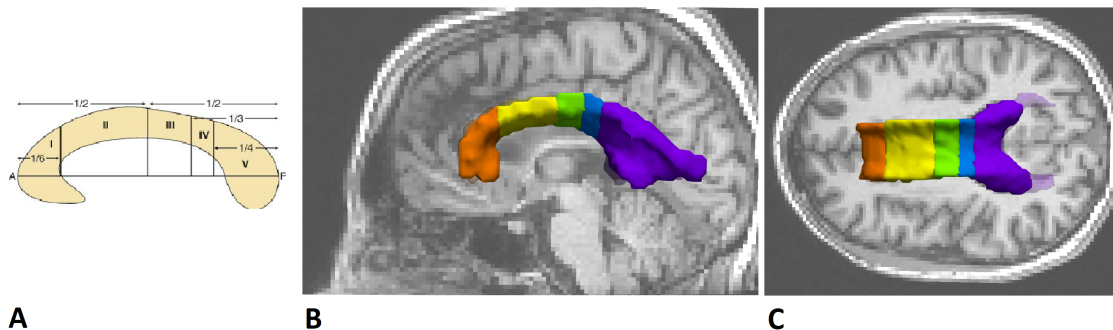


Figure 4.9: **A** Topography of the midsagittal CC [90]; **B** Sagittal and **C** axial slice of the CC map sub-division. All the regions in subfigure **A** correspond to a color in subfigure **B/C**: region I representing the genu is in *orange*; region II in *yellow* and region III in *green* illustrating the anterior and posterior midbody respectively; region IV in *blue* showing the isthmus and region V in *purple* depicting the splenium.

4.3.4 Atlas registration

Once all those standardized atlases are downloaded, it is important to recall that they were registered in the Montreal Neurological Institute (MNI) space and built according to a large set of human brains and then generalized into the common MNI152 coordinate system (corresponding to the *152th nonlinear 6th generation atlas*) using appropriate registration. The MNI152 space was built through a coregistration of 152 normal images to another MNI space, itself coregistered to a well-known atlas: the Talairach atlas. This coregistration is a way to define a standard brain anatomy [91].

As each subject treated in this master's thesis possesses a unique brain, the maps contained in those atlases had to be registered for each one of them in order to delimit correctly each area of the brain on which the analysis was performed. This registration thus resulted in two maps per patient, one for T1 and another one for T2. Indeed, as introduced in section 3.4.2, the brain of AUD patients is prone to volumetric changes in some brain area so the maps might slightly differ between the first and the second scan.

The method used to perform this registration is the combination of two different sub-registrations applied successively: first an affine transformation and then a

diffeomorphic registration. To start with, the affine registration is the combination of a translation and rotation step called rigid transformation, and a scaling step characterizing the affine part. A combination of both steps is illustrated in Figure 4.10A. Thereafter, the second operation is a diffeomorphism registration, which is *an isomorphism of smooth manifolds*. *It is an invertible function that maps one differentiable manifold to another such that both the function and its inverse are differentiable* [92]. Figure 4.10B displays this particular phenomenon.

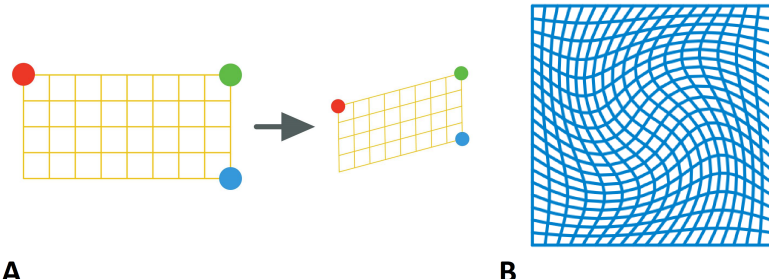


Figure 4.10: Transformations used for the registration **A** affine transformation and **B** diffeomorphism (rectangular grid on a square under a diffeomorphism from the square onto itself) [92].

The registration is based on a DiPy tutorial [93] and is built in the following way. First, a function called `getTransform` takes a static volume (T1 or T2 scan) and a moving volume (here considered as the HCP1065 standard-space FA map) as arguments and returns a transform operation mapping the moving element on the static one. Then, a second function named `applyTransform` simply applies the transformation on the atlas map to create its corrected copy.

To illustrate those manipulations, the transformation process of one WM tract called « Cingulum subsection dorsal right » is detailed for each one of the steps. One can observe in Figure 4.11A, the original atlas map in the MNI space. But as shown in Figure 4.11B, the latter does not fit at all to the FA map of a specific patient of this study. This is the reason why it was registered, in order to target the correct brain area. Figure 4.11C clearly reveals the efficiency of the transformation.

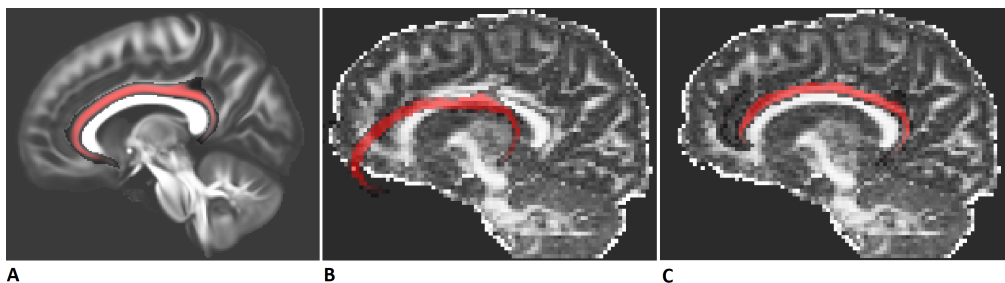


Figure 4.11: Registration process for the Cingulum atlas map. **A** Initial map in MNI space; **B** Initial map in patient space; **C** Registered map in patient's space.

Finally, in order to enhance this zone delimitation represented by each map, a mask was applied on some of them. A mask is a binary map only composed of 0 and 1 elements. It can be applied on any other map by multiplication: pixels located in the mask (in areas covered by *ones*) keep their initial values whereas the others are set to zero. This useful tool to delimit specific zones was used in this

case because we had at our disposal (thanks to the ElikoPy pipeline) two masks for each patient: a brain mask and a WM mask (for T1 and T2) as displayed Figure 4.12.

On the one hand, the brain mask gives the real delimitation of the brain area, and its application on any atlas map avoids to an atlas region to be considered outside of the brain (in the background). On the other hand, the WM mask is a little bit more specific and allows the correction of a lot of errors. This mask delimits all the WM in the brain, and as the latter can be defined by thin segments and small areas, it was of great interest to make sure that a WM tract was not falsely registered. Indeed, a wrong registration could have detrimental consequences on the following analysis if some GM or CSF voxels were considered as part of a WM tract, as the changes in the WM and GM respectively are expected to be different.

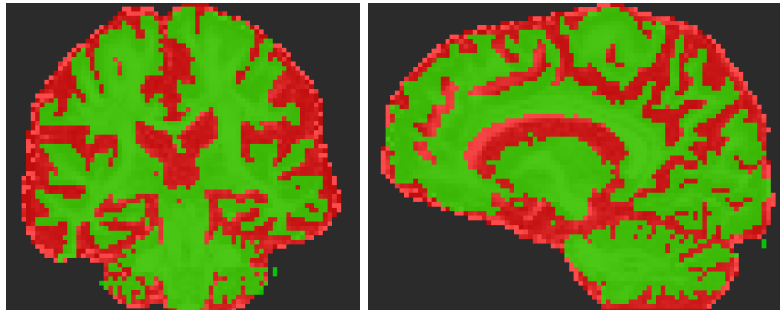


Figure 4.12: Superposition of the brain mask (red) and WM mask (green).

Consequently, two new masks (T1 & T2) were created for each atlas map of each patient considering two criteria. First, as the maps used in this study are probabilistic, a threshold was established for each atlas: voxels with a probability higher than the threshold of being in the considered area were added to the mask. A different threshold was fixed for each atlas:

- Cerebellar: 20%;
- Cerebellum: 50%;
- WM tracts: 30%;
- Subcortical: 30%;
- Cortical: 30%;
- Lobes: 30%.

Those thresholds have been chosen to limit the overlapping of the different areas. They differ because the atlases are constructed with different probabilities. Indeed, the range of values used for each atlas varies: one atlas could be for example delimited by values between 20 and 50 while another would be delimited by values between 40 and 60. By setting a threshold of 40 for both, the first atlas would be very limited. After that, those masks were multiplied either by the brain mask or the WM mask introduced earlier, depending on which atlas is concerned.

4.4 Microstructure analysis

4.4.1 General evolution concept

For each one of the metrics treated in this work, two maps for each patient (T1 and T2) were available. Accordingly, a map is 3D representation of the value of a specific metric, in each voxel of the brain. The first step of this analysis was

to summarize the variations of each metric between both scans, for every region of interest. As the main goal is to observe the possible improvements occurring during the 18 days of abstinence, the variations are represented by a percentage of change of the concerned metric for each atlas map. The latter is computed in the following way for each region:

$$Change_{ROI}[\%] = \frac{mean(T2) - mean(T1)}{mean(T1)} * 100,$$

where $mean(T1)$ and $mean(T2)$ respectively represent the mean value of the metric inside the region of interest in the T1 and T2 map (mean of all the voxels located in the concerned region).

A positive number characterises an augmentation whereas a negative one suggests a diminution of the metric value over time in the ROI. All the values were then saved in an excel file in order to allow further analysis and data exploration.

A first rough analysis put in evidence two facts: there was very strong variations in behavioral data between the patients' set and several divergences in the different metrics when looking at the microstructural evolution. This forced us to adapt our approach: the idea was to group the similar microstructural tendencies in clusters and search for any correlation with the behavioral data. This clustering was also necessary to allow a clear and concise analysis, as evaluating every single subject separately is neither efficient, nor relevant for a master's thesis.

4.4.2 Clustering

The clustering method selected in this case is the K-means clustering. This method splits a dataset of n observations into K non-overlapping clusters. The idea is to make a partition of the space into K Voronoi regions. Each Voronoi region is associated to a centroid of which the location is fixed according to the data. The goal of this algorithm is to minimize within-cluster variances [94].

The main downside the K-means clustering algorithm (coming from `sklearn.cluster`, a Python library [95]), is its lack of consistency. Indeed, the centroids are at first randomly initiated, and then updated at each iteration in order to build the different clusters. But this random aspect induces a potential variation in the results, which means that the assignment of each patient to one of the clusters might vary each time the algorithm runs. In order to limit this randomness, an argument in the K-means algorithm can be set to perform the clustering a certain number of times and thus make the outcome more relevant. This parameter was set to 100.

In order to allow differentiation without complicating the treatment of data, the number of clusters was set to three. The clusters were made according to a « metric evolution » criteria. So the data given as input of the algorithm for each subject are the percentage of change of each metric, for each considered brain area. The resulting clusters were therefore expected to translate different tendencies. For instance, some metric could increase overall in the WM tracts for one of the clusters and stay relatively constant in another cluster, translating a recovery for the first group of patient and no real evolution for the second one.

This clustering was firstly done by considering each microstructural model separately, taking as input only the values of the model's metrics (Figure 4.13A), and secondly for all the models taken together (Figure 4.13B). However, as different microstructural models are used and might not always be 100% consistent with each other, this questions which data should be used for this part of the clustering. Indeed, if two models contradict themselves in some way, the combination of both models could potentially introduce bias in the clusters. Therefore, the four clusters' sets resulting from the single model clustering and the last clusters' set built on the basis of all the microstructural models were compared in order to find the most appropriate way to segment the data.

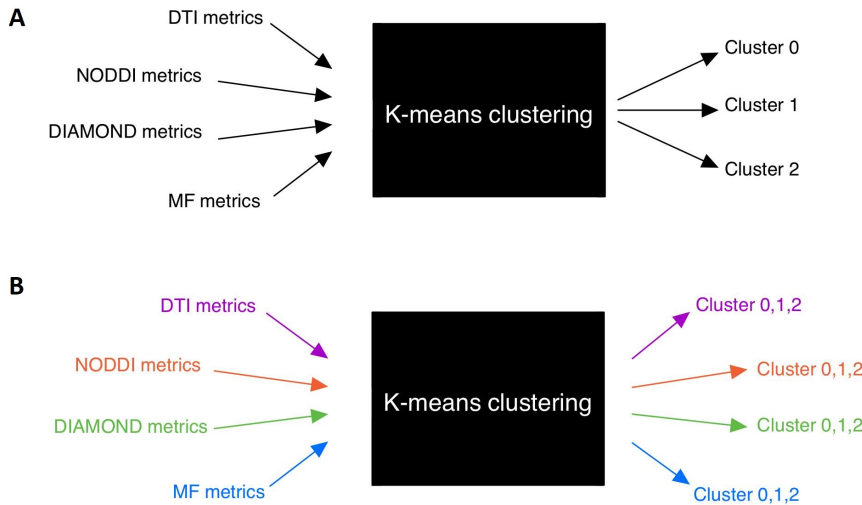


Figure 4.13: Clustering procedure. **A** Separate clustering taking as inputs, the metrics of every microstructural model separately, giving rise to different clusters for each one of them; **B** Final clustering taking as inputs, the entire set of metrics coming from all the models together.

Finally, another clustering method was used to confirm the final choice of clusters. This method is called affinity propagation and does not require the number of cluster to be determined before running the algorithm. As for K-means, the python function performing this algorithm comes from `sklearn.cluster` [96].

4.4.3 Statistical analysis

For each one of the models covered in this section, a preliminary Student's (t-test) analysis was performed in order to highlight the statistically significant metric changes in every ROI. This test allowed to take the variance of each dataset into consideration and to avoid the apparition of « false results » caused by high outlier variations.

To this aim, two one-sided paired t-test were made for each metric: the first one retrieved the ROI for which a significant increase appeared whereas the second one similarly brought some decreasing changes to the fore.

Concretely, a p-value and a t-score were computed for each atlas map and for

each metric, according to the following formula:

$$t = \frac{\bar{X}_D - \mu_0}{s_D / \sqrt{n}} \quad \text{and} \quad p\text{value} = Pr(T \leq (\text{or } \geq) t | H_0).$$

The t-score quantifies the difference between the population means and the p-value translates the probability of obtaining a t-score at least as extreme as the one observed in the dataset. A change was then considered as significant if a p-value smaller or equal to 5% was computed, meaning that the chances of wrongly declaring that the changes were significant was lower than 5%. Once the areas known as representative of an evolution according to the t-test were gathered, the average percentage of change could be computed for the considered metric, as a mean value over all patients in the considered cluster.

4.4.4 DTI analysis

The DTI model has been used for a couple decades now and has proven to be a robust way to investigate the condition of the brain microstructure over the course of alcoholism. For each one of those metrics (FA, MD, RD, AD), two maps corresponding to each patient (T1 and T2) were explored. Some T1 maps are shown as illustration in Figure 4.14.

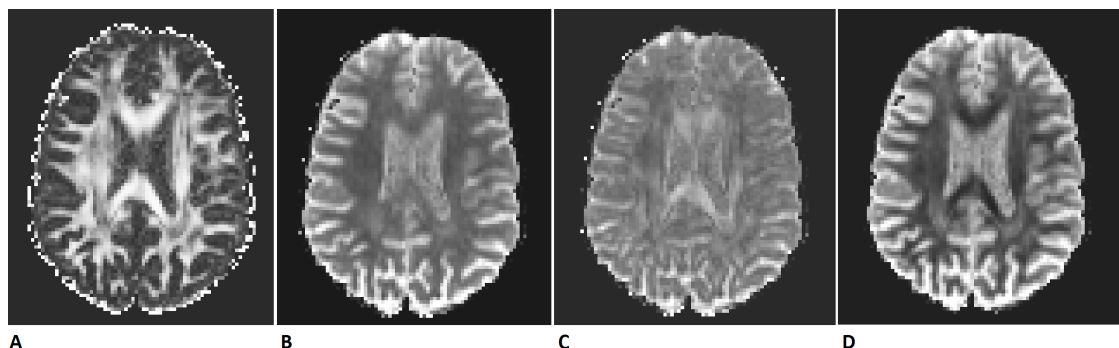


Figure 4.14: Representation of DTI metrics: **A** FA, **B** MD, **C** AD and **D** RD.

The aim of this DTI analysis was to summarize the variations of each metric, for every ROI as already explained in section 4.4.1. The focus was however only put on the significant variations highlighted by the t-test introduced earlier and not on the entire atlas set. Moreover, the complete atlas set was divided in several categories: the WM, GM, cerebellum, subcortical structures and lobes. The cerebellum, the subcortical structures and the lobes were considered as single categories because they are all made of both GM and WM. All the DTI metrics are displayed in Figure 4.14 and their meanings are illustrated in section 1.2.2.

4.4.5 NODDI analysis

The NODDI microstructural model provides, in the same way as the DTI model, two 3D maps per metric (T1 and T2). Among the metrics that ElikoPy outputs for this model, the metrics retained for the analysis are listed here below and illustrated in Figure 4.15:

- **fiso**: free water volume fraction⁵,
- **fintra**: intracellular volume fraction,
- **fextra**: extracellular volume fraction,
- **ODI**: fiber orientation dispersion index.

Figure 4.15A shows high **fiso** values in the ventricles, in which CSF resides, while values are relatively low in the rest of the brain. On its right, the quantification of intracellular matter presents low values in the ventricles in which no fibers are expected and high values in the WM, especially in highly anisotropic zones such as the CC. Similarly, Figure 4.15C highlights the importance of the extracellular compartment in a similar map but with higher values surrounding the WM tracts which confirms the biological truth. Finally, the **ODI** map has very high values in the CSF, as no directionality is observed and low values all around, where the CC and other fiber tracts are present.

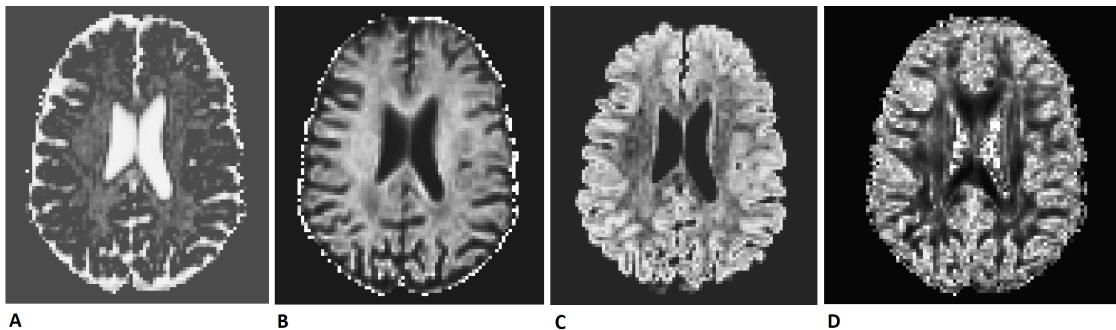


Figure 4.15: Representation of NODDI metrics: **A fiso**, **B fintra**, **C fextra**, **D ODI**.

The choice has been made to gather the information of the WM of the brain only. Indeed, this microstructural model has been built to study the different compartments in and around fibers, especially in the WM tracts. The extend to GM areas would have therefore introduced a lack of consistency with the initial applications of the model. Hence, in contrast to the DTI model for which 5 separate analyses were conducted, only 3 were done here: one on the WM tracts, another one on the subcortical structures and a last one on the cerebellum.

Regarding the study of the different metrics given as output by the model, a first analysis was made on the **ODI** metric. As explained in section 1.4.1, **ODI** is an indication of the dispersion of fibers inside a voxel. This value ranges between 0 and 1, the maximal value standing for highly dispersed fibers.

Combined to this first analysis, a second topic for research consisted in the relationship between three metrics: the extracellular, the intracellular and the free water volume fraction. As the addition of those three fractions is supposed to be equal to 1 in the brain of a subject, the variations in those three tissue types are also directly related. Hence, a mean value of those three quantities was computed for each atlas map studied and for each patient. Three new means were then calculated for each atlas map as the mean metric variations (percentage of change) over the subjects inside a cluster.

⁵The free water volume fraction is in this work, sometimes referred to as a compartment filled with CSF because of their very similar properties in terms of diffusion. It should however be mentioned that this is abuse of the language

4.4.6 DIAMOND analysis

In the same way as the NODDI model, several metrics can be extracted from the DIAMOND model, applied through the ElicoPy pipeline. First, some fractions files were retrieved. They each contained 3 files corresponding to a first fiber population, a second fiber population and an extra axonal compartment. The first two were named `frac_f0` and `frac_f1` while the last one was called `frac_csf`. Then, additional files named `t0` and `t1` were also explored. They both represent tensors from the first and the second fiber population respectively. Each one of these tensors has 6 components, allowing the construction of the $\bar{\mathbf{D}}$ tensor described in section 1.2.2. The reason why this tensor characterizing a spatial behavior in the 3D space with theoretically 9 components (3×3 matrix) only contains 6 components here, is because of the symmetry of the matrix. As the non-diagonal elements are expressed twice, 6 components are sufficient to characterize the entire tensor.

An additional property of this tensor is that it enables the computation of the four DTI metrics thanks to the equations (1.4) to (1.8). The latter were then called `cFA`, `cMD`, `cAD` and `cRD` to differentiate them from the original DTI metrics. As they were computed from each tensor, two maps per metric were obtained: one for each fiber population. This is the reason why the notion of fractions was added as weights on the different compartments. The new computed metrics were then named `wFA`, `wMD`, `wAD` and `wRD`, with the `w` standing for *weighted*, and computed according to the following formulas:

$$wFA = \frac{frac_f0 * cFA(f0) + frac_f1 * cFA(f1)}{frac_f0 + frac_f1}.$$

`wMD`, `wAD` and `wRD` were computed according to the same formula.

The interest of those new metrics is in fact the ability of the DIAMOND model to overcome the main limitation of the DTI. Indeed, by allowing the existence of two distinct fiber populations in a voxel, fiber crossing can be considered while the DTI model does not allow it. For this reason, the four DTI metrics can be erroneous when two fiber populations are crossing themselves, by just averaging their behavior. This situation is illustrated in Figure 4.16 from which we can extract some numbers:

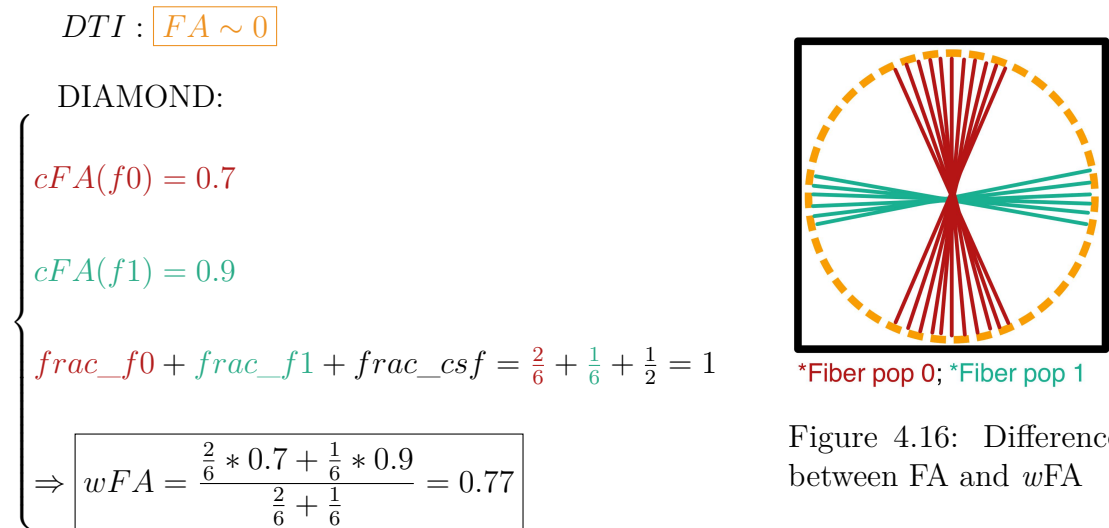


Figure 4.16: Difference between FA and *wFA*

As depicted here above, the DIAMOND model allows the existence of fiber populations crossing each other and enables the detection of highly anisotropic voxels. Indeed, a high wFA value can be observed while in the case of the DTI, it is considered to have an almost null FA, because one fiber population induces a high RD and the other one an identical AD.

All in all, the discrimination of fiber populations has proven its usefulness, especially for the computation of those new metrics. However, there are some considerable limitations in terms of interpretability of those separate fractions. For this reason, the files `frac_f0` and `frac_f1`, representing the volume fraction of each fiber population inside a voxel were combined to form a new metric called `frac_ftot`, translating the total fraction of fibers contained in each voxel. Its evolution was easier to interpret, as the fiber and CSF (free water) volume fractions inside a voxel are complementary. Two new files (T1 & T2) were thus created for each patient, for this new metric: maps of the total fiber fraction.

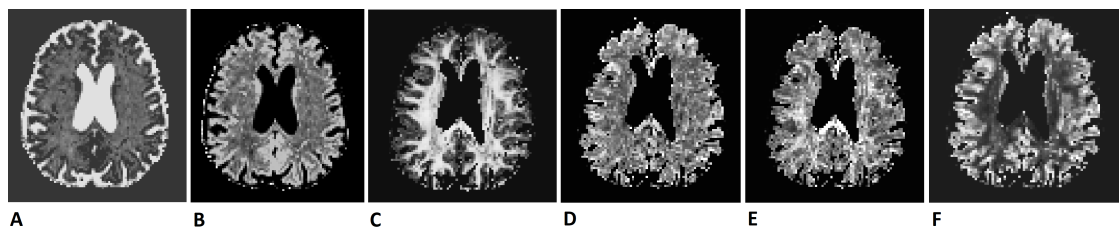


Figure 4.17: Representation of DIAMOND metrics: **A** `frac_csf`, **B** `frac_ftot`, **C** wFA , **D** wMD , **E** wAD and **F** wRD .

Consequently, a list of six metrics (see Figure 4.17) was kept to characterise the brain microstructure through the DIAMOND model:

- `frac_ftot`: total fiber volume fraction (built as a combination of the `f0` and `f1` files),
- `frac_csf`: free water volume fraction⁶,
- wFA : weighted FA,
- wMD : weighted MD,
- wAD : weighted AD,
- wRD : weighted RD.

4.4.7 Microstructure Fingerprinting

Similarly to the DIAMOND model, the MF method enables the discrimination of fiber populations inside a voxel. But again, the interpretation of the fraction of each population does not provide relevant information for the analysis of the microstructural evolution of the brain here. This is why both fractions were merged in the exact same way as the DIAMOND fractions, to form a new metric: `frac_ftot`.

Moreover, another metric is given as output by the MF model: the fiber volume fraction (fvf), again for each fiber population. With the same motivations as the

⁶The free water volume fraction is here, referred to as a compartment filled with CSF because of their very similar properties in terms of diffusion. It should however be mentioned that this is abuse of the language

one cited here above, a common **fvf** named *weighted* **fvf** (**wfvf**) was created. The latter represents the proportion of fibers (from both fiber populations) inside the voxel, without taking the CSF compartment into account. **wfvf** was computed according to the following formula:

$$wfvf = \frac{frac_f0 * fvf_f0 + frac_f1 * fvf_f1}{frac_f0 + frac_f1} = \frac{fvf_tot}{frac_ftot}. \quad (4.1)$$

This **wfvf** only focuses on the concentration of fibers inside the fiber compartment, as illustrated in Figure 4.18.

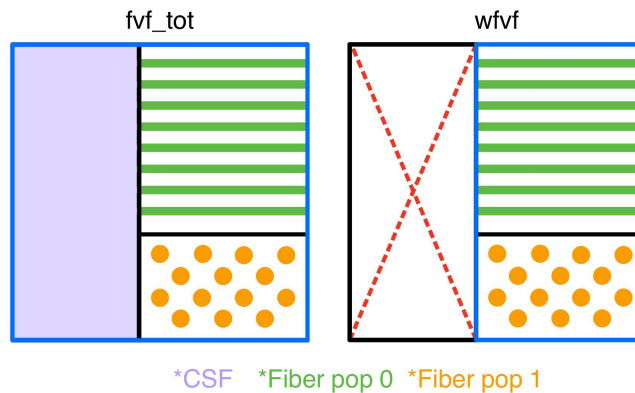


Figure 4.18: Difference between **fvf_tot** and **wfvf**: **fvf_tot** estimates the proportion of fibers in the entire voxel whereas **wfvf** only considers the fiber compartment and evaluates the concentration of the fibers.

The exhaustive list of MF metrics treated in this work is thus listed below and the corresponding maps are shown in Figure 4.19.

- **frac_csf**: free water volume fraction⁷,
- **frac_ftot**: total fiber volume fraction (built as a combination of the **f0** and **f1** files),
- **fvf_tot**: fiber volume fraction,
- **wfvf**: weighted fiber volume fraction.

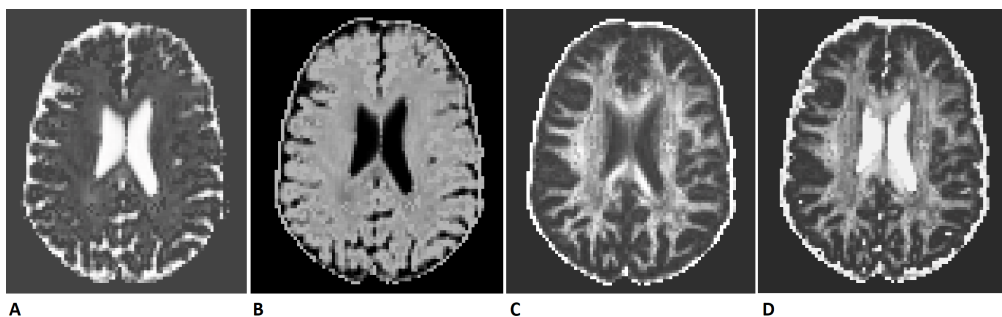


Figure 4.19: Representation of MF metrics. **A** **frac_csf**, **B** **frac_ftot**, **C** **fvf_tot**, **D** **wfvf**.

⁷The free water volume fraction is here, referred to as a compartment filled with CSF because of their very similar properties in terms of diffusion. It should however be mentioned that this is abuse of the language

The volume fraction of CSF and the total volume fraction are two values that compensate each other: their addition always equals 1. The two maps (Figures 4.19A and B) are therefore complementary. This visualization confirms the consistency of the model with the biology of the brain and its diverse compartments.

4.5 Treatment of the behavioral data

All the tests introduced in section 4.1 were performed twice, the first time on day 2 (T1) and the second time on day 17 (T2). The scores were then partly treated as an evolution, which means that the focus was on the changes of those scores between T1 and T2. Their evolution was, in opposition to the one of the microstructural metrics, characterised as a difference in time and computed as follows:

$$Diff = Score(T2) - Score(T1). \quad (4.2)$$

A last indicator for each one of the subjects is the number of alcohol unit that the subjects drink on a daily basis. An alcohol unit equals 10ml or 8g of pure alcohol which corresponds to a single shot of spirits or half a pint of lower-strength lager/beer/cider (568ml, ABV 3.6%) [97].

4.6 Motion analysis

Obviously, the conditions of the scan have to be taken into consideration to ensure that no measure could be biased because of external factors. One of those well-known factors is motion. Indeed, the subject's dynamic during the scan period can significantly influence the outcome of the diffusion and mislead the eventual conclusions of the study. This is why four measures for each scan were explored: the average absolute motion (mm), the amount of outlier slices (%), the average SNR ($bvalue = 0 s/mm^2$) and the average Carrier to Noise ratio (CNR) ($bvalue = 999 s/mm^2$). Among them, the two first (abs. motion and outliers) should be as low as possible whereas the two others (SNR and CNR) are desired to be high to ensure good quality data.

Another type of motion that influences the analysis is the difference between the scan in T1 and the re-scan in T2. Usually, some microstructural changes of about 5% for the WM and 10% for the GM can be observed between two successive scans, because of the slight motion of the patient in the MRI. For this reason, a threshold was set to 8% to discriminate relevant changes, and only changes above this threshold are discussed in the rest this work.

4.7 Volumetric changes analysis

As explained in the section 3.4.2, one of the most common effects of alcohol on the brain is volumetric changes.

As a first step, the overall volumetric changes were studied, i.e., how the volumes of CSF, WM and GM evolve between the two scans. To do so, the difference in volume between T1 and T2 was computed with help of three files given as output of the ElikoPy, each corresponding to a mask of the CSF, WM and GM respectively. Those volume were defined as the sum of pixels belonging to the masks. From this, three metrics were obtained: `volume_CSF`, `volume_WM` and `volume_GM`. Then,

those variables were divided by the overall brain volume to get their relative volume.

As a second step, this analysis was transposed to specific regions of the brain. As we created a mask for each atlas map treated for the microstructural analysis, the number of voxels contained in each zone was easily accessible and the evolution of their volume was computed in order to spot noticeable changes.

5 Results

This section gathers the observations resulting from the different analyses performed and explained in section 4. They will be described and compared to the expectations that were set, either on the basis of our literature review (see section 3), or simply on logical correlation between the different variable studied. Many of the studied regions are separated into a left and right part which are respectively referred to L and R in the following sections.

5.1 Clusters

As explained in the previous section, the interest of dividing the patients into distinct clusters is to perform separate analysis on each one of them, as the evolution of their brain can differ. The number of clusters was set to three and they will therefore be called cluster 0, cluster 1 and cluster 2.

It appears that the outputs of the clustering are not exactly as balanced as expected. Indeed, the algorithm tends to isolate some single patients in a cluster and build a big cluster with the rest of the patients' set, which translates the presence of outliers within the set. This happens to be the case when the number of clusters (K) is too low. Once the latter is increased, all the outliers are solely attributed to a cluster and new balanced clusters can rise from the non-outlier group. For this reason, the choice has been made to create a « side cluster » composed of the outliers, always found alone in a cluster, and to assign them to cluster 0. This side cluster is therefore composed of subjects that differed significantly from the rest of the group but that did not represent any specific pattern and thus, no real similarity with each other.

To overcome this and spot some real clusters inside the rest of the group, the number of clusters was temporarily set to different higher values. The algorithm was therefore launched for 3, 5, 7 and 9 clusters to see which patterns would come out. Additionally, another clustering method called affinity propagation was used as a double check, to see if a similar outcome would appear with a totally different algorithm. The affinity propagation algorithm does not require any pre-determined number of clusters and therefore creates as many clusters as necessary to split the data set in the best way possible.

When the clustering algorithm is run four times with as input the metrics of only one of the models, the emerging clusters always differ. Consequently, the final choice is to build clusters according to a combination of all the microstructural models. Indeed, the more inputs a model has, the more accurate it is supposed to be. Moreover, randomly picking one of the models would suggest that the trust is hypothetically placed on that particular model, and that is not the case as each model brings something to the analysis of this thesis, and that they will all be covered. Consequently, all the relevant metrics of each model were selected according to their potential to bring insights to the microstructural evolution of the brain and used as inputs of the clustering algorithm. They are all listed in sections 4.4.4 to 4.4.7.

As shows Table 5.1, the side cluster is already defined when K is set to 5 and

gets bigger when this number is increased to 7. But by increasing K one last time to 9, a new cluster of eight patients stands out. This is the set of clusters that defines the final cluster assignment. The side cluster is composed of the outliers colored in blue and orange. Cluster 2 gathers the subjects colored in green that represent a similar pattern. Finally, cluster 1 is composed of all the other subjects. The clustering with the affinity propagation method confirms the relevance of this choice as it splits the set of patients in a very similar way.

In order to make sure that cluster 1 is a real cluster with subjects showing similarities in metric evolution and not a group of patients that did not fit in the cluster 2, a new clustering algorithm with the affinity propagation method was run on the cluster 1. The resulting clusters confirmed the relevance of this cluster: only three clusters are formed by the algorithm, two composed of single patients, and one big cluster containing the 18 others. The fact that the algorithm did not create more than 3 clusters reflects the similarity of microstructural changes for the patients contained in cluster 1.

To illustrate the result of the clustering, Figure 5.1 displays the mean value of three DTI metrics: FA, AD and RD in the CC. The subjects belonging to cluster 1 are shown in black whereas the ones in cluster 2 appear in green. We can see with this figure that the colors are relatively separated.

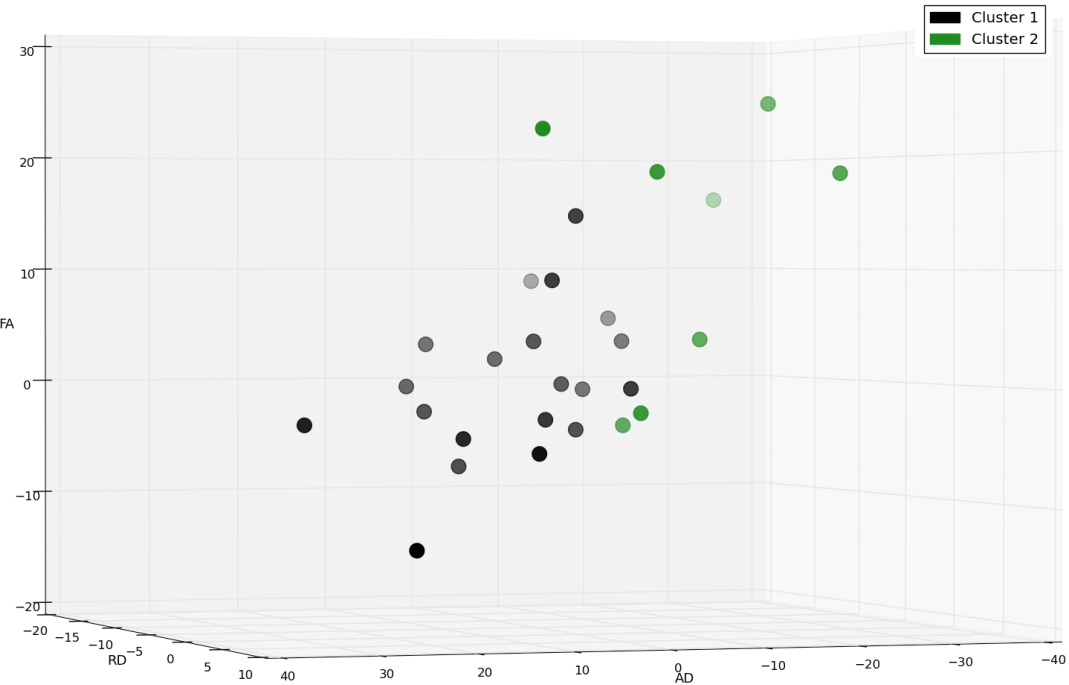


Figure 5.1: Clustering according to DTI metrics (FA, AD and RD) in the CC.

Table 5.1: Clusters formed by the K-means algorithm for different values of K and result of the affinity propagation method.

Model	K-means			Affinity propagation
K =	5	7	9	Not specified
[02,04,08,09,11, 12, 13 ,14,15, 17 , 18, 19 ,20,21,22, 24,27,28,30, 31 , 32,33,34, 37 ,39, 41 ,42, 43 ,45, 46]	[02,04,08,09,11, 12, 13 ,14,15, 17 , 18, 19 ,20,21,22, 24,27,28,30, 31 , 32,33,34,39,42, 43 ,45, 46]	[02,04,08,09, 11,12,14,15, 18,20,21,22, 24,27,28,30, 32,33,34,39,42, 34,39,42,45,46]	[02,04,08,09, 11,12,14,15, 18,20,21,22, 24,27,28,30, 34,39, 41 , 43 , 45, 46]	[02,04,08,09, 11,12,14,15, 18,20,21,22, 24,27,28,30, 34,39, 41 , 43 , 45, 46]
	[26,40]	[26,40]	[13, 17 ,19,31, 32,33, 43 ,46]	[13,19,31,32, 33]
	[05]	[05]	[05]	[05]
	[35]	[35]	[35]	[35]
	[36]	[36]	[36]	[36]
		[37]	[37]	[37]
		[41]	[41]	[17]
			[26]	[26]
			[40]	[40]
	FINAL CLUSTERS			
0 (<i>side cluster</i>)	[05, 26 ,35,36, 37 , 40 ,41]			
1	[02,04,08,09,11,12,14,15,18,20, 21,22,24,27,28,30,34,39,42,45]			
2	[13, 17 ,19,31,32,33, 43 ,46]			

5.2 Motion

The patients have been ranked according to how much motion affected their scans in comparison to each other. For this, all the scores attributed to each motion parameter have been normalized. In other words, each parameter (e.g. absolute motion) has been taken one by one and divided by the maximum value of this parameter over the whole set of scans, in order to obtain values between 0 and 1 reflecting how big each value is in comparison to the ones of the other scans. But, as explained earlier, two out of the four values used must be as low as possible: the SNR and the CNR, in opposition to the others. The same methodology was thus applied for those two parameters, but they were then subtracted from one. The following equations will help for comprehension:

$$\begin{aligned} \text{Relative abs-motion}[i] &= \text{abs-motion}[i] / \max(\text{abs-motion}), \\ \text{Relative outlier-slices}[i] &= \text{outlier-slices}[i] / \max(\text{outlier-slices}), \\ \text{Relative SNR} &= 1 - (\text{SNR}[i] / \max(\text{SNR})), \\ \text{Relative CNR} &= 1 - (\text{CNR}[i] / \max(\text{CNR})). \end{aligned}$$

where i represents the number of the scan. The latter ranges between 1 and 70 as two scans per patients are treated.

Each patient is thus represented by 8 score (4 parameters * 2 scans), all ranging between 0 and 1, and translating how much the scans were impacted by motion. To obtain the final ranking between all the subjects, an average of the 8 scores is then assigned to each patient and the ranking is made on this basis. For a patient, the lower the score, the better and more reliable the scans.

The final ranking in ascending order is the following: [13, 20, 28, 33, 09, 41, 05, 18, 24, 22, 26, 39, 46, 04, 31, 15, 43, 30, 45, 02, 35, 14, 19, 21, 32, 40, 11, 42, 27, 08, 36, 12, 37, 17, 34]. The patient 13 is thus the one with highest quality scans whereas patient 34 is the most impacted by motion.

What we can retrieve from this list is that the patients belonging to each cluster are relatively dispersed with respect to the ranking. If all the patients belonging to the same cluster were for instance, all at the end of the list, this would be the sign that motion highly influences the results and thus the clusters. We can therefore reasonably conclude that despite motion can have a significant impact on the set of data, it does not call into question the process to define our clusters.

5.3 DTI analysis

The four DTI metrics introduced in this work can all be signs of specific biological phenomena taking place inside the brain. However, they do not all have an easy and interpretable meaning everywhere. For this reason, a focus will be put on the MD for areas located in the GM and in the brain lobes, and the three other metrics will be considered in the WM tracts, as well as the cerebellum and subcortical areas in which both gray and white matter can be found. As the diffusion metrics are related by equation 1.7: the measure of FA and two diffusion metrics (AD and RD) are thus enough to characterise a voxel.

5.3.1 Gray matter and lobes

As shown in the Figures 5.2 and 5.3, there are some discrepancies in the metrics variation in the two clusters to analyse. Cluster 1 does not show any significant changes in GM areas. By contrast, cluster 2 is characterised by a decreasing MD in several GM regions as well as in the *Temporal Lobe*, as depicted in Figure 5.2.

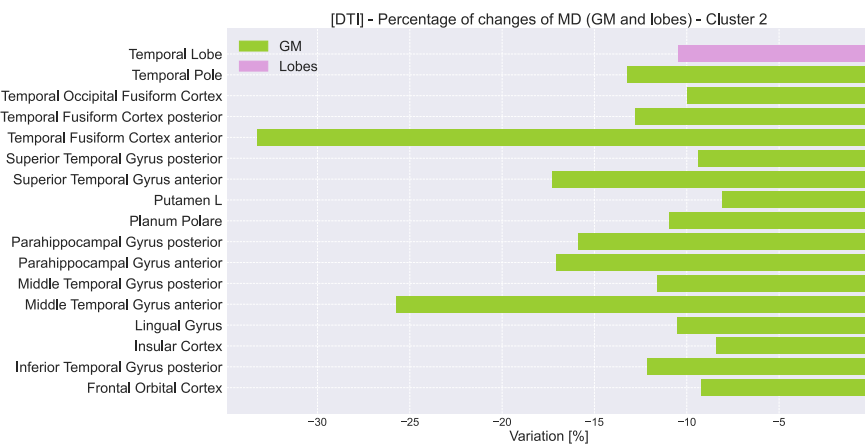


Figure 5.2: Summary of all regions showing significant MD changes (GM areas and lobes) considering cluster 2.

This global change at the lobe scale is in agreement with the more particular GM areas standing out of this analysis. As shows Figure 5.2, the majority (11/16) of the regions displayed are located in the temporal lobe.

5.3.2 White matter, cerebellum and subcortical structures

Cluster 1

When it comes to the cerebellum, new observations can be discussed. Firstly, an almost complete absence of results in cluster 1 can be pointed out, with a single conspicuous zone: the *Cerebellum X L*. As shown in Figure 5.3, this cerebellar lobule is characterised by an increased FA and AD, with no significant change regarding the RD.

In the case of WM areas, the *Middle Cerebellar Peduncle* and the *Cingulum subsection Temporal L* stand out with the increase of only one of the DTI metrics (either AD or RD as depicted in Figure 5.3), suggesting a slight evolution in at least one other metric that does not exceed the 8% threshold. One can observe the same behavior in the *Brain Stem* which is a subcortical structure.

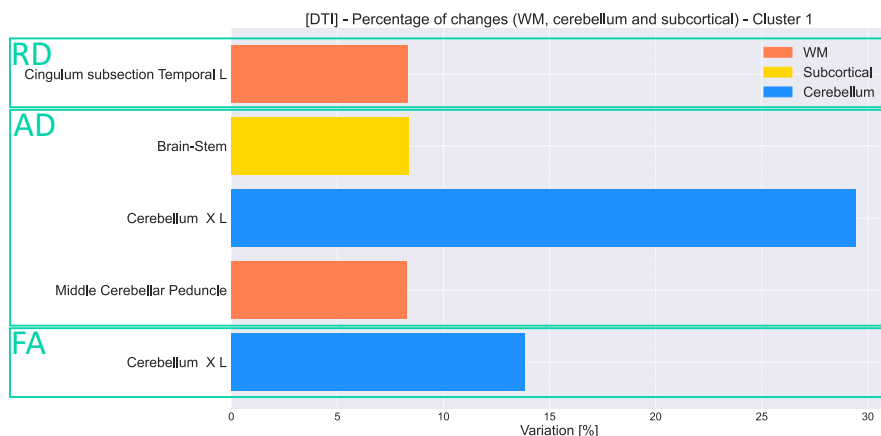


Figure 5.3: Summary of all regions showing significant RD (top), AD (middle) and FA (bottom) changes considering cluster 1.

Cluster 2

Secondly, in cluster 2, important variations are observed in the cerebellum (see Figures 5.4 to 5.6). The FA increases in 8 out of its 21 subdivisions and almost all of them (17/21) are impacted by AD and RD decrease. It suggests that, in the 8 regions showing FA augmentation, the RD decreases more than the AD. In contrast, they both decrease homogeneously when FA shows no significant change.

By comparing graphs 5.5 and 5.6, those expectations are confirmed. Indeed, among the 8 FA increasing areas, 7 present a stronger RD decrease. Regarding the only area that does not follow this behavior, the AD and RD changes are almost equal (0.16% of difference), and those numbers are a representation of a global behavior among this cluster. And yet, the clusters were built according to a wide set of metrics coming from four different microstructural models. This means that for a single metric, we do not necessarily observe similar behaviors for every patient of the cluster. An outlier patient for the concerned metric can therefore have a big impact on the expected results.

Moreover, the 9 other regions showing no FA difference but a noticeable evolution of AD and RD have relatively poor diffusion variance: a third⁸ of the zones (3/9) shows slightly stronger RD in opposition to the two other thirds⁹ (6/9).

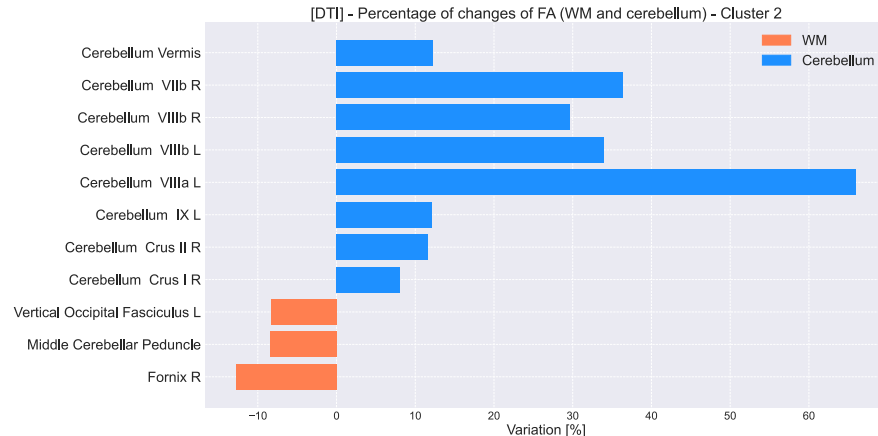


Figure 5.4: Summary of all regions showing significant FA changes (WM and cerebellum) considering cluster 2.

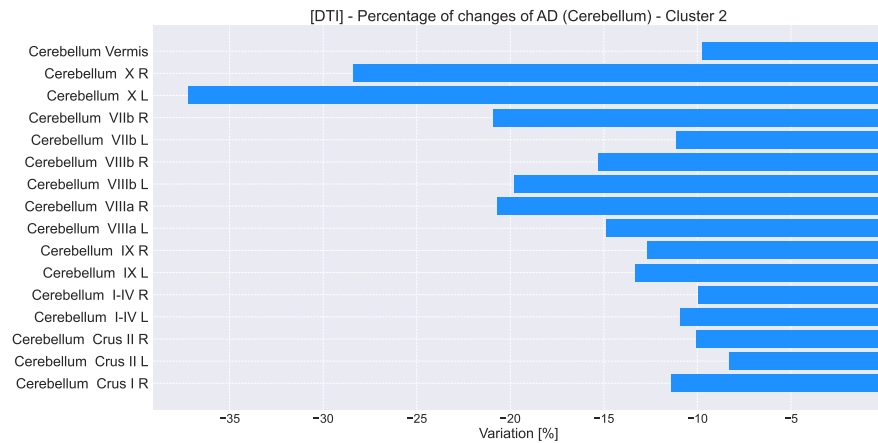


Figure 5.5: Summary of all regions showing significant AD changes (cerebellum) considering cluster 2.

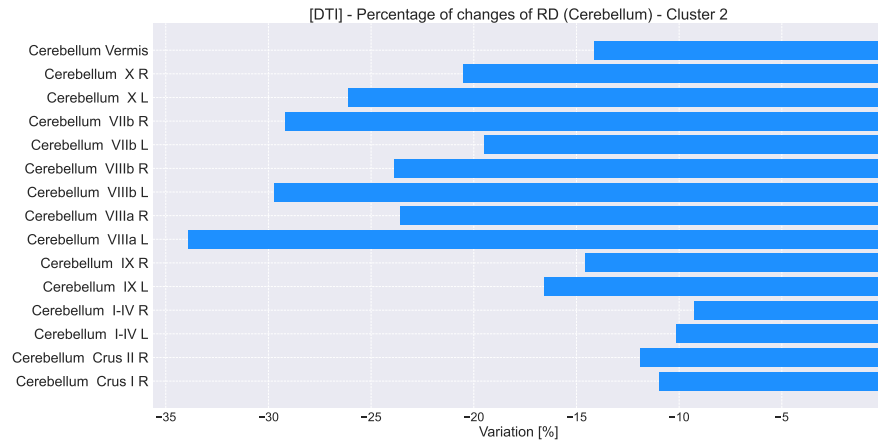


Figure 5.6: Summary of all regions showing significant RD changes (cerebellum) considering cluster 2.

⁸ $\text{mean}(\text{changes}_{\text{RD}} - \text{changes}_{\text{AD}}) = 5.2\%$

⁹ $\text{mean}(\text{changes}_{\text{RD}} - \text{changes}_{\text{AD}}) = -4.5\%$

Finally, in the brain WM, the *Middle Cerebellar Peduncle* and the *Fornix R* show a decrease for the 4 DTI metrics. It suggests a stronger AD decline which is indeed the case, as one can see in Figures 5.7 and 5.8.

Additionally, the *Vertical Occipital Fasciculus L* is characterised by a decreased FA but does not seem to present real significant diffusion changes. Moreover, some other WM tracts and subcortical structures do not show any significant FA change despite the diffusion decline. Among them, 15 show significant alterations of both AD and RD and 11/15 show a stronger AD decrease. The difference is however relatively small, as the maximal difference between changes in AD and RD is about 5% with a mean value worth 2%.

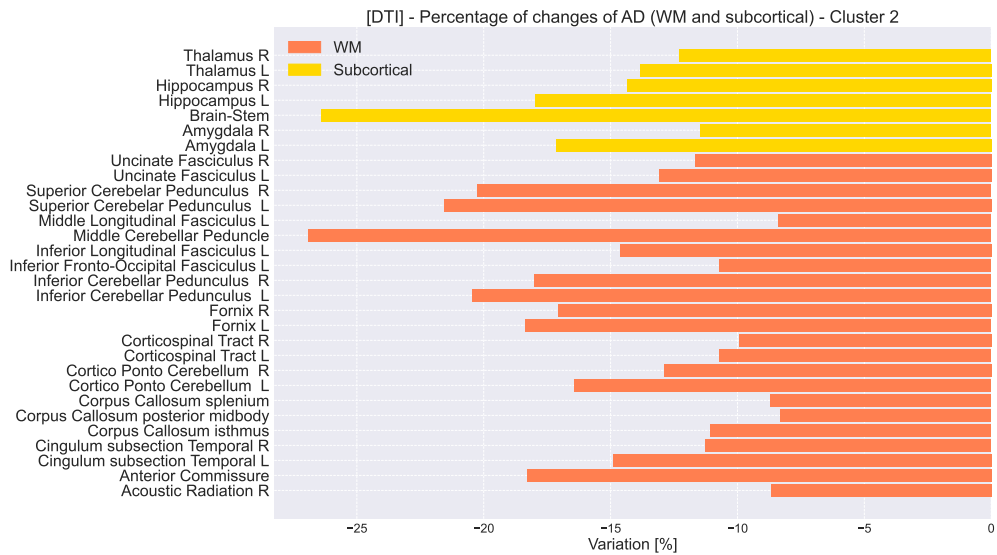


Figure 5.7: Summary of all regions showing significant AD changes (WM and subcortical areas) considering cluster 2.

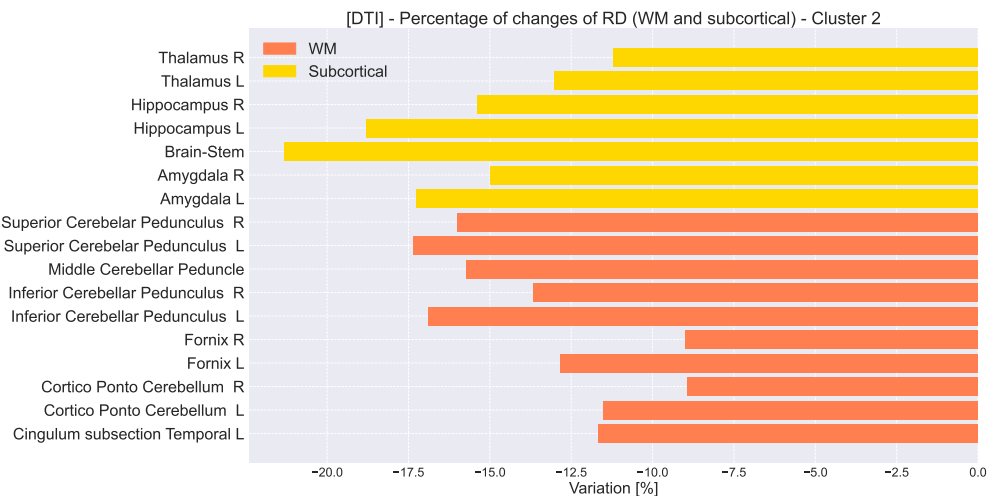


Figure 5.8: Summary of all regions showing significant RD changes (WM and subcortical areas) considering cluster 2.

5.4 NODDI analysis

The NODDI analysis can be divided into two parts: On the one hand, several metrics can be analysed separately and hypotheses about the microstructural behavior can be derived from them. on the other hand, a check can be made on the consistency of the metrics relatively to each other. This analysis concerns the coherence of the model itself and is detailed in appendix C.1.

As already mentioned, NODDI is a microstructural model that was built specifically for WM tracks. However, as the cerebellum and subcortical regions are composed of both WM and GM, it makes sense to study them also in this model. Therefore, the following sections will focus only on these ROIs in the brain. The two other microstructural models used in this thesis (DIAMOND and MF) will similarly only base their analysis on the WM, the cerebellum and subcortical areas of the brain.

Cluster 1

First of all, cluster 1 does not seem to have significant change of **fintra** or **ODI** in any ROI, neither in the WM, nor in the cerebellum and the subcortical regions. There is no increase or decrease of more than 8%. But if we first focus on what is happening in the WM and in the cerebellum, 12 areas are highlighted with a significant increase of **fextra** and 9 with a meaningful decrease of **fiso** (see Figures 5.9 and 5.10). However, only 4 regions, the *Optic Radiation L*, *Cerebellum IX L*, *I-IV R* and *I-IV L* show a significant evolution in both metrics. The rest of the zones appearing in Figures 5.9 and 5.10 only exhibit a decrease in one of the metric (**fiso** or **fextra**) between the two scans. Regarding the subcortical areas, 3 of them show a significant increase of **fextra** and another one is represented by a **fiso** decrease (see Figure 5.11).

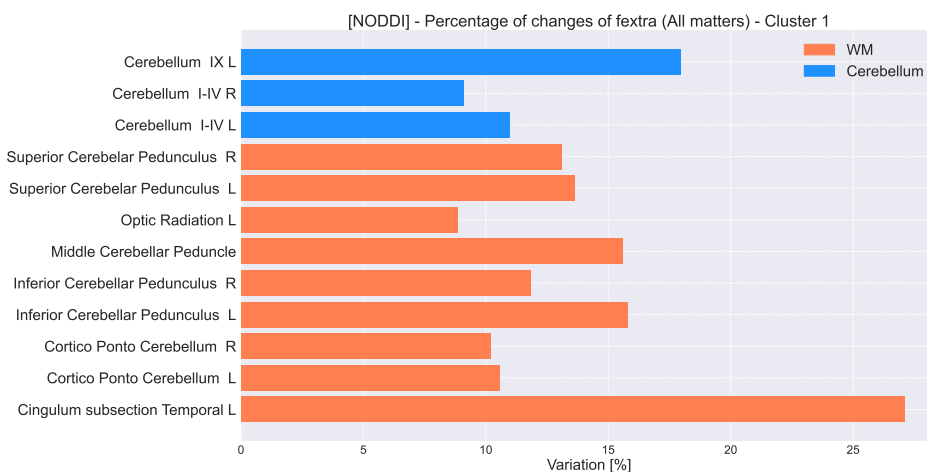


Figure 5.9: Summary of all regions showing significant **fextra** changes (WM and cerebellum) considering cluster 1.

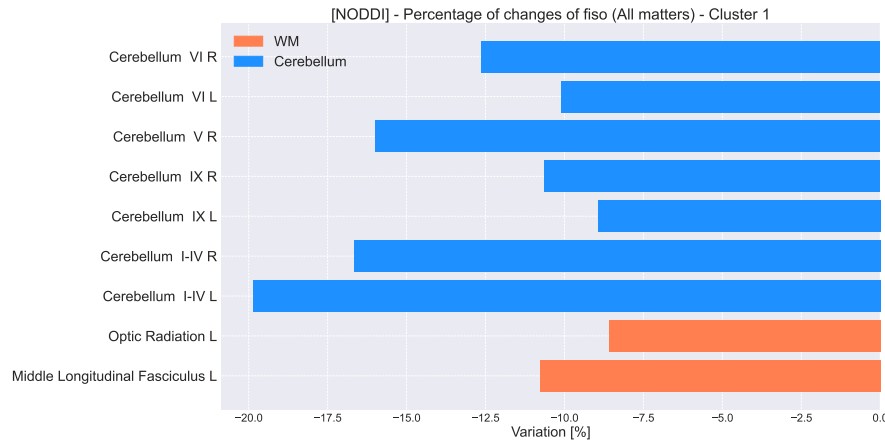


Figure 5.10: Summary of all regions showing significant **fiso** changes (WM and cerebellum) considering cluster 1.

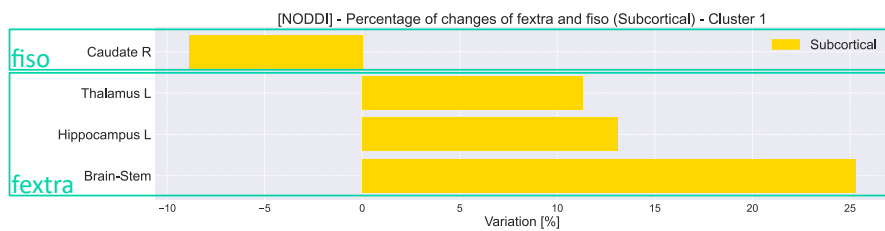


Figure 5.11: Summary of all regions showing significant **fextra** (bottom) and **fiso** (top) changes (subcortical areas) considering cluster 1.

Cluster 2

If one considers now the data arising from cluster 2, it seems to display more significant areas than cluster 1. By having a first look at Figures 5.12 to 5.18, one can see that **fintra** has a global tendency to increase in all brain matters (WM, cerebellum and subcortical), in opposition to **fextra** that only shows decreasing values. **fiso** is more variable and seems to increase and decrease in the WM and the cerebellum, depending on the zone, whereas it never shows any significant change in the subcortical structures. Finally, **ODI** only increases in the WM and the cerebellum, without having any significant evolution in the subcortical structures either.

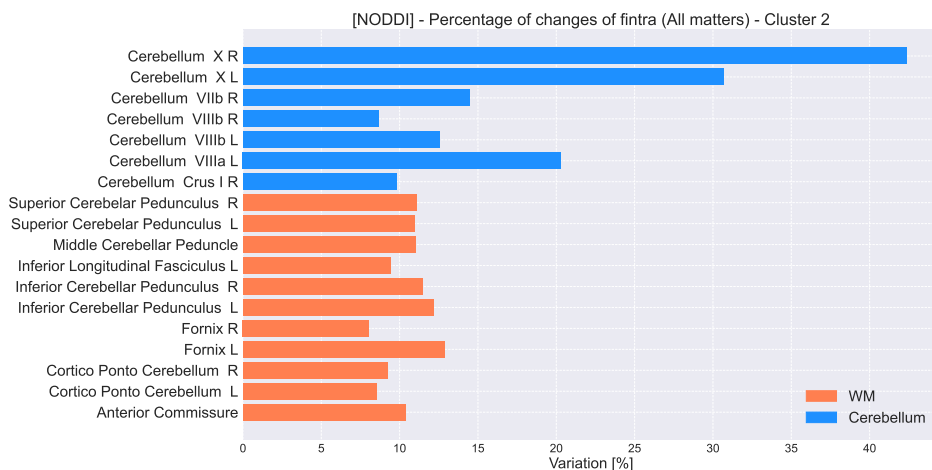


Figure 5.12: Summary of all regions showing significant **fintra** changes (WM and cerebellum) considering cluster 2.

To begin, when analysing what is going on in the WM and the cerebellum, 18 regions show a significant change according to **fintra**, 39 to **fextra**, 18 to **fiso** and 29 to **ODI**. Among all these areas, only two show a significant evolution in all four metrics. The *Superior Cerebellar Peduncle R* and *L* have an increase in **fintra**, **fiso** and **ODI**, and a decrease in **fextra**. For the remaining regions, there are 13 possible scenarios. Four of them appear when an area shows a significant change in only one of the four metrics. Two regions only show an increase in **fintra**: the *Inferior Longitudinal Fasciculus L* and the *Cerebellum Crus I R*, 3 are only showing a meaningful decrease in **fiso**, 8 a decline of **fextra** and 7 an increased **ODI**.

Among the rest of the areas displayed in Figure 5.12, there are 5 possible scenarios involving an increased **fintra**. It can be combined with a decreasing **fextra**, as it is the case for two regions, or with an increasing **ODI**, as shows the *Fornix R*. 10 other areas also show an increased **fintra** accompanied with a decrease in **fextra** and a last increase in **fiso** for 2 of them, or in **ODI** for the last 8. To finish with the changes in **fintra**, the *Cerebellum X R* is the only area characterised by a decreasing **fiso** while **fintra** and **ODI** are increasing.

Finally, the three last scenarios are those for which **fextra** is evolving in the opposite way of either **fiso** or **ODI**. Out of the 39 areas with a significant decrease according to **fextra**, 7 also show an increase according to **fiso**, 7 to **ODI** and the last 3 are depicting a meaningful increase in both metrics. All this information is summarised in Figures 5.13 to 5.15.

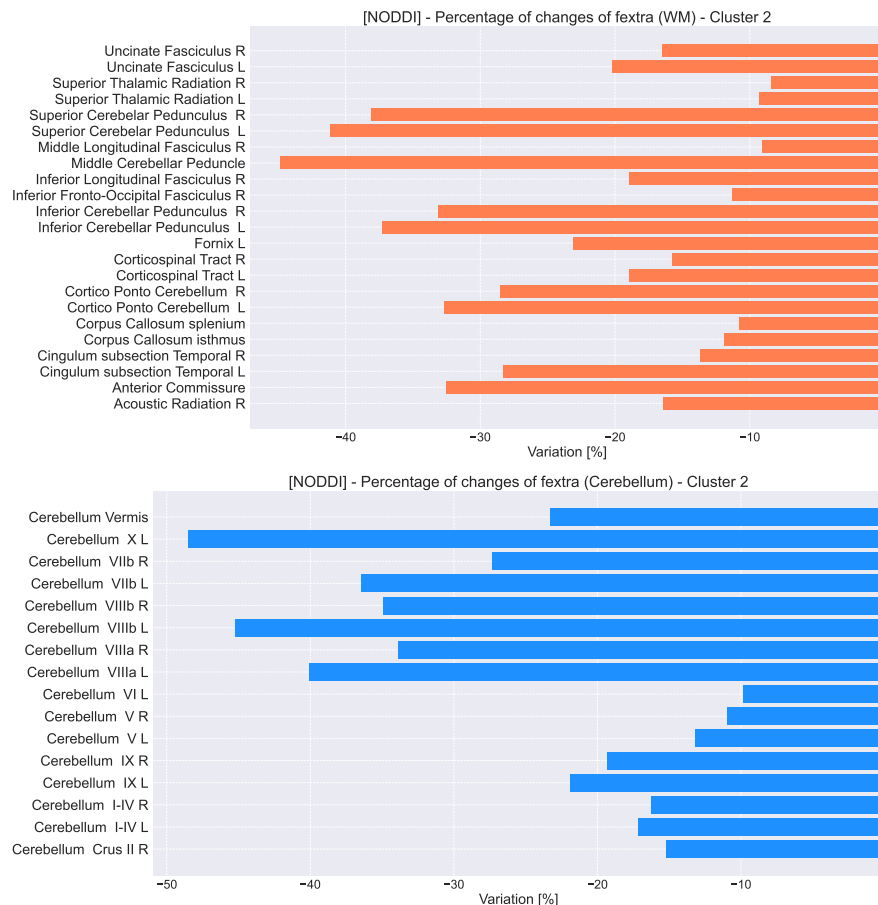


Figure 5.13: Summary of all regions showing significant **fextra** changes (WM (top) and cerebellum (bottom)) considering cluster 2.

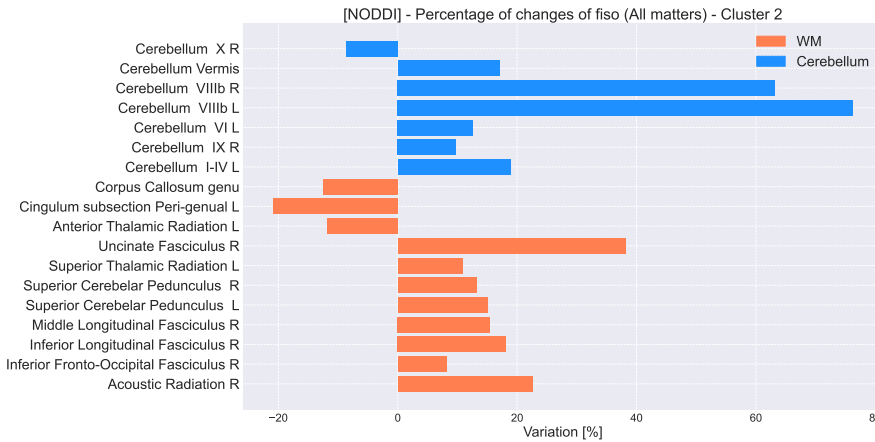


Figure 5.14: Summary of all regions showing significant **fiso** changes (WM and cerebellum) considering cluster 2.

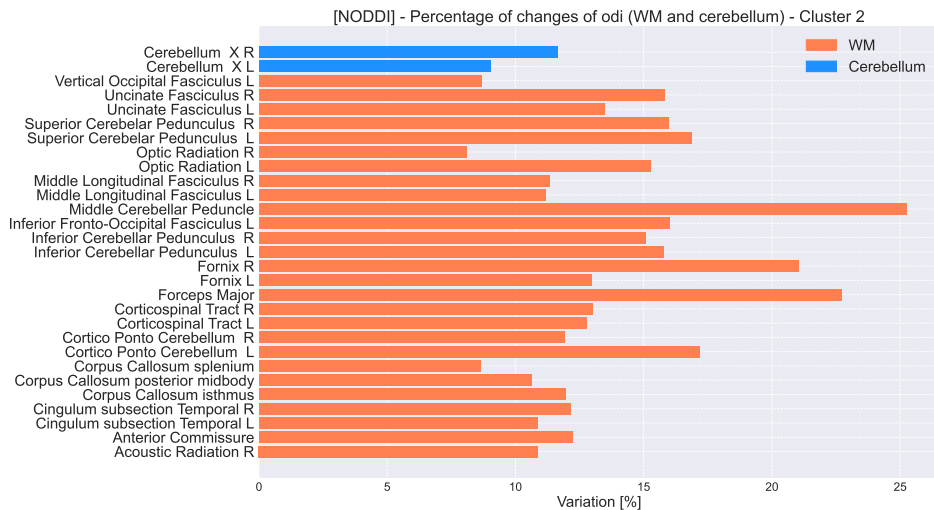


Figure 5.15: Summary of all regions showing significant **ODI** changes (WM and cerebellum) considering cluster 2.

Lastly, the subcortical areas are showing the same general behaviour as the ones in the WM and the cerebellum. Among all the zones displayed in Figures 5.16 to 5.18, only one area, the *Amygdala L*, is showing a significant evolution in the four metrics. Then, 4 other regions are showing a significant evolution in three metrics. On the one hand, the *Thalamus R*, the *Hippocampus R* and *L* have an increased **fintra** and **fiso** combined with a decline in **fextra**, while on the other hand, the *Brain Stem* shows the same evolution for the first two metrics combined this time with an augmentation of **ODI**. Next, 2 regions have only changes in two of the metrics: for the *Thalamus L*, it is in **fintra** and **fextra** while for the *Amygdala R*, it is only in **fextra** and **fiso**. To finish, two areas indicate a meaningful change in only one metric, either **fextra** for the *Caudate L* or **fiso** for the *Cerebral White Matter L*.

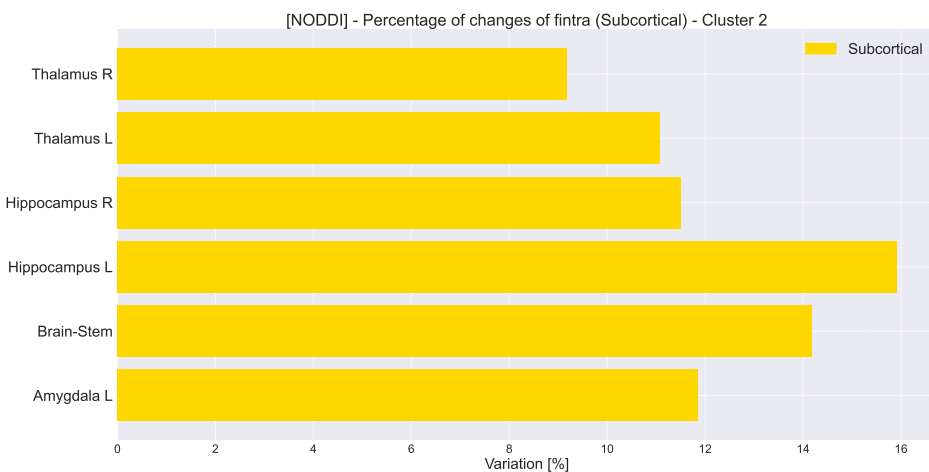


Figure 5.16: Summary of all regions showing significant **fintra** changes (subcortical areas) considering cluster 2.

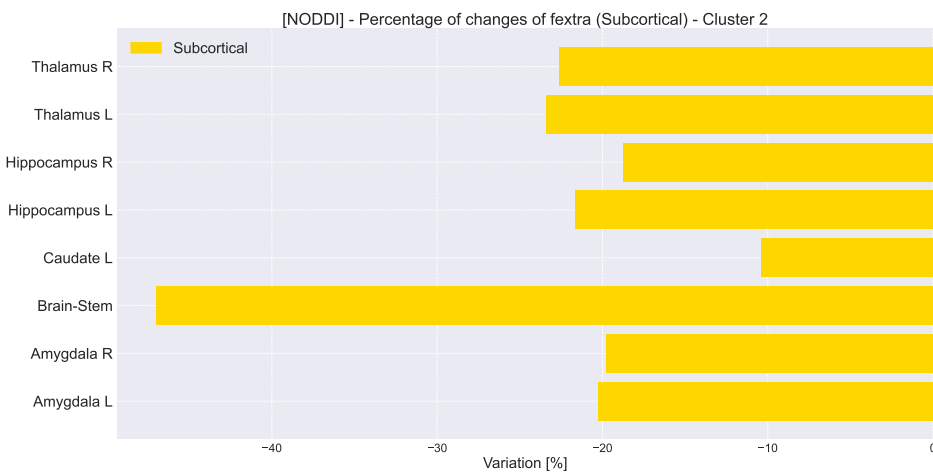


Figure 5.17: Summary of all regions showing significant **fextra** changes (subcortical areas) considering cluster 2.

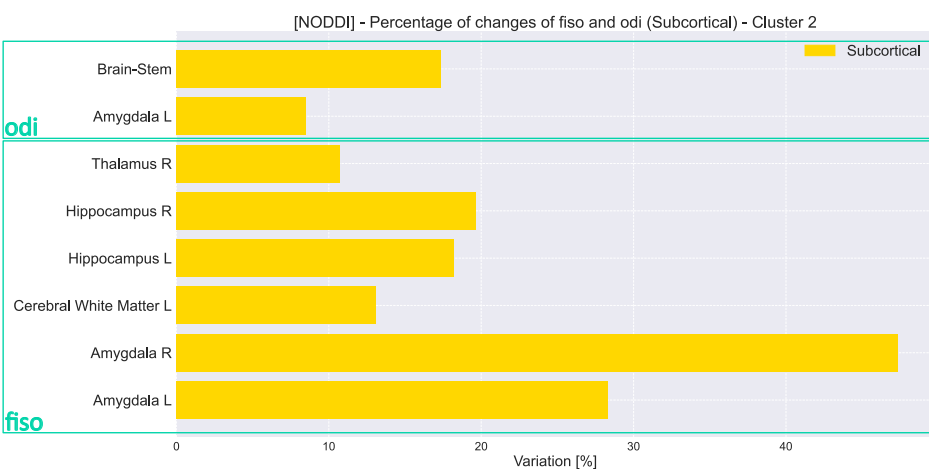


Figure 5.18: Summary of all regions showing significant **ODI** (top) and **fiso** (bottom) changes (subcortical areas) considering cluster 2.

5.5 DIAMOND analysis

A similar analysis to the one of DTI model can be performed for the new metrics created for DIAMOND: wFA , wMD , wAD and wRD . However, as this model is more convenient to study WM tracts than GM, a focus will be put on those regions by analysing trends in all metrics except for wMD as previously explained for MD (see section 5.3). Indeed, some zones can be grouped according to the evolution of those three metrics and depict some specific scenarios.

Similarly to the NODDI model, the coherence of the DIAMOND metrics can be evaluated to make sure that the logical relationship between the CSF and the total fiber fractions is respected. This analysis can be found in appendix C.2.

Cluster 1: wFA, wAD, wRD

In the case of cluster 1, no significant change is found regarding the *weighted* metrics. As a very small amount of change were already identified in cluster 1 for the corresponding DTI metrics, those results suggest a consistency between the DTI and DIAMOND model. The fact that the FA, AD, RD changes shown in Figure 5.3 are not appearing here, suggest that those changes might be due to a limitation of the DTI model that does not take possible fiber crossing into account.

Cluster 2: wFA, wAD, wRD

Cluster 2 involves a few more areas and metric evolution, represented by 4 distinct situations. First, the *Middle cerebellar peduncle* can be represented by the following scenario: wFA and wAD are decreasing. A second scenario can be observed for the *Cerebellum X L* and the *Brain Stem*, that are characterised by an homogeneous decrease of both diffusion metrics, that thus does not involve the wFA to significantly change. The third scenario represent the case for which all three metrics are decreasing. The *Cerebellum X R* is concerned by this scenario. Finally, 11 other areas (7 cerebellar and 4 WM tracts) are additionally displayed because of their significant evolution in one of the three studied metrics. All those changes are displayed in Figures 5.19 and 5.20.

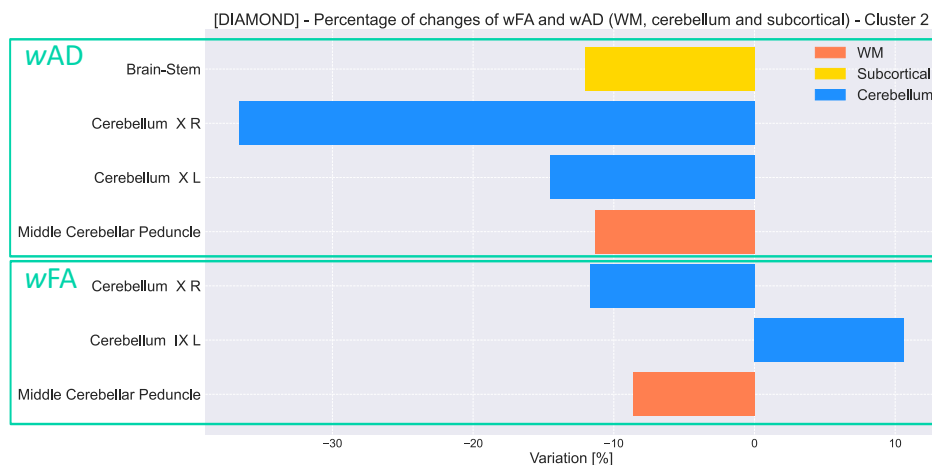


Figure 5.19: Summary of all regions significant wFA (bottom) and wAD (top) changes (WM, cerebellum and subcortical areas) considering cluster 2.

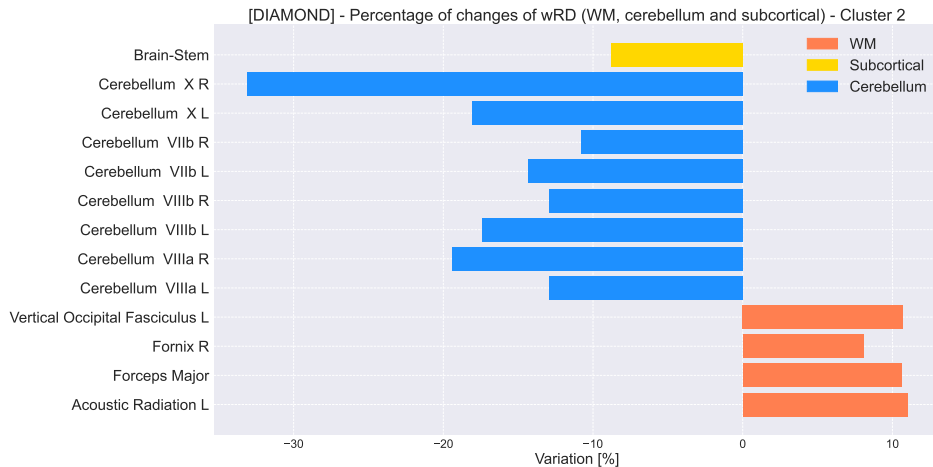


Figure 5.20: Summary of all regions significant *wRD* changes (WM, cerebellum and subcortical areas) considering cluster 2.

Cluster 1 & 2: `frac_csf`, `frac_ftot`

Two last metrics can be analysed in the case of the DIAMOND model to understand the variation of proportions between CSF and fibers inside specific ROIs. It appears that considering cluster 1, 4 cerebellar lobes show a decreasing `frac_csf` whereas nothing appears to be significant regarding `frac_ftot` as depicted on the bottom part of Figure 5.21. Similarly to cluster 1, 12 areas in cluster 2 are brought to the fore for their significant evolution of the CSF fraction but nothing appears to be remarkable when it comes to the fiber fraction (see the upper part of Figure 5.21).

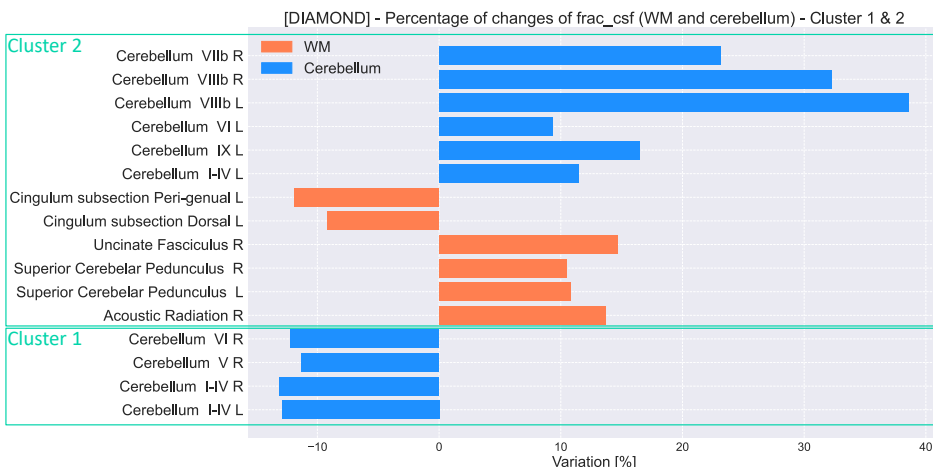


Figure 5.21: Summary of all regions showing significant `frac_csf` changes considering cluster 1 (bottom) and cluster 2 (top).

5.6 MF analysis

Thanks to the outputs of the ElikoPy pipeline and the new metrics created (`frac_ftot` & `wfvf`, explanations in section 4.4.7), several metrics can be separately analysed whereas the evolution of others can be compared. The analysis is also split in different categories, the WM tracts, the cerebellum and the subcortical regions.

Once again, the coherence of the MF metrics can be evaluated to make sure that the logical relationship between the CSF and the total fiber fractions is respected. This analysis can be found in appendix C.3.

Cluster 1

In cluster 1, all the areas presenting a significant evolution are located in the cerebellum and are characterised by a free water volume fraction reduction but no significant change appears for the fiber fraction. The corresponding graph (Figure 5.22 (bottom)) thus translates a slight decrease in the water content of 6 cerebellar subdivisions. The fiber proportion is therefore barely modified.

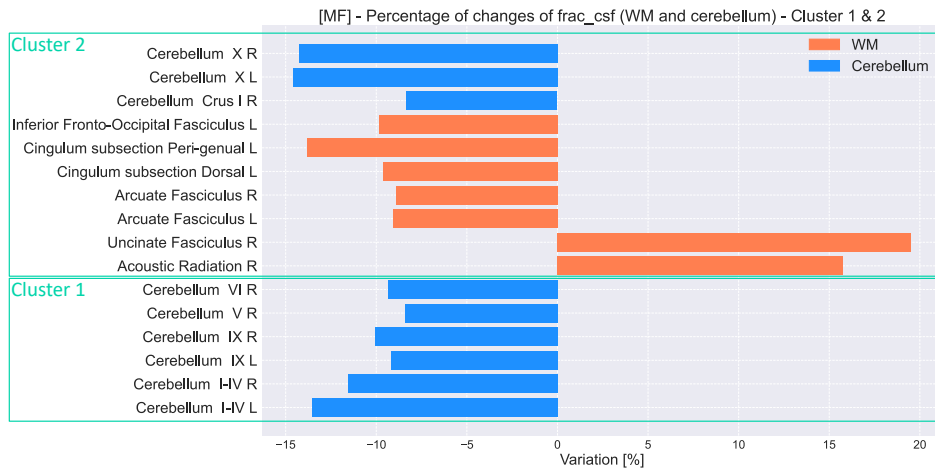


Figure 5.22: Summary of all regions showing significant `frac_csf` changes (WM and cerebellum) considering cluster 1 (bottom) and cluster 2 (top).

Cluster 2

In cluster 2, three different scenarios are appearing. First, 8 areas express a single metric change with no modification for the others. As shown in Figure 5.22 (top), the *Cerebellum Crus I R* as well as all the WM displayed show a variation in the CSF volume fraction, with no significant modification of the other MF metrics. Second, only two areas evolve according to a second scenario: the *Cerebellum X L* and *R*. They both show a reduced `frac_csf`, and an increase for `frac_ftot` and `fvf_tot` but no significant change in the fiber concentration `wfvf` as depicted in Figures 5.22 to 5.24.

Third, 5 areas located in the WM and 7 subcortical areas are representative of the last scenario as show Figure 5.23. Here, the general fiber and CSF fractions stay stable, but the total fiber volume fraction (`f vf_tot`) significantly increases, for a constant `wfvf`.

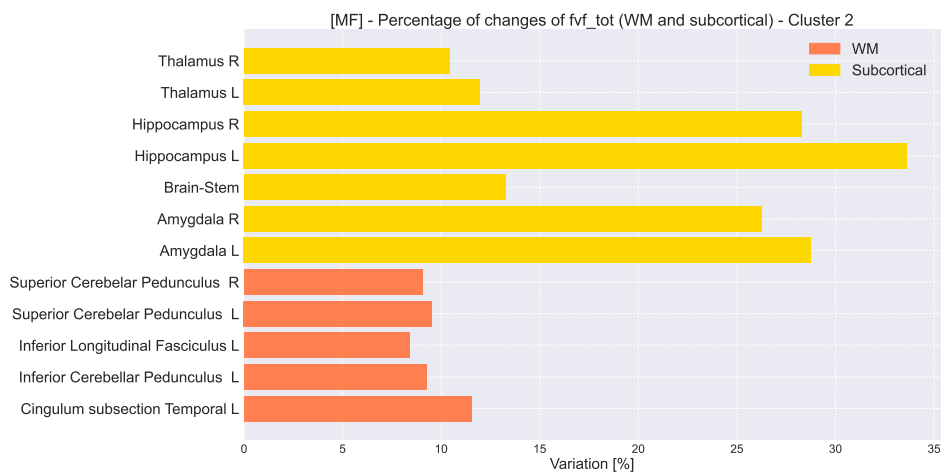


Figure 5.23: Summary of all regions showing significant `fvf_tot` changes (WM and subcortical areas) considering cluster 2.

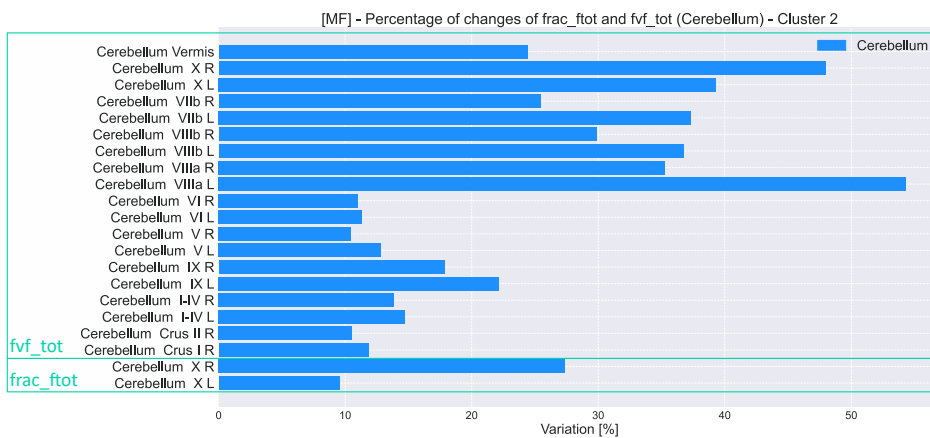


Figure 5.24: Summary of all regions showing significant `frac_ftot` and `fvf_tot` changes (cerebellum) considering cluster 2.

5.7 Volumetric changes in the three main brain compartments

Firstly, as the global volume of the brain cannot vary considerably, because of the physical restrictions imposed by the skull, one expects to see a compensation of the evolution of its different main compartments (i.e. the CSF, WM and GM). On the Figures 5.25 and 5.26, are displayed the volume differences between the two scans (T2-T1). Both graphs suggest that the fractions (%) of the three compartments compensate each other before and after abstinence, making the sum of all changes $((\text{frac}(T2)-\text{frac}(T1)) * 100$ null for all the subjects.

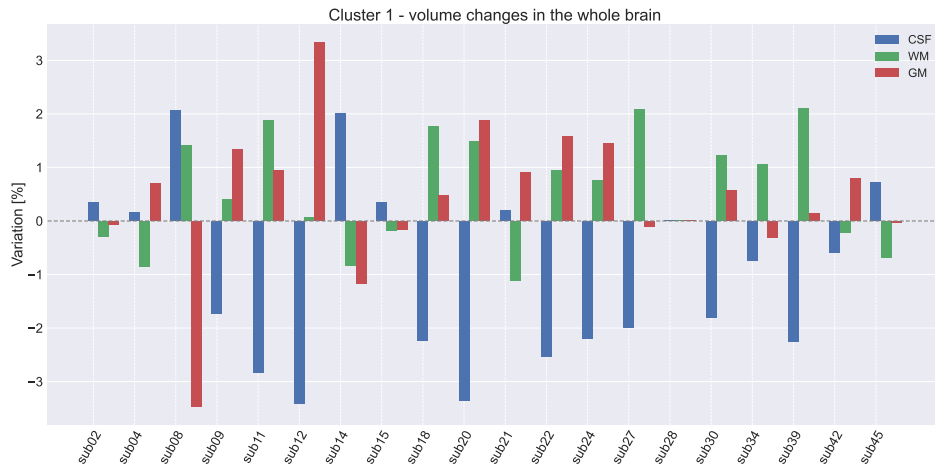


Figure 5.25: Overall volumetric changes (WM,GM,CSF) considering cluster 1.

To confirm this, the total volume variation $\text{diff}(\text{volume_tot}) = \text{diff}(\text{CSF}) + \text{diff}(\text{WM}) + \text{diff}(\text{GM})$ can be computed and then averaged over each cluster. From this, the value obtained defines the coherence of the evolution of the clusters. Indeed, if this value is very small, it means that the compartments for the patients inside the clusters compensate each other. For cluster 1 this value is $-2.9143 * 10^{-15}$ and for cluster 2 is $-3.4694 * 10^{-16}$, which absolutely confirms the consistency of the volumetric changes.

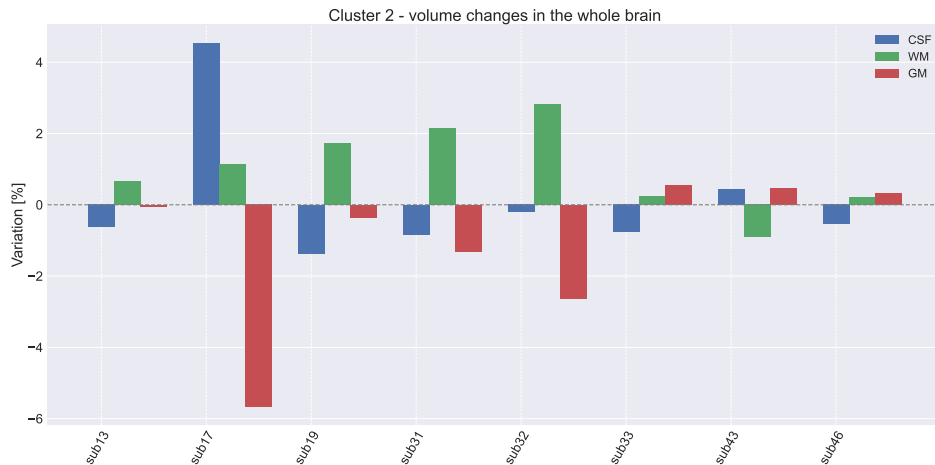


Figure 5.26: Overall volumetric changes (WM,GM,CSF) considering cluster 2.

Finally, we can have a closer look at the variations displayed in Figures 5.25 and 5.26 individually for the patients in the set. It can be noted that no significant

pattern can be observed for patients belonging to the same cluster so the volume changes are not representative of the behavior of a cluster. The values displayed are also relatively weak (with maximal values reaching 5%), which suggests that no remarkable volumetric changes did take place during abstinence. Those results differ from the one of Agartz et al. [78] and Shear et al. [79] who observed a progressive increase in the WM volume during short term abstinence.

The explanation for those volumetric is not trivial and has been subject to discussion in the literature. Agartz et al. [78] assumed that they are caused by the direct toxic effects of alcohol but that more research would be needed to identify the underlying physiological events of this brain volume restitution.

5.8 Conspicuous regions

By gathering all the results exposed from sections 5.3 to 5.6, one can note that several brain areas seem to have experienced more significant changes than others. As the analysis of 3 out of the 4 microstructural models developed in this thesis only focused on WM zones, the cerebellum and some subcortical structures, those are the ones that will be considered to highlight the conspicuous regions.

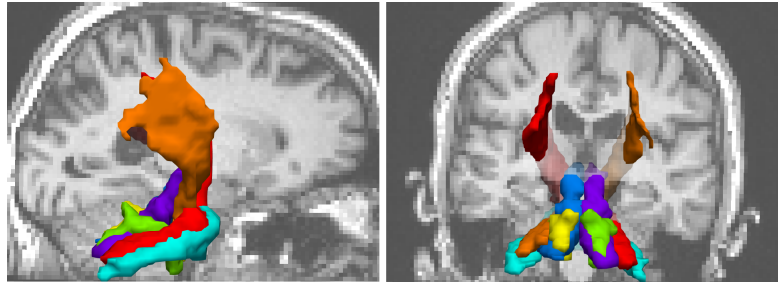
Those regions are selected according to the number of times they appear to be significant overall. However, for the metrics evolution described in the NODDI, DIAMOND and MF models (i.e. `fiso`, `fintra`, `fextra`, `frac_csf` and `frac_ftot`), when only one of the metrics demonstrates significant changes but that all the others do not, one can assume that this significant change is due to an initial very low fraction of the metric appearing as significant. This means that a slight change can appear as significant because it is computed as a percentage of change $((T2 - T1)/T1)$, whereas an initial higher fraction having an identical difference $(T2 - T1)$ does not identify the change as significant. The same remark can be made when only one out of the three metrics (i.e. FA, AD and RD) is changing for the DTI model. For this reason, the number of times each region is appearing as significant is only accounted, in the case of fraction metrics, when at least two of the fractions are significantly changing (or two DTI metrics), meaning that a real physiological reorganisation did indeed take place. Considering this, 28 regions are standing out by being affected by significant change of more than 4 different metrics¹⁰:

- Brain Stem,
- Amygdala L/R
- Cerebellum,
 - Crus I R,
 - Crus II R,
 - I-IV L/R,
 - IX L/R,
 - VIIIa L,
 - VIIib L/R,
 - VIIib R,
 - X L/R,
 - Vermis.
- Cortico Ponto Cerebellum L/R,
- Fornix L,
- Hippocampus L/R,

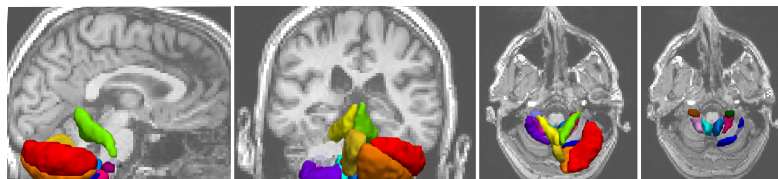
¹⁰The threshold of 4 significant changes has been set arbitrarily

- Inferior Cerebellar Pedunculus L/R,
- Middle Cerebellar Peduncle,
- Superior Cerebellar Pedunculus L/R,
- Thalamus L/R.

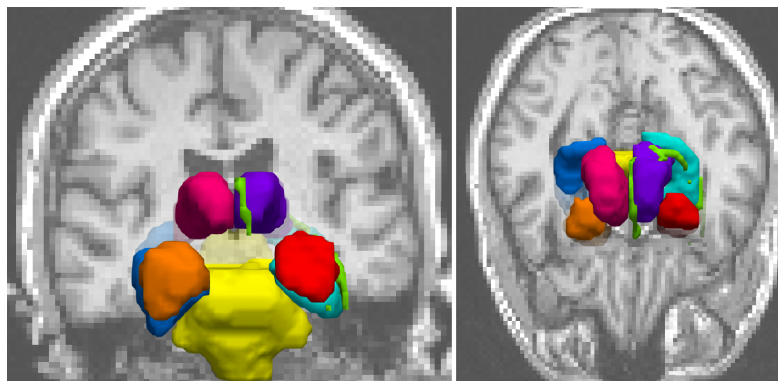
Those regions are the ones standing out and the focus will thus be put on them in section 6. They are also displayed on a 3D anatomic scan in Figures ?? ??.



(a) *Turquoise* : Middle Cerebellar Peduncle; *Red*: Cortico Ponto Cerebellum L; *Orange*: Cortico Ponto Cerebellum R; *Green*: Inferior Cerebellar Pedunculus R; *Yellow*: Inferior Cerebellar Pedunculus L; *Purple*: Superior Cerebellar Pedunculus R; *Blue*: Superior Cerebellar Pedunculus L.



(b) Cerebellum. *Light Green*: I-IV R; *Yellow*: I-IV L; *Gold*: Vermis; *Red*: Crus I R; *Orange*: Crus II R; *Purple*: VIIIa L; *Turquoise*: IX L; *Light blue*: IX R; *Dark pink*: VIIIb R; *Light pink*: VIIIb L; *Dark blue*: VIIb R; *Brown*: X L; *Dark green*: X R



(c) *Pink*: Thalamus R; *Purple*: Thalamus L; *Green*: Fornix L; *Turquoise*: Hippocampus L; *Blue*: Hippocampus R; *Orange*: Amygdala R; *Red*: Amygdala L; *Yellow*: Brain Stem

Figure 5.27: 3D view of the conspicuous regions.

Volume changes during abstinence of the conspicuous regions

Once the conspicuous zones have been identified, the potential volumetric evolution of those regions during abstinence raises a new field for analysis.

In the case of cluster 1, two areas (the *Cerebellum VIIb R* and *VIIIb R*) present significant volumetric variations (over 100%) that even had to be removed from the figure over 250% for clarity. For both areas, the median percentage change is very close to 0% but some extreme values appear for some of the patients in the cluster. Looking at the median of the other areas, the *Cerebellum Crus II R* is the only one showing a noticeable volumetric change with a 10% decrease whereas all the other medians are really close to zero.

Now talking about cluster 2, several areas show a significant volume increase higher than 8%: the *Hippocampus R/L*, *Amygdala L/R*, *Cerebellum Vermis* and *Cerebellum VIII b R/L*.

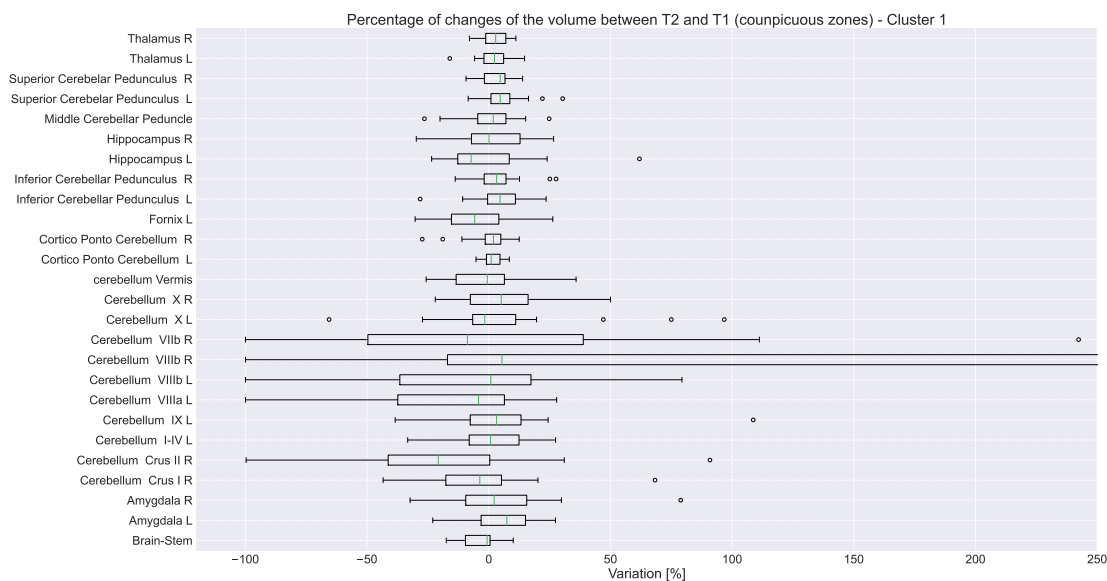


Figure 5.28: Local volumetric changes (conspicuous regions) - Cluster 1

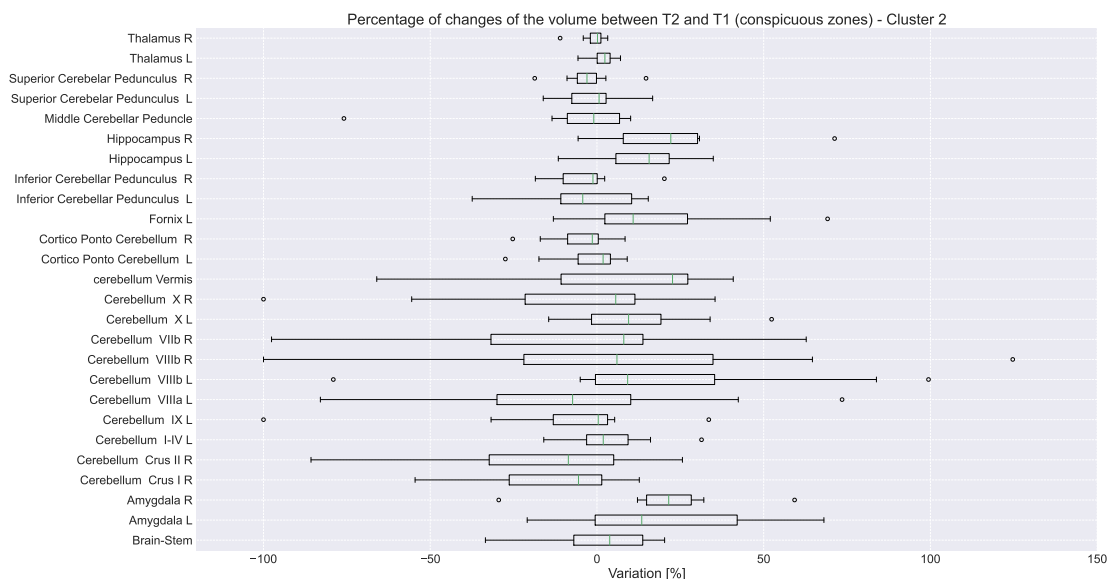


Figure 5.29: Local volumetric changes (conspicuous regions) - Cluster 2

5.9 Behavioral analysis

First of all, one can look at the alcohol consumption of each patient during the week before the start of the abstinence period. As depicted in the upper part of Figure 5.30, it is not possible to draw a conclusion about the behavior of the clusters with respect to this characteristic. Indeed, even if cluster 1 contains more patients than cluster 2, their respective alcohol consumption are not localised in a different and narrow range. This can be concluded by the distribution of the green and black curves: they both have similar heights at equivalent alcohol unit values, and their respective peaks appear at 9.2 and 10.3 units, which translates the similarity of the patterns.

Next, several other characteristics can be analysed and are depicted in the bottom part of Figure 5.30. The first one is the BDI, representing the degree of depression. It can be noted that the majority of the patients (24 out of the 28 belonging to cluster 1 and 2) improved their score between T1 and T2. Indeed, the negative value means that $T1 > T2$ and we can therefore interpret this as a decrease in their depression level after the 18 days of withdrawal. Among these 24 patients, 17 belong to cluster 1 and 7 to cluster 2 which represents 85 and 87.5 % of their total respectively. On the other hand, three patients have a T2 higher than T1 which indicates that they were more depressed than before abstinence. Finally, only one patient showed no change between the two tests. With those results, it cannot be said that one of the two clusters has a particular behavior but it can be concluded that in general, the level of depression of the patients decreased during their withdrawal.

Subsequently, we can look at the total OCDS. The latter is a combination of compulsion and obsession which represents craving. Once again, no particular pattern is evident for the two clusters. Considering cluster 1, only one patient is not improving his score. For all the others, their craving level seems to be enhanced. Now, for cluster 2, one patient's craving level increased and for the rest of this cluster, the score either stays stable or decreases. Thus, both clusters are showing an improvement of the craving (85 and 87.5 % of cluster 1 and 2 respectively).

The STAI is an indicator of anxiety and is depicted in Figure 5.30. Out of the 8 patients in cluster 2, 2 patients show more anxiety than before withdrawal, 4 show less anxiety and 2 shows no change. In cluster 1, 3 patients had a higher STAI at T2 than T1 thus illustrating an increase of their anxious feeling whereas the inverse situation is observable for 13 subjects, which is indicative of an amelioration of their anxiety level. Lastly, 4 patients shows no change between both tests. All in all, both clusters still have the same general development when taking into consideration the STAI: 50 and 65% of cluster 1 and cluster 2 respectively show an increase in this score.

Finally, the last characteristic that can be studied is the MFI (see Figure 5.30). The latter quantifies the level of fatigue. It seems that the clusters do not have a characteristic evolution when compared to each other. We can just note majority of patients in general, showing an improvement of their score and therefore having their fatigue level decreasing between the T1 and T2. This represents 85% of cluster 1 and 87.5% of cluster 2.

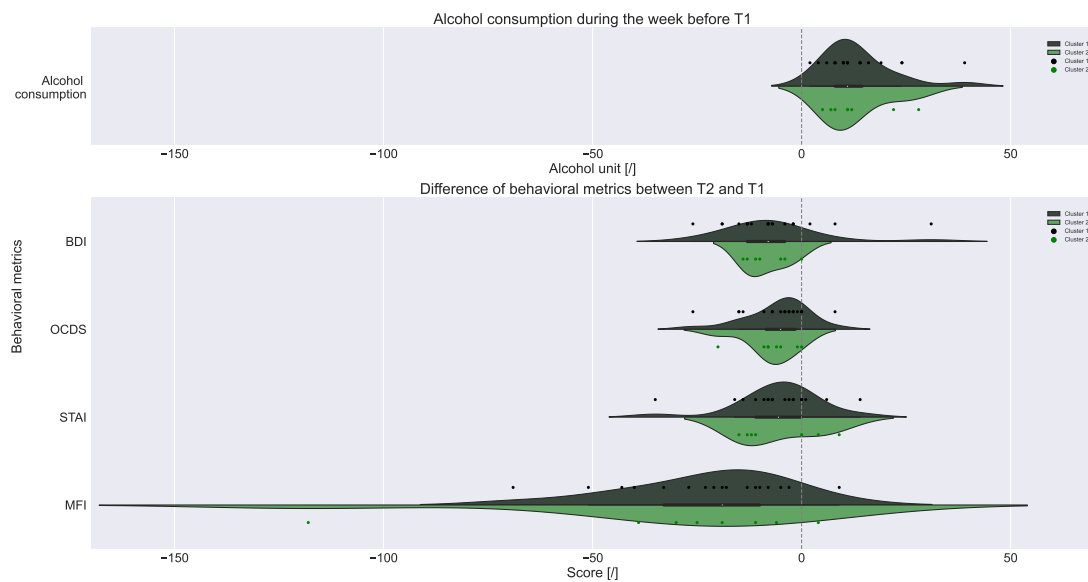


Figure 5.30: Evolution of the behavioral metrics for each cluster.

6 Discussion

This section consists in a critical analysis and interpretation of the results and the methods employed to obtain them. The potential inconsistencies in the results will also be discussed and some hypothesis will be posed to explain their presence.

6.1 Relevance of the different microstructural models

A coherence analysis has been performed in appendix C in order to highlight the coherence of diverse metrics when compared to metrics from other models. The same approach was adopted for metrics belonging to the same model (see appendices C.1 to C.3). These analyses allow the critical assessment of the validity of the models and the confidence in their outcomes.

First, the intra-model assessment, evaluating the consistency of the metrics inherent to a single model varied according to the model. Indeed, the NODDI and MF models proved a direct compensation of their different fractions over time (respectively: `fintra`, `fextra`, `fiso` and `frac_csf`, `frac_ftot`) whereas a first limitation of DIAMOND was introduced at this stage. The DIAMOND model did indeed not respect the rule that comes from the definition of the two fractions composing a voxel (`frac_csf` and `frac_ftot`): they must add up to one, and therefore, their evolutions must also compensate each other.

Then, the inter-model consistency assessment raised some new concerns about the DIAMOND model. As stated in appendix C, given the fact that DIAMOND and NODDI are both sensitive to fiber crossing and that they are able to discriminate the fibers from the CSF, `wFA` and `ODI` are supposed to have opposite tendencies in most of the cases. Yet, 5 out of the 37 (14%) significant brain regions analysed depicted in Figures C.9 and C.10 do not meet this expectation which, given the first imperfections in the DIAMOND model raised earlier, tends to either suggest an incoherence in DIAMOND model or a too high degree of liberty of the mathematical model.

Moreover, as already mentioned, the main drawback of the DTI model is its inability to discriminate crossing fiber populations, and to consequently mislead the results when this scenario appears inside a voxel/region. The impact of this limitation could be assessed by comparing two metrics built upon the same concept: `FA` and `wFA`. Indeed, as they both quantify the degree of anisotropy of the fibers inside a voxel, they should always either increase or decrease simultaneously. Hence, as it is the case for the 37 brain regions displayed in Figures C.9 and C.10, this suggests that the DTI and the DIAMOND models are consistent. But we can also observe that the values of the changes (T2-T1) of `FA` and `wFA` can be very different. In theory, the `wFA` has been created to overcome the limitation of fiber crossing observed in the computation of `FA` and is therefore more reliable. However, as the accuracy of the results coming out of DIAMOND has sometimes been questioned, one should stay critical regarding the evolution of its metrics, even if it is theoretically more accurate than the DTI model for instance.

6.2 Interpretation of the different metric variations

6.2.1 DTI

In the WM, the evolution of the three metrics of interest and their combinations enables to establish some hypotheses about the underlying physiological changes taking place in and around the axons. First, the FA is a primary indicator of axonal integrity and its augmentation therefore suggests a dense axonal packing whereas a decrease in FA is a sign of a loss of organised structure. Then, AD, directly linked to FA, can translate brain maturation when it increases for a certain period, while its decrease emphasizes axonal deletion, degeneration or injury in general. Finally, a decrease in RD can be caused by an increase in axonal density and a RD increase results from a potential myelin disruption [98]. When it comes to the GM, MD is an interesting metric, giving information about a potential inflammation process. Its increase can thus reflect an inflammation of the GM. In section 5.3, several combinations of metric evolution appear in several brain areas and translate different microstructural rearrangement.

First, a cerebellar lobule experienced an increase in FA and AD with no significant evolution regarding RD (see Figure 5.3). This reflects a probable maturation of the axons contained in the zone and therefore an improvement of axonal integrity for the WM parts of the lobe, thus improving the passage of nerve impulses. Considering the GM part of the lobe, it suggests an increase in the diffusivity of the water molecules as this situation induces an augmentation of MD, hypothetically sign of inflammation.

Second, other lobules showed a significant decrease in both diffusion metrics and a diminution in FA, suggesting that RD decreases more than the AD as explains Figure 6.1B. Biologically, this can be explained by an axonal degeneration or deletion and a denser axonal packing. Those changes are displayed in Figures 5.4 to 5.6. Similarly, other zones located in the cerebellum, WM tracts and subcortical structures show a decrease in both diffusion metrics but this time, with no noticeable change regarding FA, which means that an homogeneous decrease of AD and RD occurs as shows Figure 6.1C. This homogeneous diminution in both metrics also suggests a potential axonal degeneration with increased fiber density. Those changes are represented in Figures 5.5 to 5.8. Moreover, two WM zones are characterized by a decrease in all DTI metrics as shown in Figures 5.4 to 5.8. This combination suggests a stronger AD decline as depicted in the scenario of Figure 6.1A. This decrease in AD and RD in the three situations just introduced raises some questions, as axonal degeneration and packing do not intuitively take place at the same time. This could mean that the theoretical interpretation of the DTI metrics is reduced so simple cases but that particular situations can occur in which other phenomena take place. It is therefore important to note that many biological rearrangements and external contributors (fibers corrugation, fiber crossing, membrane permeability to water, internal axonal structure,...) can interfere with the logical interpretation of those simple metrics.

The last scenario concerns many brain areas for which only one of the analysed metrics shows a significant evolution. Usually, the changes are quite low and very close to the 8% threshold. This low value explains why the selection test could reject the significance of the other metrics, as they might for instance both decrease

from lower values and thus not exceed the threshold of 8% required to be considered as significant. This can be interpreted as an absence of considerable modification in the microstructure of these areas.

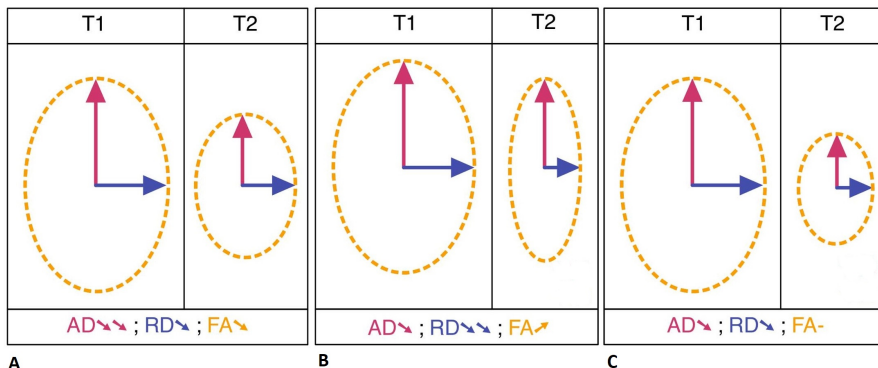


Figure 6.1: Possible evolutions between the different DTI metrics. **A:** FA decrease caused by a diffusion decrease with a stronger AD change; **B:** FA increase caused by a diffusion decrease with a stronger RD change; **C:** homogeneous decrease in AD and RD resulting in non noticeable change in FA.

6.2.2 NODDI

The NODDI model gives insights into the proportion of fibers, CSF and microglial cells occupying a specific brain area. The ODI metric is additionally analysed to give information about fiber dispersion. As detailed in section 5.4, many different combinations of those 4 metrics can be observed (see Figures 5.9 to 5.18).

First of all, if only one of the volume fraction (`fintra`, `fextra` or `fiso`) shows a significant evolution and that both others are stable, a reasonable conclusion can be made: no biological rearrangement is taking place. This means that one of the fraction might be changing because of its initial low value and that the others prove that nothing noticeable does in reality happen.

Then, by taking the basic definition of each fraction, an increase reasonably stands for an increased proportion of the compartment it represents, counterbalanced by a decrease in the volume of at least one of the other compartments. A change of `fintra` is thus the sign of axonal regrowth/regeneration, whereas `fextra` suggests a change in the amount of microglial cells such as the Schwann cells. Thus, a change in `fextra` can partly explain some changes in the integrity of the myelin sheath, as more Schwann cells might create more myelin to surround axons and therefore increase the speed of neural influx. Finally, the last compartment containing CSF can also vary in proportion, to potentially compensate the changes occurring in the two other compartments.

However, all metric combinations are not necessarily interpretable with some consistent biological modifications. For instance, some areas experience a simultaneous `fintra` increase and `fextra` decrease. Intuitively, having an increased proportion of fibers as a consequence of axonal regeneration, accompanied by a degradation in the myelin integrity suggested by the decreased volume of extracellular space does not fully make sense. This is where the inflammation hypothesis intervenes. An increase or decrease of one of the compartment does indeed not necessarily

translates an apparition or disappearance of the elements it is composed of. It might also be possible that an inflammatory process generates an increased volume of one of the compartment. The increased **fintra** of the previous example could therefore be caused by axonal swelling and not axonal regrowth, whereas the extra-axonal space could be compressed by this swelling or conversely in the case of an originally inflamed extra-axonal compartment that comes back to a «healthy state».

Finally, ODI also shows some variations during abstinence. When the latter increases in the WM, the fibers are supposed less dense after abstinence whereas in the GM, this can be the sign of an inflammation, a tissue rearrangement or a dendritic growth [28].

6.2.3 DIAMOND

wFA, wAD, wRD

From the 3 scenarios illustrated in Figure 6.2 that are taking place in the microstructure of some brain areas, some biological changes can be deduced and give an insight into the influence of abstinence.

The first scenario illustrated in Figure 6.2A is representative of a *wFA* and *wAD* decrease, with relatively stable *wRD*. Similarly to the interpretation of the DTI metrics, this is the sign of an axonal degeneration/injury. The second case, depicted by Figure 6.2B is characterised by a diminution of all three metrics, suggesting a stronger *wAD* decline. The third situation occurs when *wAD* and *wRD* decrease homogeneously, causing no change in *wFA* (see Figure 6.2C). Once again, those two last scenarios are relatively hard to understand at first sight, as axonal regeneration and fiber packing do not naturally come together but other unusual scenarios can be at the origin of such changes. To finish with the DIAMOND *weighted* metrics, several areas are characterized by a significant change in only one of them, translating an absence of real physiological change inside the brain in those areas, and a very light opposite evolution of at least one of the two metrics that have not been pinpointed. Those changes are all displayed in Figures 5.19 and 5.20.

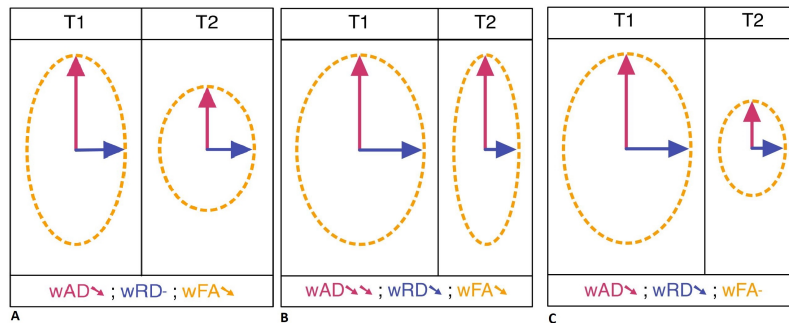


Figure 6.2: Possible evolutions between the different DTI metrics. **A:** FA decrease caused by a diffusion decrease with a stronger AD change; **B:** FA increase caused by a diffusion decrease with a stronger RD change; **C:** homogeneous decrease in AD and RD resulting in non noticeable change in FA.

frac_csf, frac_ftot

Similarly to **fiso** in the NODDI model, **frac_csf** quantifies the proportion of CSF inside an defined area (see Figure 5.21). As a complementary value, **frac_ftot**

reflects the total amount of fibers. It appears several times in section 5.5 that only `frac_csf` shows a significant evolution, in opposition to `frac_ftot` that never shows any significant change. This can be explained by an initial relatively small fraction of the CSF compartment, changing slightly in absolute proportion but importantly with respect to itself and the initial fraction occupied. For this reason, the other fraction is not spotted as changing significantly and we can conclude that no particular rearrangement occurred for the concerned zones.

6.2.4 MF

This time again for the MF microstructural model, 3 different scenarios are sufficient to illustrate the microstructural rearrangements taking place inside the brain.

The scenario n°1 is the one already introduced in the previous section: the only metric showing a significant change is the `frac_csf`. This is due to the fact that the initial CSF fraction is much lower than the fiber fraction. Moreover, as they both experience the same absolute change (more or less 2% as showed Figure C.7), the latter is proportionally higher in the case of the CSF, for which it can then exceed a threshold of 8%, whereas it stays weak for `frac_ftot`. The corresponding scenario is illustrated in the left part of Figure 6.3 ($T_2 \approx T_1$): the non significant change of the global fiber compartment causes some other variable to probably slightly increase but nothing strong enough to really be significant.

The scenario n°2 is the symbol of a decreasing `frac_csf`, increasing `frac_ftot` and `fvf_tot`, accompanied with a stable `wfvf`. This means that the fiber compartment is proportionally bigger after abstinence but that the concentration of fibers represented by `wfvf` does not increase. Equation 4.1 can explain this phenomenon: `fvf_tot` increases because of the increase of `f0` and `f1` (caused by the general `frac_ftot` increase and represented by the pink and yellow boxes respectively), but the axonal packing inside both fiber populations does not vary. This could suggest an actual inflammation of the fibers, causing the `frac_csf` decrease, as shown in the middle of Figure 6.3.

Finally, the scenario n°3 can be described by an increased `fvf_tot` with all other metrics keeping a stable value. As depicted in the right part of Figure 6.3, this can be caused by an increased number of fibers (axonal regrowth) in the fiber compartment. Thus, `wfvf` probably slightly increases but not enough to be significant.

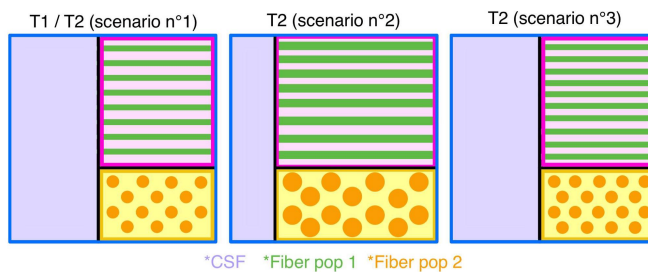


Figure 6.3: Different evolution in T_2 observed: scenario 1 characterises no noticeable change; scenario 2 represents reduced proportion of CSF with no significant change in the fiber concentration; scenario 3 illustrates a total fiber volume fraction increase but with no volume change for the general CSF and fiber fractions.

6.3 Conspicuous regions

From the list of noticeable areas detailed in section 5.8, 8 elements can be designated as structures mostly affected by short term abstinence: the brain stem, the amygdala, the cerebellum, the Cortico-Ponto Cerebellar (CPC) pathway, the fornix, the hippocampus, the cerebellar peduncles and the thalamus. They are thus going to be analysed separately in each cluster in order to draw conclusions about the microstructural changes they experienced. For this reason, as many cerebellar lobes are mentioned several times in the results, the cerebellum will be considered as a whole in the rest of this section and the changes will be considered to be global in this area.

As just said, it is interesting to focus on each cluster separately in order to retrieve the most accurate conclusion. These results will be discussed here below and are detailed in Figure 6.4.

Atlas	CLUSTER 1				CLUSTER 2											
	NODDI		DTI		MF		DIAMOND		NODDI		DTI					
	fextra	fiso	FA	AD	frac_csf	frac_ftot	wFA	wRD	wAD	fintra	fextra	fiso	ODI	FA	AD	RD
Brain Stem							-	-	+	-			+	-	-	-
Amygdala L								+	-		+	+	+	-	-	-
Amygdala R								-		+		+		-	-	-
Cerebellum Crus I R														+	-	-
Cerebellum Crus II R														+	-	-
Cerebellum I-IV L	+	-								-	+				-	-
Cerebellum I-IV R	+	-													-	-
Cerebellum IX L	+	-												+	-	-
Cerebellum IX R										-	+			-	-	-
Cerebellum VIIIa L							+	-					+	-	-	-
Cerebellum VIIIb L							+	-		+			+	-	-	-
Cerebellum VIIIb R							+	-		+			+	-	-	-
Cerebellum VIIb R							+	-					+	-	-	-
Cerebellum X L	+	+	-		+		-	-	+	-			+	-	-	-
Cerebellum X R					+		-	-	+				+	-	-	-
Cerebellum Vermis										-	+		+	-	-	-
Cortico Ponto Cerebellum L							+	-					+	-	-	-
Cortico Ponto Cerebellum R							+	-					+	-	-	-
Fornix L							+	-					+	-	-	-
Hippocampus L							+	-		+				-	-	-
Hippocampus R							+	-		+				-	-	-
Inferior Cerebellar Pedunculus L							+	-					+	-	-	-
Inferior Cerebellar Pedunculus R							+	-					+	-	-	-
Middle Cerebellar Peduncle					-		-	+	-				+	-	-	-
Superior Cerebellar Pedunculus L							+	-		+			+	-	-	-
Superior Cerebellar Pedunculus R							+	-		+			+	-	-	-
Thalamus L							+	-						-	-	-
Thalamus R							+	-		+				-	-	-

Figure 6.4: Summary of the metrics evolution in the conspicuous regions. The empty columns (metrics) have been removed from the table.

6.3.1 Noteworthy changes in Cluster 1

In the first cluster, three lobes of the cerebellum were mentioned for increased extracellular space compensated by a reduced fraction of CSF. This evolution in the cerebellum is accompanied by an increasing FA and AD pointed in another lobe by the DTI model. This sign of better axonal integrity is in line with the increase of **fextra**, resulting from a bigger amount of myelin around the axons. It can thus be concluded that the axon integrity improved during abstinence in some parts of the cerebellum for cluster 1 thanks to the myelin helping the transmission of neural influx.

To sum up, the amount of regions in which cluster 1 showed significant changes is limited, but the ones highlighted tend to show a recovery over time and thus a positive influence of abstinence.

6.3.2 Noteworthy changes in Cluster 2

As previously mentioned, cluster 2 is characterized by many more metric variations during abstinence than cluster 1. By analysing the table in Figure 6.4, one can easily spot a similar evolution of the metrics in all the conspicuous regions. Globally, the DTI demonstrates a decrease in both diffusion metrics, whereas the NODDI model suggests a decrease of the extra-axonal space, accompanied with an increase of the intracellular space as well as the free water volume. The dispersion of fibers also tends to globally increase. The DIAMOND and MF models show less changes but confirm this metric evolution for certain areas. Fortunately or not, the combination of these metrics can be interpreted in various ways. Indeed, one can reasonably assume that the microstructural integrity of the brain either goes towards a recovery state, or experience degradation but that both processes should not take place at the same time. For this reason, two main hypotheses come out of this combination of metrics.

First, the *positive hypothesis* would tend to suggest a promising evolution of the WM during abstinence. The decrease of both diffusion metrics could then be the sign of a global diffusion decline, that can be caused by a disinflammation of the zone if the latter was initially inflamed. Following this assumption, the reduction of **fextra** together with the increased **fintra** translate the deflation of the extra-axonal space, giving more space to the axons, thus increasing the volume of the intracellular compartment and giving more space for free water diffusion. The last remarkable change comes from the **ODI** increment, result of the lower constraints on the axons once the extracellular space inflammation shrunk.

Then, the *negative hypothesis* can rise from the exact same metric combination. From its common interpretation, the decrease of **AD** is a sign of axonal degeneration and the **RD** decline can potentially be caused by the appearance of lesions. Additionally, **fintra** can increase as a result of axonal inflammation, thus compressing the extracellular space and reducing its volume. The **ODI** measure can then increase because of the compromised directionality of the fiber due to the emerging inflammation.

To conclude, the abstinence process can have two opposite effects on the brain microstructure, depending on which one of the *positive* or *negative hypothesis* is adopted. The *negative hypothesis* suggests that abstinence does not have a real positive impact on the microstructure of the 8 patients belonging to cluster 2. This would be in line with the conclusion of De Santis et al. [5] who concluded that microstructural alterations caused by alcohol do not start to revert immediately after discontinuing alcohol consumption (see section 3.4). This also means that the considerable microstructural effect of abstinence might take place on a longer time-scale and that in the first weeks of abstinence, the long-term drinking history keeps damaging the condition of the patients in this cluster. By contrast, the *positive hypothesis* brings to a fully different conclusion. The latter leads to believe that the brain is initially subject to inflammation, especially in the extra-axonal

compartment (i.e. the microglial cells), and that abstinence reduces considerably this inflammation and gives more freedom to fibers configuration.

6.3.3 Respective volumes of the conspicuous regions

As already mentioned a few times in this paper, the volume of a zone can impact the results coming out of the analysis. This is why one must stay cautious about the interpretations of the results and take those volumes into consideration.

Indeed, as depicted in Figure 6.5, some of the regions are only represented by a few voxels in the brain. This is particularly the case of the cerebellar lobules for which the majority is composed of less than 500 voxels. Thus, if a small amount of pixels (e.g. 50) present outliers values for a specific metric, those smallest zones can be proportionally more impacted than bigger areas such as the brain stem. This is maybe one of the reason explaining why the cerebellum is coming out as a changing zone during abstinence. However, as the cerebellum is also enormously mentioned in the literature for its involvement in abstinence process, the changes are still expected to reflect a real reorganisation of the brain, but the values of percentage of change underlined might be impacted by the size of each zone.

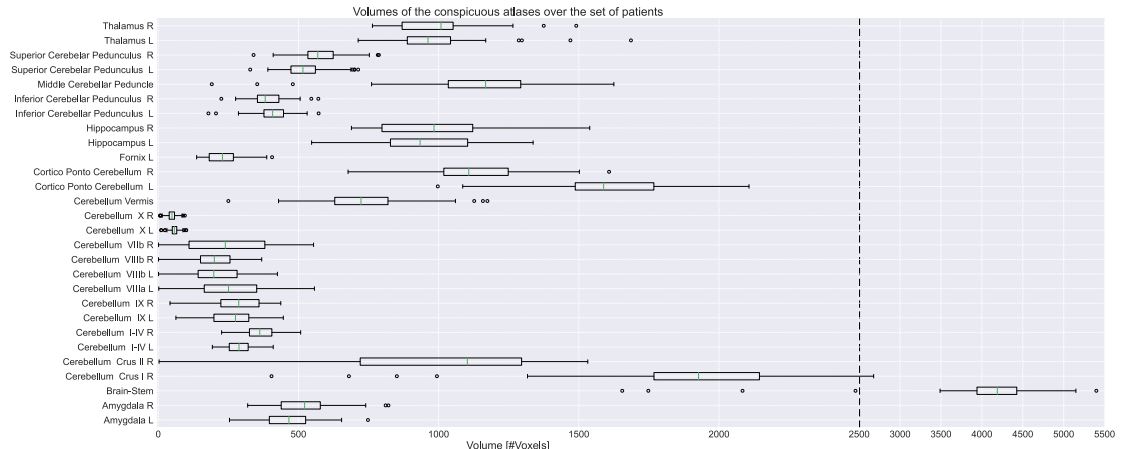


Figure 6.5: Boxplot representing the volume of the conspicuous regions in the patients' set. The right part of the figure, located after the black vertical line, is represented at another scale.

6.4 Resulting behavioral expectations

In the first place, the subcortical structures carry different roles inside the brain, and some were already introduced in section 3.3.1. The brain stem is the passage bloc between the brain and the spinal cord and helps for the coordination of basic body functions such as breathing, balance or heart rhythms [99]. However, it is also believed to play a role in the craving feeling in the case of AUD patients. The amygdala and the hippocampus have their main implications in emotion regulation, reward processing, spatial cognition, memory and decision making whereas the thalamus is involved in functions such as mood, memory, cognition, perception and finally relay of motor and sensory signals to the cerebellum [100]. There are thus many impairments that might appear during abstinence, if the integrity of those areas is not preserved which is presumably the case for the subjects belonging

to cluster 2 if the *negative hypothesis* is confirmed. On the assumption that the *positive hypothesis* would be the right one, those abilities would on the contrary be improved as a consequence of abstinence.

Then, as already introduced in section 3.3.1, the cerebellum plays a key role in the regulation of motor functions. On the one hand, cluster 1 shows some promising results for the motricity of the subjects composing it. Indeed, the increased number of microglial cells and the resulting improved myelination suggest that patients of cluster 1 should have retrieved better motor skills after withdrawal. On the other hand, cluster 2 can be affected by a deterioration or improvement of those skills depending on the hypothesis.

Furthermore, some studies tried to identify the role of the fibers connecting the cerebral cortex to the cerebellar cortex (see Figure 6.6): the CPC pathway. The fibers contained in the tract connect different parts of the brain together, but some more importantly than others. Indeed, the frontal lobe accounts for a major part (20%) of its fibers connections in the cerebral cortex. The existence of connections between the cerebellum and the parietal (9%), prefrontal (8%) and temporal cortex have also been proved for the CPC pathway. The modification of axon properties in this tract thus have implications mainly in cognitive processing but also in terms of spatial orientation, working memory, mental preparation for imminent actions [101]. Looking back at the results, this zone has not been particularly impacted by abstinence in cluster 1. By contrast, cluster 2 has demonstrated a similar evolution as the one in the cerebellum.

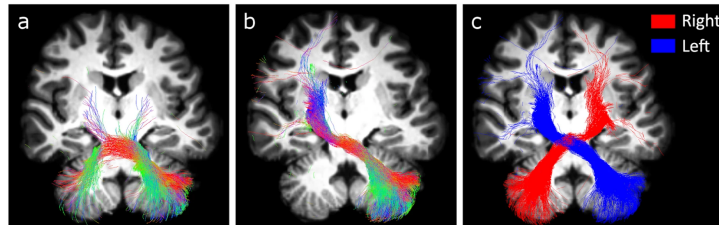


Figure 6.6: Reconstruction of the CPC pathway: 2D rendering of combined CSD technique and probabilistic streamlines tractography in a representative subject [101]

When it comes to the fornix, no specific function is directly associated to it but the latter is known to transmit information coming from the limbic system (composed for example from the hippocampus) to other structures. Concretely, the fornix has some indirect implications in the processes of recall memory and emotional memory. Moreover, as the limbic system is responsible spatial memory, learning, social processing,... the fornix assists them as just mentioned, and might compromise those functions when damaged [102]. The inflammation of the patients in cluster 2 in this zone might therefore be a cause for such consequences whereas the hypothesis of disinflammation suggests better abilities for those tasks.

Finally, the cerebellar peduncles contain the afferent and efferent tracts of the cerebellum. This means that compromising their integrity affects the transmission of motor information treated by the cerebellum whereas reinforcing it enables a better information flow.

6.5 Limitations

Despite the means put in place to characterize the microstructural changes taking place in the brain of 35 subjects suffering from AUD during short term abstinence, some limitations still exist and being aware of them is crucial for the interpretation of the results developed in section 5.

First, one cannot state that this study has been performed in a situation of complete abstinence for the entire set of patients. Indeed, some of them have consumed alcohol during the third week of abstinence when they were sent back home. This means that for some subjects, there has been an alcohol intake, in different quantities, a few days before the T2 scan.

Second, the clustering performed within the patient set can also be discussed. Indeed, it is not relevant to study the evolution of many metrics on 35 patients separately. However, the fact that a side cluster had to be defined in order to form two « real clusters », discards 7 subjects (20%) from the analysis. Moreover, the reason why they did not fit in any cluster is because of their *outlier* behavior. Hence, some of them might be representative of a significant recovery or degeneration of the brain in key areas affected by chronic alcohol consumption. Additionally, as explained in section 4, the metrics evolution on the entire set of atlases has been used to cluster the data. Perhaps, a prior selection targeting some specific areas reported as susceptible to changes in the case of AUD would have given a different and more relevant set of clusters. Finally, due to the limitations that each model brings into the analysis, some of the model contradict each other regarding specific changes, this can bring bias into the clusters as one of the observation might be erroneous. This is why it has been thought to build a different set of clusters for each microstructural model in order to maximize the relevance of the clusters and the similarity of the patients inside a same cluster. Nevertheless, this choice would have rendered the comparison of the different models less consistent and this stays one of the main goal of such a study. Therefore, the choice of building general clusters was kept.

Third, the atlas maps that are considered during this entire analysis have been registered from a standard MNI space to a space corresponding to each scan. This registration has shown to be imperfect in some of the brain areas. Notwithstanding, the considerable amount of regions and the big amount of patients renders the individual registration check very time consuming. Indeed, displaying 4725 (135*35) regions one by one to make sure that the registration has worked correctly and that each atlas map is well located would have taken a lot of time. But this limitation introduces some uncertainty about several brain regions, especially for the smallest ones that might therefore contain a higher fraction of voxels that should not, in reality, belong to them. This is why it is important to keep in mind that the registration is an automatic process that aims to adapt a general atlas map to every subject's brain. Nevertheless, the subjects considered in this study are not healthy controls but patients suffering from a condition highly affecting their brain at a micro and a macro-scale. Consequently, the exact delimitation of each zone might not be as precise as desired.

Moreover, the registration from the MNI space to T1 and T2 comes with a new limitation: the regions in both scans might not have the exact same size and be perfectly identical, which is totally normal considering the potential volumetric changes taking place in some regions of the brain. However, this has to be kept in mind in the analysis of the coherence between the different metrics (see appendix C). As shown in Figure 6.7, the pixels considered in T1 and on which an average percentage of change is computed are not exactly the same as the ones used for the same computation in T2, which justifies why averaging over two different regions does not always bring perfectly compensating results, and a error margin can be fully acceptable.

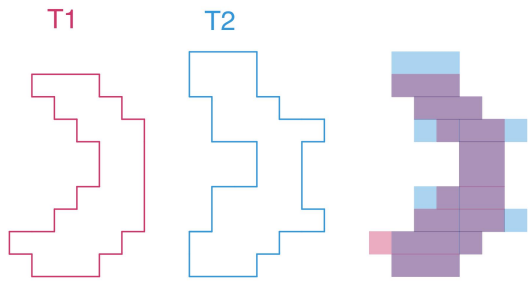


Figure 6.7: Illustration of the difference between a region in T1 & T2.

Fourth, as mentioned all along the report, a threshold has been set to 8% to discriminate real significant transformations from alterations due to randomness. Indeed, it has been explained that between two successive scans, some changes in the metrics usually appear due to slight motion in the MRI and other factors. This threshold has however been arbitrarily set and its relevance is therefore not ensured. Moreover, there is some uncertainty regarding the weak percentage of evolution, as even for changes exceeding 8%, the part of the change due to this randomness remains unknown.

Fifth, the MRI acquisition has some imperfections that must be mentioned. By displaying the different scans with a software such as MisterI [89] or MRIcron [83], it has been observed that a few slices are usually missing at the bottom of the brain. As a consequence, a part of the cerebellum is usually not taken into account as it is not part of the final file. Moreover, an acquisition default causes the first slices at the base of the skull to be incorrect, and only composed of a few pixels. For this reason, this slice was automatically cancelled (set to zero) to avoid the presence of incorrect data. However, the suppression of one additional slice avoids the consideration of valuable data that might be important, especially for the lobules VIIb, VIIIa and VIIIb (see Figure 4.3) that are located in this area. Indeed, as those volumes are already relatively small, missing a few pixels might have a big proportional impact.

Then, still considering the cerebellum, the analysis of every microstructural model has considered its entire structure all along the analysis, including its connected WM tracts such as the CPC pathway and the cerebellar peduncles but also the cerebellar lobes composed of both WM and GM. Those hybrid sub-divisions thus lead to less interpretable results as the nature of the cells inside those brain regions varies. To counter this limitation, a WM mask could have been applied on the lobes in order to consider the axons solely. However, the decision was made not to apply this mask because of the final volume that would have resulted from this operation. As explained earlier, the cerebellar lobules are already relatively small and the amount of voxels in each atlas map is initially a little bit critical, and shrinking them even more would lead to tiny volumes hard to analyse in a

meaningful way. Furthermore, it can be observed in Figure 4.12 that the WM mask provided by ElikoPy is not perfectly accurate. This is particularly obvious around the corpus callosum, as the WM mask actually goes beyond its delimitation and is composed of voxels located in the ventricles. Hence, one must stay cautious with the use of this WM mask.

Furthermore, it can be noted that the significant changes analysed were always expressed as a percentage of change, which helps to realise the proportional changes of the different metrics. However, some of the atlas maps considered in this study represent very small regions in the brain, thus sometimes only composed of a few pixels. The fact that some small volumes are also analysed has to be kept in mind, as a big variation in one voxel in such a zone might considerably influence the result of the entire area, whereas it would not have such an impact on a larger region. The choice of analysing the percentage of change along this thesis and not the absolute change (difference) is justified by the fact that no matter which metric is analysed, every result is expressed with the same unit (%) and is therefore comparable. But this choice also comes with some limitations, already expressed several time in the previous section (section 5: Results). Indeed, the situation in which one of the metric changes significantly (i.e. its percentage of change increases or decreases significantly according to the t-test with a mean absolute value higher than 8%), but no other metric of the concerned model show any significant changes occurs many times. As already said, this phenomenon might take place when an initially very small value experiences a slight change, that proportionally causes the metric to exceed the 8% threshold for change. As a result, this changes happens to be significant but does in reality not prove anything about a microstructural rearrangement. For instance, if the CSF volume fraction in a voxel increases from 3 to 6%, the value actually doubles and is thus significantly changing, but the fiber volume fraction, varying from 97 to 94% only experiences a 3.1% decrease which does not suggest any rearrangement.

Finally, the behavioral data analysed in section 5.9 are used to bring additional information about the mental state of the subjects and potentially link it to their microstructure evolutions. The results are however very dependent on the context in which the tests were performed. For instance, the fatigue level of a person might be highly influenced by AUD or by withdrawal symptoms, but it is also influenced by many other external factors such as recent events or even a bad night the day before. The anxiety score might as well differ a lot according to the moment at which it has been tested. Therefore, the variation of those scores can not be interpreted as solely coming from the evolution of the AUD pathology during abstinence and should perhaps be considered on a case by case basis.

6.6 Further perspectives

As just explained, many limitations still restrain the scope of this master's thesis. One of those limitations is of course the time, as additional analyses could have been conducted and others adjusted according to the results obtained. For this reason, there is undoubtedly more work to be done with those data to further analyse short term abstinence.

First and foremost, some functional data (fMRI) are also available for the same

set of patients. Treating them would add more insights into brain activity during specific tasks of interest and its evolution in the course of abstinence. Other data gathered by Mélissa Salavrakos are stool samples as it is believed that microbiota inflammation influences the inflammation state of the brain. Finding the correlation between both could help answering many questions about AUD and the physical effects of abstinence process. And with the results obtained in this study, this additional information would maybe be enough to pick between the *positive* and *negative hypothesis* that come out for cluster 2. As we are left with a big question mark about the nature of the evolution of this cluster, this could be a rapid way answer to it. Unfortunately, those samples have to be investigated by qualified doctors and the analysis has not started yet.

Moreover, being able to compare the data of AUD patients to the one of healthy controls could also give a new perspective to this work, by allowing to make a parallel with control values and estimate how far the metrics analysed in both T1 and T2 are from a control case.

Also, as several brain areas have been put forward in this work, it might be advisable to only consider those regions for the clustering of the patients to maybe obtain more realistic clusters. The clustering could therefore be performed once again, by only taking the conspicuous regions underlined in section 5.8 into consideration.

Furthermore, the microstructural models used in this work are relatively recent and the amount of studies exploring them in the literature stays low. This introduces a limitation for the interpretation of those metrics and the combinations that can be made between all the models, as they are not fully understood by the scientific community yet. It is therefore the diversity of researches that will be conducted in the future and considering those specific models that will enrich the general knowledge about their metrics and give certainties about the way to interpret them.

Finally, the big amount of results exposed is not always easy to summarize and to interpret. To have a bigger-scale impact, they could be outlined in a useful way. Indeed, the interest of this study is to identify the potential beneficial role of abstinence. And those results should not stay in the literature for scientific readers. They should be presented to people suffering from AUD to first convince them of the interest that withdrawal has for them and then to motivate them in this laborious experience and to prove them that they are doing the right thing by hanging on to sobriety. A project has been started during this master's thesis: a mobile application for doctors and AUD patients based on a daily follow up of the abstinence experience. The app intended to give daily advises to users and to link microstructural changes to effective enhancement of their capacities and improvement of their daily life. Due to a lack of time, this app only stayed at the stage of prototype. However, this could render this scientific discovery more concrete and have a real impact.

7 Conclusion

Identifying the short term impact of abstinence on the brain microstructure of AUD patients is at the center of many ongoing researches. This master's thesis has been undertaken to go further with those researches by analysing the brain in the framework of a very strict and rigorous protocol. The fact that every patient was scanned twice, at the exact same time interval and experienced an identical testing procedure adds a strong value to the data explored in comparison to other studies available in the literature.

To this aim, four microstructural models were used to quantify various parameters and highlight their changes over time: DTI, NODDI, DIAMOND and MF. Each model is built on different principles and theories, allowing to have diverse perspectives over the brain microstructure, and it is the combination of the information given by all those models that enables the formulation of hypotheses about the actual phenomenon taking place during abstinence. At first, the raw diffusion data acquired were pre-processed before applying the different microstructural models, both with help of the ElicoPy pipeline. Each metric, given as output of the microstructural models was then studied in terms of percentage of change during abstinence for each subject. It has been noticed at this point, that some divergences were present within the patient set and that different tendencies seemed to come out. For this reason, the patients were divided into three clusters, among which two were investigated in details.

The cluster 1 - composed of 20 subjects - was in the end, slightly impacted by the abstinence process but seemed to move towards an improvement of white matter integrity in the only outstanding area: the cerebellum. By contrast, the cluster 2 - composed of 8 subjects - demonstrated a lot more microstructural rearrangements in the course of the abstinence process. The most affected brain regions were the brain stem, the structures belonging to the limbic system (amygdala, fornix, hippocampus, thalamus), the cerebellum and its peduncles, and the cortico ponto cerebellar pathway. The tendency in all those areas was relatively similar: a decreased diffusion, an increased intracellular space, compensated by a decreased extracellular volume and a varying free water compartment, tending to usually increase. Finally, the fibers seemed to be more scattered after 18 days. From those evolution, two opposite hypotheses were put forward: a *positive* one stating that the brain was initially subject to inflammation and that abstinence reduces considerably this undesirable effect of alcohol, and a *negative* one suggesting that the impact of alcohol keeps damaging the microstructure and thus increases the inflammation state of the white matter, at least for the first couple weeks of alcohol cessation.

Concerning the metrics that revealed the majority of the information upon which the conclusions of this work are made, it seems that the DTI and the NODDI models are the most appropriate ones to characterise abstinence and spot the areas of interest. They are indeed the ones that demonstrated the most significant changes over time for their metrics.

Those conclusions have also been compared to the behavioral data assessing the level of fatigue, anxiety, craving (and others) of the different subjects, but no relationship between the microstructural clusters and the behavioral data could

be found. Nevertheless, the evolution of the behavioral scores suggests an overall recovery tendency for the patients, including therefore the ones belonging to cluster 2. For this reason, we would like to privilege the *positive hypothesis* that would be more in line with the behavioral data. It is however a personal assumption that has not been proven.

This work however presents some limitations. The clustering method could have been adapted by taking more relevant metrics and brain areas into account instead of the complete set of information at our disposal. One must also stay critical about the quality of the diffusion data as the acquisition contains several imperfections that cannot always be corrected. Finally, magnetic resonance imaging is a tool that has proven to be extremely useful to characterise the brain microstructure and the diffusion properties of its compartments. However, it is only by combining data from different sources and nature such as behavioral tests, blood samples, functional imaging, inflammation data and an entire set of biological markers, that those phenomena, mainly spotted with mathematical models will be given some sense and confirmed conclusions.

Nonetheless, the results of this study still give information about the brain areas prone to change when submitted to alcohol cessation and the potential underlying biological phenomena resulting from the variation of several metrics. This work thus opens the field for new researches as promising hypotheses have been set about the interest of abstinence.

References

- [1] Understanding Alcohol Use Disorder | National Institute on Alcohol Abuse and Alcoholism (NIAAA). <https://www.niaaa.nih.gov/publications/brochures-and-fact-sheets/understanding-alcohol-use-disorder>, last accessed on 2021-12-29.
- [2] Alcohol Abuse Statistics [2022]: National + State Data. <https://drugabusestatistics.org/alcohol-abuse-statistics/>, last accessed on 2022-12-29.
- [3] MRI online course (Magnetic Resonance Imaging). <https://www.imaios.com/en/e-Courses/e-MRI>, Last accessed on 2021-12-29.
- [4] Kastler Bruno. *Comprendre l'IRM : manuel d'auto-apprentissage / par B. Kastler,... D. Vetter,... ; [collab.] Z. Patay,... et P. Germain,... avec la participation de R. Allal, P. Anstett, S. Aubry... [et al.] préface du pr. Auguste Wackenheim.* Collection d'imagerie médicale diagnostic. Masson, Issy-les-Moulineaux, 6e édition entièrement révisée edition, DL 2006.
- [5] S. De Santis, P. Bach, L. Pérez-Cervera, A. Cosa-Linan, G. Weil, S. Vollstädt-Klein, D. Hermann, F. Kiefer, P. Kirsch, R. Ciccocioppo, W.H. Sommer, and S. Ca-nals. Microstructural white matter alterations in men with alcohol use disorder and rats with excessive alcohol consumption during early abstinence. *JAMA Psychiatry*, 76(7):749–758, 2019.
- [6] Sylvie Nozaradan Julie Duque, Laurence Dricot and Marcus Missal. Lgbio1115 - introduction aux neurosciences. <https://uclouvain.be/cours-2021-lgbio1115>.
- [7] D. Weishaupt, V. Kochli, B. Marincek, and E. Kim. How does mri work? an introduction to the physics and function of magnetic resonance imaging. *Journal of Nuclear Medicine - J NUCL MED*, 48:1910–1910, 11 2007.
- [8] Macq Benoît Kerckhofs Greet, Lee John and Peeters Frank. Lgbio2050 - medical imaging. <https://uclouvain.be/cours-2021-lgbio2050>.
- [9] Principles of diffusion imaging. <https://www.imaios.com/en/e-Courses/e-MRI/Diffusion-Tensor-Imaging/diffusion-principles>, last accessed on 2022-04-06.
- [10] Jeremy Jones. T1 relaxation time | Radiology Reference Article | Radiopaedia.org. <https://radiopaedia.org/articles/t1-relaxation-time?lang=us>, last accessed on 2022-04-11.
- [11] Usman Bashir. T2 relaxation | Radiology Reference Article | Radiopaedia.org. <https://radiopaedia.org/articles/t2-relaxation?lang=us>, last accessed on 2022-04-11.
- [12] Robert A. Pooley. Fundamental physics of MR imaging. *RadioGraphics*, 25(4):1087–1099.
- [13] Zach Drew. Magnetic field homogeneity | Radiology Reference Article | Radiopaedia.org. <https://radiopaedia.org/articles/magnetic-field-homogeneity?lang=us>, last accessed on 2022-04-11.

- [14] Wikipedia. Brownian motion, April 2022. https://en.wikipedia.org/w/index.php?title=Brownian_motion&oldid=1081772001, last accesed on 2022-04-11.
- [15] Principles of diffusion imaging. <https://www.imaios.com/en/e-Courses/e-MRI/Diffusion-Tensor-Imaging/diffusion-principles>, last accessed on 2022-04-12.
- [16] T.A.G.M. Huisman. Diffusion-weighted and diffusion tensor imaging of the brain, made easy. *Cancer Imaging*, 10(1):S163–S171.
- [17] J-Donald Tournier. Diffusion MRI in the brain – theory and concepts. *Progress in Nuclear Magnetic Resonance Spectroscopy*, 112-113:1–16.
- [18] Denis Le Bihan, Jean-François Mangin, Cyril Poupon, Chris A. Clark, Sabina Pappata, Nicolas Molko, and Hughes Chabriat. Diffusion tensor imaging: Concepts and applications. *Journal of Magnetic Resonance Imaging*, 13(4):534–546. <https://onlinelibrary.wiley.com/doi/10.1002/jmri.1076>.
- [19] Usman Bashir. Echo planar imaging | Radiology Reference Article | Radiopaedia.org. <https://radiopaedia.org/articles/echo-planar-imaging-1?lang=us>, last accessed on 2022-04-06.
- [20] Usman Bashir. Diffusion-weighted imaging | Radiology Reference Article | Radiopaedia.org. <https://radiopaedia.org/articles/diffusion-weighted-imaging-2?lang=us>, last accessed on 2022-04-12.
- [21] Susumu Mori and Jiangyang Zhang. Principles of diffusion tensor imaging and its applications to basic neuroscience research. *Neuron*, 51(5):527–539.
- [22] Yasmeen Ibrahim Elsayed Mabrouk, Rasha Elshafey, Wafik Elbahnasy, and Mahmoud ABD EL-AZIZ Dawoud. Early prediction of functional outcome after cerebral small arteries infarctions using diffusion tensor MRI tractography.
- [23] Diffusion tensor imaging: a practical handbook. OCLC: ocn935108978.
- [24] Lauren J. O'Donnell and Carl-Fredrik Westin. An introduction to diffusion tensor image analysis. *Neurosurgery Clinics of North America*, 22(2):185–196. <https://linkinghub.elsevier.com/retrieve/pii/S104236801000121X>.
- [25] Adolf Pfefferbaum, Margaret J Rosenbloom, Weiwei Chu, Stephanie A Sassenon, Torsten Rohlfing, Kilian M Pohl, Natalie M Zahr, and Edith V Sullivan. White matter microstructural recovery with abstinence and decline with relapse in alcohol dependence interacts with normal ageing: a controlled longitudinal dti study. *The Lancet Psychiatry*, 1(3):202–212, 2014.
- [26] Maxime Descoteaux. *High Angular Resolution Diffusion Imaging (HARDI)*, pages 1–25. John Wiley & Sons, Inc. <https://onlinelibrary.wiley.com/doi/10.1002/047134608X.W8258>.
- [27] Logan R. Ranzenberger and Travis Snyder. Diffusion tensor imaging. In *StatPearls*. StatPearls Publishing. <http://www.ncbi.nlm.nih.gov/books/NBK537361/>.

- [28] Kouhei Kamiya, Masaaki Hori, and Shigeki Aoki. NODDI in clinical research. *Journal of Neuroscience Methods*, 346:108908, December 2020.
- [29] Hui Zhang, Torben Schneider, Claudia A. M. Wheeler-Kingshott, and Daniel C. Alexander. Noddi: Practical in vivo neurite orientation dispersion and density imaging of the human brain. *NeuroImage*, 61:1000–1016, 2012.
- [30] Christian Beaulieu. The Biological Basis of Diffusion Anisotropy. In *Diffusion MRI*, pages 155–183. Elsevier, 2014.
- [31] Glia, December 2021. <https://en.wikipedia.org/w/index.php?title=Glia&oldid=1060484573>, last accessed on 2022-04-27.
- [32] Benoit Scherrer, Armin Schwartzman, Maxime Taquet, Mustafa Sahin, Sanjay P. Prabhu, and Simon K. Warfield. Characterizing brain tissue by assessment of the distribution of anisotropic microstructural environments in diffusion-compartment imaging (DIAMOND): Characterizing brain tissue with DIAMOND. *Magnetic Resonance in Medicine*, 76(3):963–977.
- [33] Gaëtan Rensonnet, Benoît Scherrer, Gabriel Girard, Aleksandar Jankovski, Simon K. Warfield, Benoît Macq, Jean-Philippe Thiran, and Maxime Taquet. Towards microstructure fingerprinting: Estimation of tissue properties from a dictionary of monte carlo diffusion MRI simulations. *NeuroImage*, 184:964–980. <https://linkinghub.elsevier.com/retrieve/pii/S1053811918319487>.
- [34] Stéfan van der Walt, Johannes L. Schönberger, Juan Nunez-Iglesias, François Boulogne, Joshua D. Warner, Neil Yager, Emmanuelle Gouillart, and Tony Yu. scikit-image: image processing in Python. *PeerJ*, 2:e453, June 2014.
- [35] Quentin Dessain. Elikopy. <https://github.com/Hyedrynn/ekopy>, last accessed on 2022-04-14.
- [36] Quentin Dessain and Mathieu Simon. Development of an image processing pipeline for large-scale in vivo population studies of the brain microstructure, 2021.
- [37] Eleftherios Garyfallidis, Matthew Brett, Bagrat Amirbekian, Ariel Rokem, Stefan Van Der Walt, Maxime Descoteaux, and Ian Nimmo-Smith. Dipy, a library for the analysis of diffusion MRI data. *Frontiers in Neuroinformatics*, 8, 2014.
- [38] Welcome to dmipy’s documentation! — dmipy 0.1 documentation. <https://dmipy.readthedocs.io/en/latest/>, last accessed on 2022-05-03.
- [39] DICOM. <https://www.dicomstandard.org>, lastaccessedon2022-04-12, language = en, urldate = 2022-04-12, journal = DICOM,.
- [40] Candace Makeda Moore. NIfTI (file format) | Radiology Reference Article | Radiopaedia.org. <https://radiopaedia.org/articles/nifti-file-format>, last accessed on 2022-04-12.
- [41] Usman Bashir. Gibbs and truncation artifacts | Radiology Reference Article | Radiopaedia.org. <https://radiopaedia.org/articles/gibbs-and-truncation-artifacts>, last accessed on 2022-05-01.

- [42] FSL. http://ftp.nmr.mgh.harvard.edu/pub/dist/freesurfer/tutorial_packages/OSX/fsl_501/doc/index.html, last accessed on 2022-05-12.
- [43] Jesper L.R. Andersson, Stefan Skare, and John Ashburner. How to correct susceptibility distortions in spin-echo echo-planar images: application to diffusion tensor imaging. *NeuroImage*, 20(2):870–888, October 2003.
- [44] Jesper L.R. Andersson and Stamatios N. Sotiroopoulos. An integrated approach to correction for off-resonance effects and subject movement in diffusion MR imaging. *NeuroImage*, 125:1063–1078, January 2016.
- [45] Hannah Ritchie and Max Roser. Alcohol consumption. *Our World in Data*, 2018. <https://ourworldindata.org/alcohol-consumption>.
- [46] K. Witkiewitz, R. Z. Litten, and L. Leggio. Advances in the science and treatment of alcohol use disorder. *Science Advances*, 5(9):eaax4043, 2019. <https://www.science.org/doi/abs/10.1126/sciadv.aax4043>.
- [47] Elisabeth A. Tawa, Samuel D. Hall, and Falk W. Lohoff. Overview of the Genetics of Alcohol Use Disorder. *Alcohol and Alcoholism*, 51(5):507–514, 09 2016.
- [48] Josef Frank, Sven Cichon, Jens Treutlein, Monika Ridinger, Manuel Mattheisen, Per Hoffmann, Stefan Herms, Norbert Wodarz, Michael Soyka, Peter Zill, Wolfgang Maier, Rainald Mössner, Wolfgang Gaebel, Norbert Dahmen, Norbert Scherbaum, Christine Schmäl, Michael Steffens, Susanne Lucae, Marcus Ising, Bertram Müller-Myhsok, Markus M. Nöthen, Karl F. Mann, Falk Kiefer, and Marcella Rietschel. Genome wide significant association between alcohol dependence and a variant in the adh gene cluster. *Addiction Biology*, 17, 2012.
- [49] Bela G Starkman, Amul J Sakharkar, and Subhash C Pandey. Epigenetics—beyond the genome in alcoholism. *Alcohol research : current reviews*, 34(3):293—305, 2012.
- [50] CDC. What is Epigenetics? | CDC, August 2020. <https://www.cdc.gov/genomics/disease/epigenetics.htm>, last accessed on 2022-03-07.
- [51] Epigenetics, April 2022. <https://en.wikipedia.org/w/index.php?title=Epigenetics&oldid=1082954034>, last accessed on 2022-03-07.
- [52] L.M. Kong, J.Y. Zeng, W.B. Zheng, Z.W. Shen, and R.H. Wu. Effects of acute alcohol consumption on the human brain: Diffusional kurtosis imaging and arterial spin-labeling study. *American Journal of Neuroradiology*, 40(4):641–647, 2019.
- [53] Neuroanatomy. <https://www.kenhub.com/en/library/anatomy/neuroanatomy>, last accessed on 2022-03-07.
- [54] Brain lobes neurology drawing image. <https://pixy.org/5870638/>, last accessed on 2022-05-28.
- [55] Cerebral cortex. <https://www.kenhub.com/en/library/anatomy/cerebral-cortex>, last accessed on 2022-03-07.

- [56] Mollie A. Monnig, Arvind Caprihan, Ronald A. Yeo, Charles Gasparovic, David A. Ruhl, Per Lysne, Michael P. Bogenschutz, Kent E. Hutchison, and Robert J. Thoma. Diffusion tensor imaging of white matter networks in individuals with current and remitted alcohol use disorders and comorbid conditions. *Psychology of Addictive Behaviors*, 27(2):455–465, June 2013.
- [57] M S Keshavan, V A Diwadkar, K Harenski, D R Rosenberg, J A Sweeney, and J W Pettegrew. Abnormalities of the corpus callosum in first episode, treatment naive schizophrenia. *Journal of Neurology, Neurosurgery & Psychiatry*, 72(6):757–760, 2002.
- [58] Lobes of the brain. <https://www.kenhub.com/en/library/anatomy/lobes-of-the-brain>, last accessed on 2022-04-27.
- [59] SpinalCord.com. Temporal Lobe: Function, Location, and Structure. <https://www.spinalcord.com/temporal-lobe>, last accessed on 2022-04-27.
- [60] Nervous system. <http://lindseyanatomy.weebly.com/nervous-system.html>, last accessed on 2022-03-07.
- [61] What Is the Role of the Hypothalamus? https://www.medicinenet.com/what_is_the_role_of_the_hypothalamus/article.htm, last accessed on 2022-04-27.
- [62] Thalamus | Definition, Anatomy, Function, & Disorders - Simply Psychology. <https://www.simplypsychology.org/thalamus.html>, last accessed on 2022-03-03.
- [63] Blausen com staff. Medical gallery of Blausen Medical 2014. *WikiJournal of Medicine*, 1(2), August 2014.
- [64] I.-Chao Liu, Chen-Huan Chiu, Chih-Jui Chen, Li-Wei Kuo, Yu-Chun Lo, and Wen-Yih Isaac Tseng. The microstructural integrity of the corpus callosum and associated impulsivity in alcohol dependence: a tractography-based segmentation study using diffusion spectrum imaging. *Psychiatry Research*, 184(2):128–134, November 2010.
- [65] Yajun Wang, Xiaohu Li, Cun Zhang, Haibao Wang, Zipeng Li, Jiajia Zhu, and Yongqiang Yu. Selective micro-structural integrity impairment of the isthmus subregion of the corpus callosum in alcohol-dependent males. *BMC psychiatry*, 19(1):96, March 2019.
- [66] Corpus callosum. <https://www.kenhub.com/en/library/anatomy/corpus-callosum>, last accessed on 2022-03-07.
- [67] Cerebellar degeneration. <https://www.kenhub.com/en/library/anatomy/cerebellar-degeneration>, last accessed on 2022-04-27.
- [68] Neurological Exam: Cerebellum: Anatomy. <https://lksom.temple.edu/neuroanatomy/lab/lesions/34.htm>, last accessed on 2022-05-17.
- [69] Mollie A. Monnig, Ronald A. Yeo, J. Scott Tonigan, Barbara S. McCrady, Robert J. Thoma, Amithrupa Sabbineni, and Kent E. Hutchison. Associations of White Matter Microstructure with Clinical and Demographic Characteristics in Heavy Drinkers. *PloS One*, 10(11):e0142042, 2015.

- [70] Evgeny J Chumin, Gregory G Grecco, Mario Dzemidzic, Hu Cheng, Peter Finn, Olaf Sporns, Sharlene D Newman, and Karmen K Yoder. Alterations in white matter microstructure and connectivity in young adults with alcohol use disorder. *Alcoholism, clinical and experimental research*, 43(6):1170–1179, June 2019.
- [71] Adolf Pfefferbaum, Elfar Adalsteinsson, and Edith V. Sullivan. Dysmorphology and microstructural degradation of the corpus callosum: Interaction of age and alcoholism. *Neurobiology of Aging*, 27(7):994–1009, July 2006.
- [72] Yukai Zou, Donna E. Murray, Timothy C. Durazzo, Thomas P. Schmidt, Troy A. Murray, and Dieter J. Meyerhoff. Effects of abstinence and chronic cigarette smoking on white matter microstructure in alcohol dependence: Diffusion tensor imaging at 4t. *Drug and Alcohol Dependence*, 175:42–50, 2017.
- [73] Margaret Rosenbloom, Edith V. Sullivan, and Adolf Pfefferbaum. Using magnetic resonance imaging and diffusion tensor imaging to assess brain damage in alcoholics. *Alcohol Research & Health: The Journal of the National Institute on Alcohol Abuse and Alcoholism*, 27(2):146–152, 2003.
- [74] Omar M. Alhassoon, Scott F. Sorg, Michael J. Taylor, Rick A. Stephan, Brian C. Schweinsburg, Nikki H. Stricker, Assawin Gongvatana, and Igor Grant. Callosal white matter microstructural recovery in abstinent alcoholics: A longitudinal diffusion tensor imaging study. *Alcoholism: Clinical and Experimental Research*, 36(11):1922–1931, 2012.
- [75] B. Rolland, L. Dricot, C. Creupelandt, P. Maurage, and P. De Timary. Respective influence of current alcohol consumption and duration of heavy drinking on brain morphological alterations in alcohol use disorder. *Addiction Biology*, 25(2), 2020. cited By 7.
- [76] Nabi Zorlu, Tugba Karavul Uzman, Fazil Gelal, Cigdem Colak Kalayci, Serap Polat, Aybala Saricicek, Pelin Kurtgöz Zorlu, and Seref Gulseren. Abnormal white matter integrity in long-term abstinent alcohol dependent patients. *Psychiatry Research: Neuroimaging*, 224(1):42–48, 2014.
- [77] Xiaowei Zou, Timothy C. Durazzo, and Dieter J. Meyerhoff. Regional Brain Volume Changes in Alcohol-Dependent Individuals During Short-Term and Long-Term Abstinence. *Alcoholism: Clinical and Experimental Research*, 42(6):1062–1072, June 2018.
- [78] I. Agartz, S. Brag, J. Franck, A. Hammarberg, G. Okugawa, K. Svinhufvud, and H. Bergman. MR VOLUMETRY DURING ACUTE ALCOHOL WITHDRAWAL AND ABSTINENCE: A DESCRIPTIVE STUDY. *Alcohol and Alcoholism*, 38(1):71–78, January 2003.
- [79] Paula K. Shear, Terry L. Jernigan, and Nelson Butters. Volumetric Magnetic Resonance Imaging Quantification of Longitudinal Brain Changes in Abstinent Alcoholics. *Alcoholism: Clinical and Experimental Research*, 18(1):172–176, February 1994.

- [80] Margaret J. Rosenbloom, Adolf Pfefferbaum, and Edith V. Sullivan. Recovery of Short-Term Memory and Psychomotor Speed but Not Postural Stability With Long-Term Sobriety in Alcoholic Women. *Neuropsychology*, 18(3):589–597, July 2004.
- [81] Beck’s Depression Inventory - Take Beck’s Depression Test Online. <https://psycho-tests.com/test/becks-depression-inventory>, last accessed on 2022-04-12.
- [82] State-Trait Anxiety Inventory (STAI). <https://www.statisticssolutions.com/free-resources/directory-of-survey-instruments/state-trait-anxiety-inventory-stai/>, last accessed on 2022-04-12.
- [83] NITRC: MRIcron: Tool/Resource Info. <https://www.nitrc.org/projects/mricron>, 2022-05-04.
- [84] Atlases. <https://ebrains.eu/services/atlas>, last accessed on 2022-04-13.
- [85] Jörn Diedrichsen, Joshua H. Balsters, Jonathan Flavell, Emma Cussans, and Narender Ramnani. A probabilistic mr atlas of the human cerebellum. *NeuroImage*, 46(1):39–46, 2009.
- [86] ATLAS MAPS. <https://www.natbrainlab.co.uk/atlas-maps>, last accessed on 2022-04-02.
- [87] FSL. Atlases. <https://fsl.fmrib.ox.ac.uk/fsl/fslwiki/Atlases>, last accessed on 2022-04-02.
- [88] Shaun Warrington, Katherine L. Bryant, Alexandre Khrapitchev, Jerome Sallet, Marina Charquero-Ballester, Gwenaëlle Douaud, Saad Jbabdi, Roger B. Mars, and Stamatis N. Sotiroopoulos. Xtract - standardised protocols for automated tractography in the human and macaque brain. *NeuroImage*, 217:116923, 2020.
- [89] MisterI. <http://www.benoitscherrer.com/MisterI/>, last accessed on 2022-05-17.
- [90] Sabine Hofer and Jens Frahm. Topography of the human corpus callosum revisited—Comprehensive fiber tractography using diffusion tensor magnetic resonance imaging. *NeuroImage*, 32(3):989–994, September 2006.
- [91] About the MNI space(s) – Lead-DBS. <https://www.lead-dbs.org/about-the-mni-spaces/>, last accessed on 2022-04-02.
- [92] Diffeomorphism, January 2022. <https://en.wikipedia.org/w/index.php?title=Diffeomorphism&oldid=1068397061>, last accessed on 2022-03-24.
- [93] DIPY - Tutorials. <https://dipy.org/>, last accessed on 2022-03-24.
- [94] *k*-means clustering, April 2022. https://en.wikipedia.org/w/index.php?title=K-means_clustering&oldid=1084651831, last accessed on 2022-04-12.
- [95] sklearn.cluster.KMeans. <https://scikit-learn/stable/modules/generated/sklearn.cluster.KMeans.html>, 2022-05-06.

- [96] sklearn.cluster.AffinityPropagation. <https://scikit-learn/stable/modules/generated/sklearn.cluster.AffinityPropagation.html>, last accessed on 2022-05-08.
- [97] Alcohol change UK. Alcohol units. <https://alcoholchange.org.uk/alcohol-facts/interactive-tools/check-your-drinking/alcohol-units>, last accessed on 2022-04-14.
- [98] Do Tromp. Dti scalars (fa, md, ad, rd) - how do they relate to brain structure? *The Winnower*, 04 2016.
- [99] Brainstem: Overview, Function & Anatomy. <https://my.clevelandclinic.org/health/body/21598-brainstem>, last accessed on 2022-05-20.
- [100] Amygdala Function and Location | Simply Psychology. <https://www.simplypsychology.org/amygdala.html>, last accessed on 2022-05-20.
- [101] Fulvia Palesi, Andrea De Rinaldis, Gloria Castellazzi, Fernando Calamante, Nils Muhlert, Declan Chard, J. Donald Tournier, Giovanni Magenes, Egidio D'Angelo, and Claudia A. M. Gandini Wheeler-Kingshott. Contralateral cortico-ponto-cerebellar pathways reconstruction in humans *in vivo*: implications for reciprocal cerebro-cerebellar structural connectivity in motor and non-motor areas. *Scientific Reports*, 7(1):12841, October 2017.
- [102] Fornix | Structure, Function, Connections, Role & Summary. <https://human-memory.net/fornix/>, last accessed on 2022-05-19.

Appendix

A MRI parameters: typical .json file

```
{ "Modality": "MR",
  "MagneticFieldStrength": 3,
  "ImagingFrequency": 127.77,
  "Manufacturer": "GE",
  "ManufacturersModelName": "SIGNA_Premier",
  "InstitutionName": "UCL",
  "DeviceSerialNumber": "000000210036MR03",
  "StationName": "GEHC",
  "BodyPartExamined": "BRAIN",
  "PatientPosition": "HFS",
  "SoftwareVersions":
    "28_LX_MR_Software_release:RX28.0_R04_2020.b",
  "MRAcquisitionType": "2D",
  "SeriesDescription": "Opt_DTI_4B_64_32_HB3",
  "ProtocolName": "Opt_DTI_4B_64_32_HB3",
  "ScanningSequence": "EP_SE",
  "SequenceVariant": "NONE",
  "ScanOptions": "CL_GEMS_SAT_GEMS_EDR_GEMS_EPI_GEMS_
HYPERBAND_GEMS_ACC_GEMS_PFF_FS",
  "ImageType": ["ORIGINAL", "PRIMARY", "OTHER"],
  "SeriesNumber": 5,
  "AcquisitionTime": "14:05:11.000000",
  "AcquisitionNumber": 1,
  "SliceThickness": 2,
  "SpacingBetweenSlices": 2,
  "SAR": 0.149468,
  "EchoTime": 0.0793,
  "RepetitionTime": 4.837,
  "FlipAngle": 90,
  "PhaseEncodingPolarityGE": "Unflipped",
  "CoilString": "48HAP",
  "PercentPhaseFOV": 100,
  "AcquisitionMatrixPE": 110,
  "ReconMatrixPE": 110,
  "EffectiveEchoSpacing": 0.000692,
  "TotalReadoutTime": 0.075428,
  "PixelBandwidth": 4545.45,
  "PhaseEncodingDirection": "j-",
  "ImageOrientationPatientDICOM": [ 0.999947, 0.00473293, 0.00919025,
-0.00390882, 0.996139, -0.0877037 ],
  "InPlanePhaseEncodingDirectionDICOM": "COL",
  "ConversionSoftware": "dcm2niix",
  "ConversionSoftwareVersion": "v1.0.20190902" }
```

B Atlases

WM tracts

- Association fibers:
 - Arcuate Fasciculus (L/R)
 - Frontal Aslant Tract (L/R)
 - Inferior Longitudinal Fasciculus (L/R)
 - Inferior Fronto-Occipital Fasciculus (L/R)
 - Middle Longitudinal Fasciculus (L/R)
 - Superior Longitudinal Fasciculus I (L/R)
 - Superior Longitudinal Fasciculus II (L/R)
 - Superior Longitudinal Fasciculus III (L/R)
 - Uncinate Fasciculus (L/R)
 - Vertical Occipital Fasciculus (L/R)
- Commissural fibers:
 - Anterior Commissure
 - Forceps Major
 - Forceps Minor
 - Middle Cerebellar Peduncle
- Limbic fibers:
 - Cingulum subsection: Dorsal (L/R)
 - Cingulum subsection: Peri-genual (L/R)
 - Cingulum subsection: Temporal (L/R)
 - Fornix (L/R)
- Projection fibers:
 - Acoustic Radiation (L/R)
 - Anterior Thalamic Radiation (L/R)
 - Corticospinal Tract (L/R)
 - Optic Radiation (L/R)
 - Superior Thalamic Radiation (L/R)

Corpus Callosum

- | | |
|--|---|
| <ul style="list-style-type: none"> • Corpus Callosum • Anterior Body • Posterior Body | <ul style="list-style-type: none"> • Genu • Isthmus • Splenium |
|--|---|

Cerebellum

- | | |
|---|---|
| <ul style="list-style-type: none"> • Crus I (L/R) • Crus II (L/R) • Lobules I-IV (L/R) • Lobule V (L/R) • Lobule VI (L/R) • Lobule VIIb (L/R) | <ul style="list-style-type: none"> • Lobule VIIIa (L/R) • Lobule VIIIb (L/R) • Lobule IX (L/R) • Lobule X (L/R) • Vermis |
|---|---|

Cerebellar (cerebellum WM)

- Cerebellar peduncles

- Inferior Cerebellar Pedunculus (L/R)
- Superior Cerebellar Pedunculus (L/R)
- Cortico-Ponto pathways
 - Cortico-ponto Cerebellar tract (L/R)

Cortex

- Angular gyrus
- Central Opercular cortex
- Cingulate gyrus anterior
- Cingulate Gyrus posterior
- Cuneal Cortex
- Frontal Medial Cortex
- Frontal Operculum Cortex
- Frontal Orbital Cortex
- Frontal Pole
- Heschl Gyrus
- Inferior Frontal Gyrus pars opercularis
- Inferior Frontal Gyrus pars triangularis
- Inferior Temporal Gyrus anterior
- Inferior Temporal Gyrus posterior
- Inferior Temporal Gyrus temporooccipital part
- Insular Cortex
- Intracalcarine Cortex
- Juxtapositional Lobule Cortex
- Lateral Occipital Cortex inferior
- Lateral Occipital Cortex superior
- Lingual Gyrus
- Middle Frontal Gyrus
- Middle Temporal Gyrus anterior
- Middle Temporal Gyrus posterior
- Middle Temporal Gyrus tem-
- Middle Temporal Gyrus temporooccipital part
- Occipital Fusiform Gyrus
- Occipital Pole
- Paracingulate Gyrus
- Parahippocampal Gyrus anterior
- Parahippocampal Gyrus posterior
- Parietal Operculum Cortex
- Planum Polare
- Planum Temporale
- Postcentral Gyrus
- Precentral Gyrus
- Precuneous Cortex
- Subcallosal Cortex
- Superior Frontal Gyrus
- Superior Parietal Lobule
- Superior Temporal Gyrus anterior
- Superior Temporal Gyrus posterior
- Suprocalcarine Cortex
- Supramarginal Gyrus anterior
- Supramarginal Gyrus posterior
- Temporal Fusiform Cortex anterior
- Temporal Fusiform Cortex posterior
- Temporal Occipital Fusiform Cortex
- Temporal Pole

Subcortical

- Brain Stem
- Amygdala (L/R)
- Caudate (L/R)
- Cerebral White Matter (L/R)
- Hippocampus (L/R)
- Putamen (L/R)
- Thalamus (L/R)

Lobes

- Frontal lobe
- Insula
- Occipital lobe
- Parietal lobe
- Temporal lobe

C Coherence of the microstructural models

C.1 NODDI: Coherence of fintra, fextra and fiso

As those metrics (`fintra`, `fextra` and `fiso`) are fractions, their sum must be equal to one inside a voxel:

$$\begin{cases} \text{fintra}(T1) + \text{fextra}(T1) + \text{fiso}(T1) = 1 \\ \text{fintra}(T2) + \text{fextra}(T2) + \text{fiso}(T2) = 1 \end{cases}$$

$$\Rightarrow (\text{fintra}(T2) - \text{fintra}(T1)) * 100 + (\text{fextra}(T2) - \text{fextra}(T1)) * 100 + (\text{fiso}(T2) - \text{fiso}(T1)) * 100 = 0 \quad (\text{C.1})$$

Indeed, their respective evolutions cannot all be positive or negative, they must compensate each other as states equation C.1. For example, an increase of `fintra` in one area must be compensated by a decrease in at least one for the other metrics, in the same area.

Secondly, the mean difference ($T2 - T1$)¹¹ of each metric was analysed as an average between all the subjects inside a cluster. These differences for cluster 1 are shown in Figure C.1 and only the areas with at least a significant change in one of three metrics are displayed. It can be seen that the different sticks (blue, green and red) for the same area do not evolve in the same direction. Hence, if the different sticks are summed up, one can obtain an average value of $1.382 * 10^{-6}$ for cluster 1 and $-7.76 * 10^{-6}$ for cluster 2. This shows that the model is consistent. The coherence for cluster 2 are depicted in Figures C.2 and C.3.

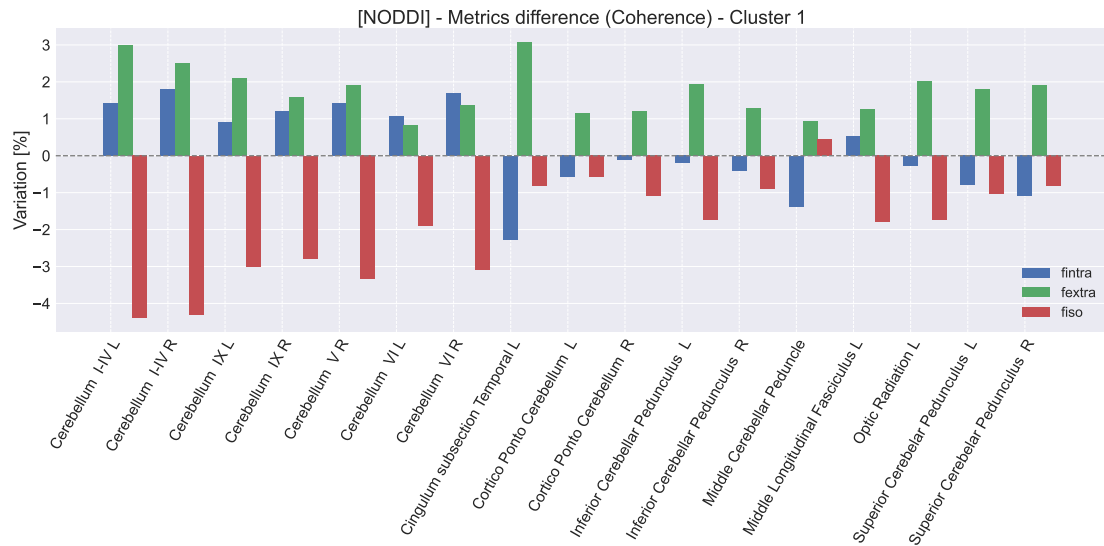


Figure C.1: Coherence of the NODDI model considering cluster 1 - summary of all regions showing at least one significant change in `fintra`, `fextra` or `fiso`. The bars represent the difference between $T2$ and $T1$ i.e. $(T2 - T1) * 100$.

¹¹ $T1$ and $T2$ being the mean value of the metric discussed in the concerned area in $T1$ and $T2$ respectively

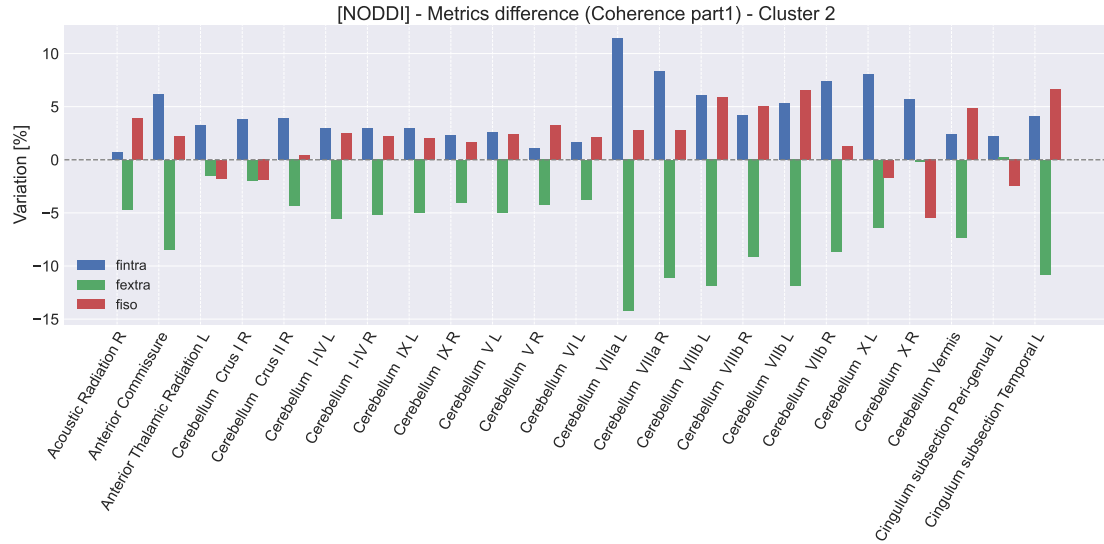


Figure C.2: Coherence of the NODDI model considering cluster 2 part1 - summary of all regions showing at least one significant change in **fintra**, **fextra** or **fiso**. The bars represent the difference between T2 and T1 i.e. $(T2 - T1) * 100$.

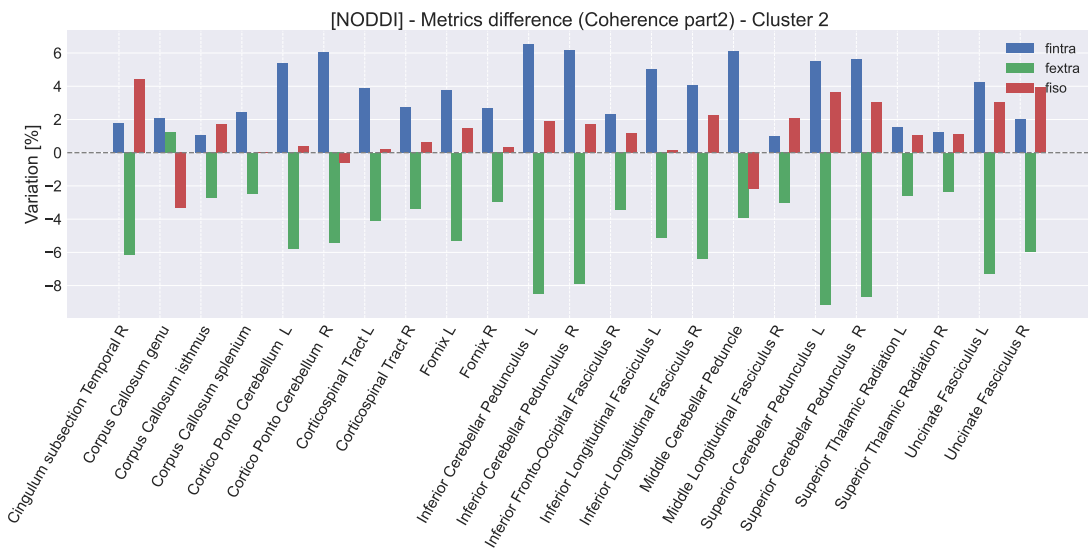


Figure C.3: Coherence of the NODDI model considering cluster 2 part2 - summary of all regions showing at least one significant change in **fintra**, **fextra** or **fiso**. The bars represent the difference between T2 and T1 i.e. $(T2 - T1) * 100$.

C.2 DIAMOND: Coherence of `frac_csf` and `frac_ftot`

First, two metrics of the DIAMOND model are directly related: the fiber fraction and the CSF fraction inside a voxel. This means that their sum always equals 1 and therefore their evolution between T1 and T2 are supposed to be complementary:

$$\begin{cases} \text{frac_ftot}(T1) + \text{frac_csf}(T1) = 1 \\ \text{frac_ftot}(T2) + \text{frac_csf}(T2) = 1 \end{cases}$$

$$\Rightarrow \text{frac_ftot}(T2) - \text{frac_ftot}(T1) = -(\text{frac_csf}(T2) - \text{frac_csf}(T1)) \quad (\text{C.2})$$

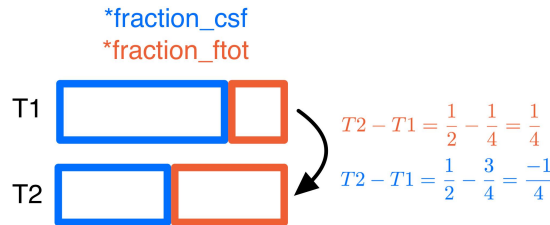


Figure C.4: Compensation of the CSF and fiber volume fractions.

The Figures C.5 and C.6 were thus built in the following way: if the percentage of change $(T2 - T1)/T1$ of at least one of the two metrics is considered as significantly changing during abstinence and if this change exceeds a threshold fixed at 8% for this work, then both metric progressions $(T2 - T1) * 100$ are plotted for this zone. This is a way to visualise both metrics at the same time and validate or not the consistency of the model.

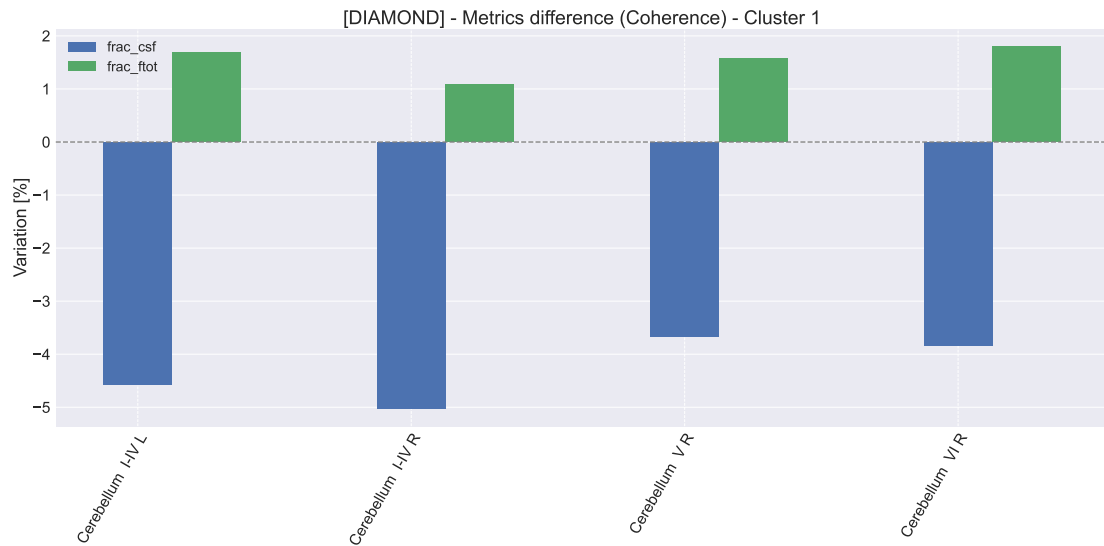


Figure C.5: Coherence of the DIAMOND model considering cluster 1 - summary of all regions showing at least one significant change in `frac_ftot` or `frac_csf`. The bars represent the difference between T2 and T1 i.e. $(T2 - T1) * 100$.

By having a first look at those figures, one can first observe that three areas demonstrate a big inconsistency by having both fractions increasing (see Figure C.6: cluster 2): the *Cerebellum I-IV L*, *VI L*, *VIIb R*. This is of course biologically not possible and this introduces the first downside of the model. Then, it is important

to focus on the values displayed on the graph. Indeed, both fractions are supposed to have identical absolute difference values and it is the case for a minority of areas. The origin of this model imperfection comes from the outputs of the ElikoPy pipeline. Indeed, if the three initial files `frac_f0`, `frac_f1` and `frac_csf` are summed up for one patient, the resulting map is not only composed of *ones* as expected, but also from various values reaching 3 in some pixels, which is absolutely not normal.

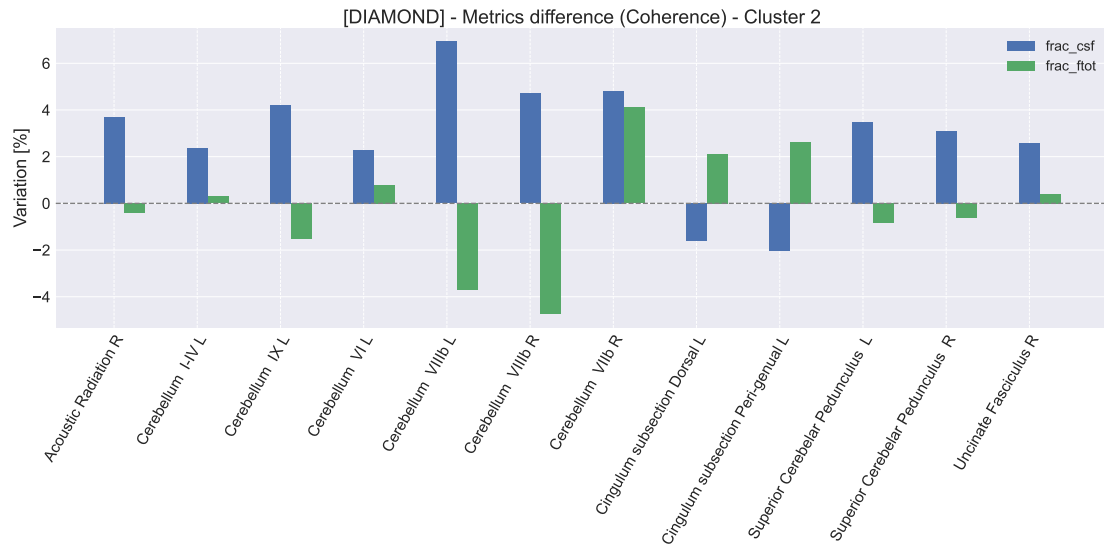


Figure C.6: Coherence of the DIAMOND model considering cluster 2 - summary of all regions showing at least one significant change in `frac_ftot` or `frac_csf`. The bars represent the difference between T2 and T1 i.e. $(T2 - T1) * 100$.

C.3 MF: Coherence of `frac_csf` and `frac_ftot`

In the same way as the DIAMOND model, the changes in `frac_ftot` and `frac_csf` are supposed to be opposite for a specific patient and a specific region, and thus also inside a cluster.

For this reason, a preliminary raw comparison of their evolution in the different areas provides a first insight of the reliability of the model and the results. As stated by equation C.2, the difference between T2 and T1 in a specific zone and a designated patient are supposed to compensate each other, as also illustrated in Figure C.4. This means that the global changes inside a cluster are expected to behave similarly for an identical group of pixels. Therefore, if an evolution is positive for a metric during abstinence, a decrease of opposite value is expected for the other metrics. This can be seen in Figure C.7, in which both metrics are displayed whenever a change in either metric has been identified as significant between T1 and T2, in the case of cluster 1. All the regions present an increase of `frac_ftot` and a complementary decrease of `frac_csf`, confirming the opposite tendencies of both metrics and thus the coherence of the MF model. As a matter of fact, the maximal difference between `frac_csf` and `frac_ftot` changes among both clusters is 0.7% which fully confirms the consistency of the model. The coherence corresponding to cluster 2 is depicted in Figure C.8.

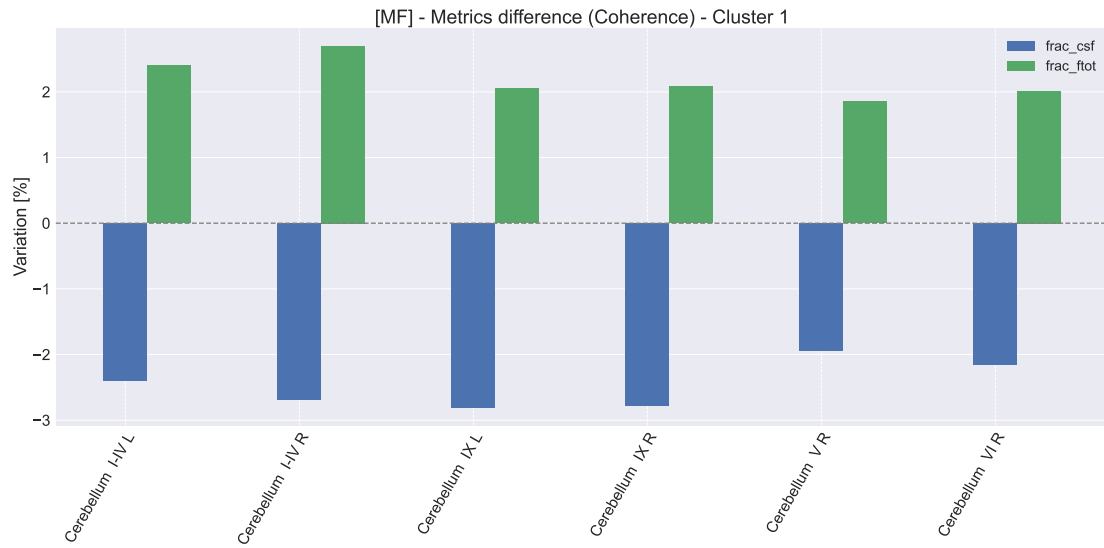


Figure C.7: Coherence of the MF model considering cluster 1 - summary of all regions showing at least one significant change in `frac_ftot` or `frac_csf`. The bars represent the difference between T2 and T1 i.e. $(T2 - T1) * 100$.

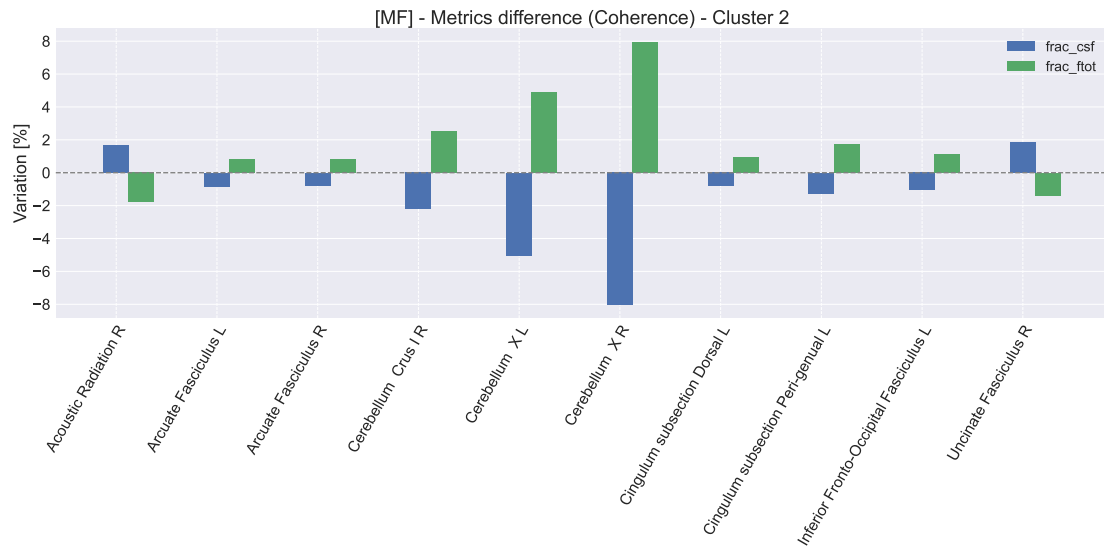


Figure C.8: Coherence of the MF model considering cluster 2 - summary of all regions showing at least one significant change in `frac_ftot` or `frac_csf`. The bars represent the difference between T2 and T1 i.e. $(T2 - T1) * 100$.

C.4 Coherence of FA, ODI and wFA

As some of the metrics analysed in the previous sections are either identical or sometimes directly linked to metrics from another microstructural model, analysing them together is a way to test the consistency of each model and to make sure that the evolution of the metrics is coherent.

It is interesting to compare ODI, a metric coming from NODDI model, and FA/wFA respectively coming from DTI and DIAMOND. As those metrics were created on the basis of three different mathematical models built with different theories, it is sometimes difficult to predict with certainty, the evolution that the metrics should have with respect to each other. However, according to their definition, one could expect the FA and wFA to evolve in the same way (both increasing or decreasing), whereas ODI represents an opposite concept and should thus have an opposite tendency.

By looking at first at cluster 1, the evolution of the three metrics in the only significant area, the *Cerebellum X L*, is coherent. Indeed, we observe an FA and wFA increase while ODI is decreasing.

Similarly to the previous analyses, cluster 2 seems to have many more significant zones compared to cluster 1 (see Figures C.9 and C.10). However, several regions seem to show inconsistencies in the evolution of the three metrics. For 4 of them, the three metrics are all increasing and In one other region, only ODI and wFA are evolving together. This is not what it is expected at first sight but as the microstructure of the brain can take many different configurations and as already said the models are also very different, it could explain those results without suggesting that one of the models is inconsistent.

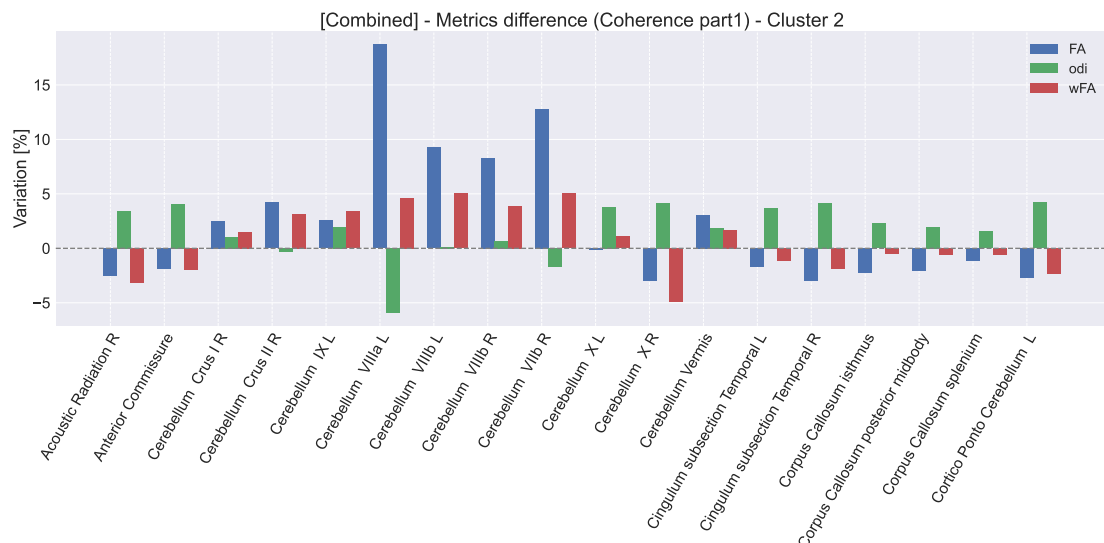


Figure C.9: Coherence of cluster 2 considering FA, ODI and wFA - part 1. The bars represent the difference between T2 and T1 i.e. $(T2 - T1) * 100$.



Figure C.10: Coherence of cluster 2 considering FA, ODI and wFA - part 2. The bars represent the difference between T2 and T1 i.e. $(T2 - T1) * 100$.

C.5 Coherence of fiso (NODDI) and frac_csf (DIAMOND, MF)

Another analysis is done on how the CSF evolves in the different models. The metrics used to this aim are `fiso` coming from the NODDI model and `frac_csf` extracted from the DIAMOND and the MF models, each representing the compartment of free water molecules. These results are depicted in Figures C.11 to C.13. These figures illustrate the evolution of the three metrics, in areas demonstrating at least one metric with a significant increase or decrease.

First of all, it is expected that the three metrics do change in the same direction (positive or negative) as they all represent the exact same concept. On the one hand, when considering cluster 1, one can observe that all three metrics are decreasing together and this, in all the significant areas displayed in Figure C.11.

On the other hand, looking more closely at what is happening in cluster 2 (see Figures C.12 and C.13), it can be seen that only 4 areas seem to show inconsistent behavior: the *Cerebellum I-IV L*, *IX L* and *VIIb R*, and *Inferior Fronto-Occipital Fasciculus R*. In the first 3 case, these zones describe a significant trend only for 2 of the three metrics: `fiso` and `frac_csf` (DIAMOND) increase while `frac_csf` (MF) decreases. However, as it is the latter that does not show a significant evolution, one can assume that the small changes it has, is in fact due to noise, inaccuracies between two scans,... One can conclude that generally the microstructural models are again consistent with each other.

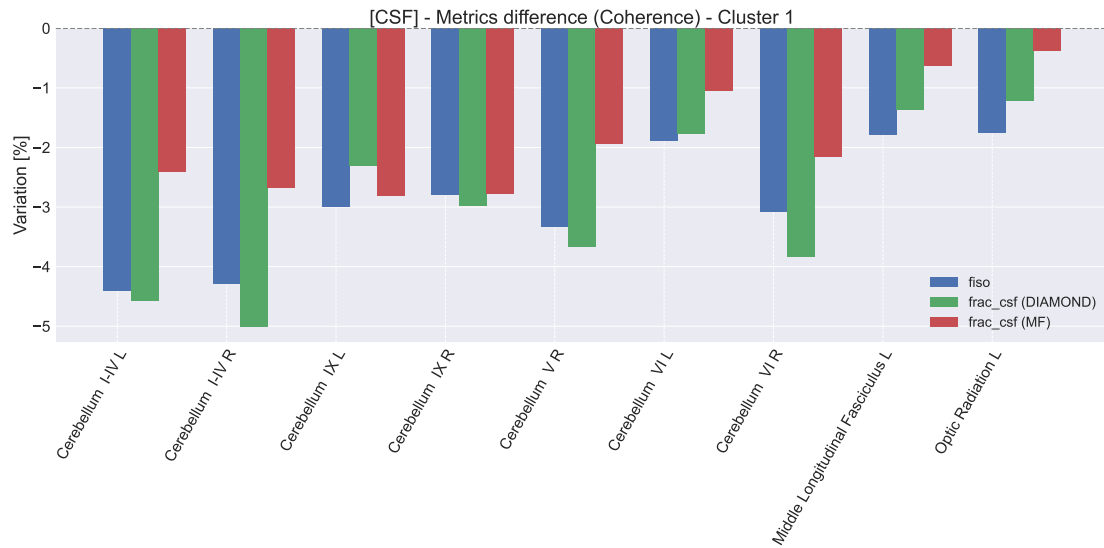


Figure C.11: Coherence of cluster 1 considering `fiso`, `frac_csf` (DIAMOND) and `frac_csf` (MF). The bars represent the difference between T2 and T1 i.e. $(T2 - T1) * 100$.

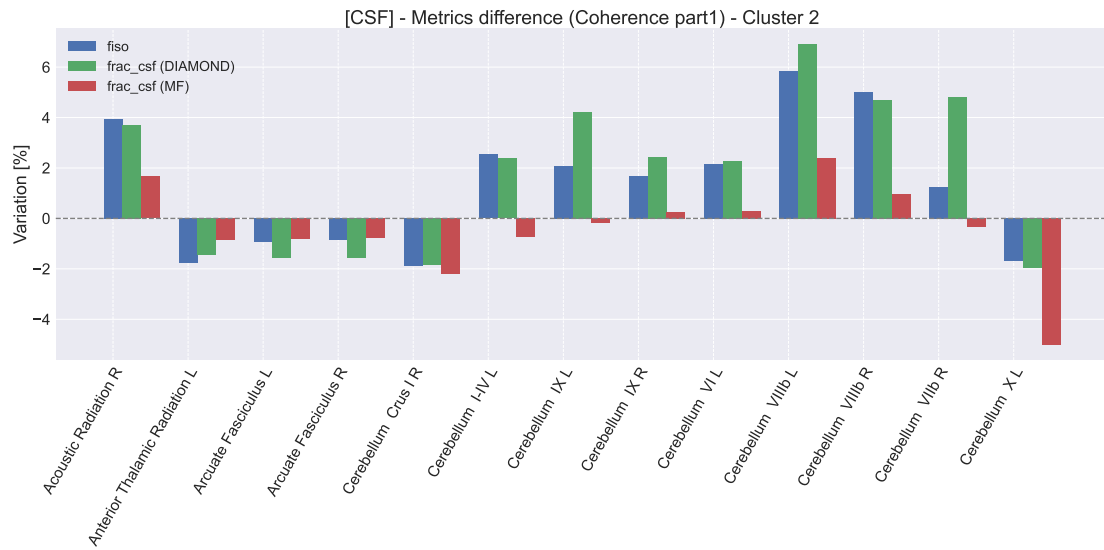


Figure C.12: Coherence of cluster 2 considering fiso, fraction_csf and frac_csf - part 1. The bars represent the difference between T2 and T1 i.e. $(T2 - T1) * 100$.

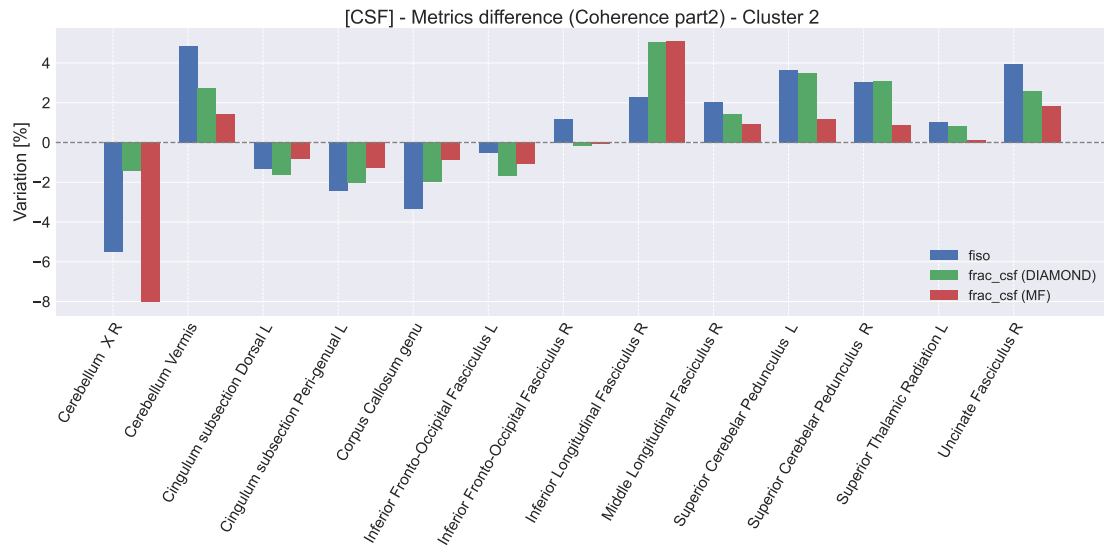


Figure C.13: Coherence of cluster 2 considering fiso, fraction_csf and frac_csf - part 2. The bars represent the difference between T2 and T1 i.e. $(T2 - T1) * 100$.

UNIVERSITÉ CATHOLIQUE DE LOUVAIN
École polytechnique de Louvain

Rue Archimède, 1 bte L6.11.01, 1348 Louvain-la-Neuve, Belgique | www.uclouvain.be/epl